TRINITY COLLEGE DUBLIN

Interactions Between Quantum Emitters in the Presence of Plasmonic Nanostructures

Candidate:
Vasilios D. Karanikolas

Supervisor:
Prof. A. Louise Bradley

Declaration

I declare that this thesis has not been submitted as an exercise for a degree at this or any other university and it is entirely my own work.

I agree to deposit this thesis in the University's open access institutional repository or allow the library to do so on my behalf, subject to Irish Copyright Legislation and Trinity College Library conditions of use and acknowledgement.

I have read and I understand the plagiarism provisions in the General Regulations of the University Calendar for the current year, found at http://www.tcd.ie/calendar.

I have also completed the Online Tutorial on avoiding plagiarism 'Ready Steady Write', located at http://tcd-ie.libguides.com/plagiarism/ready-steady-write.

Summary

In this thesis the spontaneous emission, of a single quantum emitter, and the energy transfer, between a pair of quantum emitters, rates are investigated in the presence of conducting nanostructures. The competition between these two rates leads to the introduction of the energy transfer efficiency. Metallic and graphene nanostructures are investigated. The excitation of surface plasmon modes, hybrid modes of the conduction band electrons and the electromagnetic field, is crucial for enhancing the spontaneous emission and energy transfer rates, compared with their free space values.

The near field of the quantum emitters can directly excite the surface plasmon modes. The surface plasmon wavelengths depend on the shape and material properties of the nanostructures. The spectral and distance dependences of the spontaneous emission and energy transfer processes are studied. It is of particular interest, from the point of view of applications, to be able to manipulate the light at nanometer distances.

In particular, metallic multilayer planar and cylindrical geometries are investigated. The noble metals, Ag and Au, are used as the conducting metallic medium. Their surface plasmon wavelengths lie in the visible part of the spectrum. For planar geometries the distance and spectral dependences of the spontaneous emission rate are analyzed, and their connection with the dispersion relation, the propagation length and penetration depth of the surface plasmon mode is pointed out. For the dielectrically coated cylinder the influence of the coating on coupling with the near field of the quantum emitters and excitation of the surface plasmon mode, which subsequently leads to larger interactions distances, is presented. The energy transfer efficiency is influenced by the overlap of the emission spectrum, of the donor quantum emitter, and the absorption spectrum, of the acceptor quantum emitter, with the surface plasmon resonance wavelength. Then, the interaction distance between the quantum emitters can be enhanced compared with their free space value. Tuning the surface plasmon wavelength to the emission wavelength of the donor via the geometrical and material parameters of the coated cylinder allows control of the energy transfer efficiency.

Furthermore, a graphene monolayer and graphene nanodisk are considered as conducting media supporting surface plasmon modes. Their surface plasmon wavelengths lie in the near to far infrared part of the spectrum. For the gated graphene monolayer the influence of the propagation length and penetration depth on the energy transfer rate is presented. The graphene monolayer can support efficient coupling between the quantum emitters up to distances of 300 nm when the quantum emitters are on resonance with the surface plasmon mode.

For the graphene nanodisk the surface plasmon frequencies are investigated. Different tran-

sition dipole moments of the quantum emitters excite different sets of resonances. When the emission wavelength of the quantum emitter matches the resonance frequencies, the spontaneous emission and energy transfer rates are enhanced by several orders of magnitude compared with their free space values. The distance dependence of the energy transfer rate between a pair of quantum emitters, placed perpendicularly to the graphene nanodisk plane, is studied and is found that it depends on the geometrical characteristics of the graphene nanodisk in contrast with the graphene monolayer where the penetration depth, of the surface plasmon mode, dominates.

Acknowledgements

I would like to thank my supervisor Dr. Louise Bradley first of all for giving me the opportunity to conduct my research in her group. Her enthusiasm and passion with physics was a great motivation for me. Also, in the bad days she was there to encourage me. The search for rigorous explanations for all the results we discussed will always inspire me.

I want to express my gratitude to Dr. Cristian Marocico for all the help in the world that he has provided to me. He introduced me to the field of the Green's tensor formalism and taught me all I know about programing. I would like to thank him for the numerous hours we spent discussing the physical aspects I present in this thesis and physics in general.

I'd like to thank the examiners of this thesis, David L. Andrews and Paul Eastham, for the time they spent reviewing it and providing a further insight into the subject.

All the help I got from the members of the group was always valuable. I am grateful to Xia Zhang, Luke Higgins, Graham Murphy, John Gough, Keith Wilson and Esteban Pedrueza whowere part of the group during the period of my PhD. We had a lot of discussions on the experimental work they performed and they always had time to explain how physics really works and fill the gaps in my knowledge. I thank all the other guys in the office, Azat, Marta, Ertugrul and Nicolas for the enjoyable environment for working. Also all the photonics group for the weekly presentations, there were always some nice ideas and physics there to be discussed.

Also, I would like to thank a lot of people working in the Physics Department who make my life a lot easier with their work. In particular, Jeanette Cummins, Ken Concannon, Alan O'Meara and Ciara Scanlon: thanks a lot for your help in the various difficulties encountered, from financial paper work to printing the posters.

There are numerous people that I would like to thank for all the mental support they provided the last four years and the long Skype talks we had. Jules and Ivo thank you for the Friday evening pint sessions. For the Skype talks Papasam, Nikos Kamp., Kiriakos, Paulos,

Nikos Kar., Alexandros, Zoe, Nionios, Erato. The list won't finish if I start thanking all the people back in Greece. Arnold, Aga, Karaca, Ruaraidh for being, not at the same time, my flatmates.

I am grateful to my parents and my brother. They were always there to provide me support and encouragement, when needed, thank you again. Finally, Pelin, I can't thank you enough for all the love and joy you have brought to my life and sorry for all the weekends I spent in the office.

List of publication and conference contributions

List of publications

Publications connected with the thesis:

1. Vasilios Karanikolas, Cristian A. Marocico, and A. Louise Bradley. "Spontaneous emission and energy transfer rates near a coated metallic cylinder." Phys. Rev. A 89, 063817 (2014)

2. Vasilios D. Karanikolas, Cristian A. Marocico, and A. Louise Bradley. "Dynamical tuning of energy transfer efficiency on a graphene monolayer." Phys. Rev. B 91, 125422 (2015)

3. Vasilios D. Karanikolas, Cristian A. Marocico, and A. Louise Bradley. "Tunable and long range energy transfer efficiency through a graphene nanodisk." Submitted (2015)

Other publications:

1. L.J. Higgins, V.D. Karanikolas, C.A. Marocico, A.P. Bell, T. C. Sadler, P.J. Parbrook, and A.L. Bradley. "Carrier density dependence of plasmon-enhanced nonradiative energy transfer in a hybrid quantum well-quantum dot structure." Optics Express 23, 2, 1377 (2015)

Conference contributions

Oral presentations:

1. Vasilios D. Karanikolas, Cristian A. Marocico, and A. Louise Bradley. "Decay and Energy Transfer rates in Metal/Dielectric core-shell cylinders." E-MRS Spring 2013, 27th-31st May 2013, Strasbourg, France

2. Vasilios D. Karanikolas, Cristian A. Marocico, and A. Louise Bradley. “Energy Transfer Tunability for Varying Dielectric Permittivity and Thickness of the Coating of a Metallic Cylinder.” 17th Nanoscale Simulators Ireland and Irish Atomistic Simulators Meeting, 26th-27th May 2014, Belfast, Northern Ireland

3. Vasilios D. Karanikolas, Cristian A. Marocico, and A. Louise Bradley. ”Graphene Plasmonics for Efficient Energy Transfer.” Optical wave and waveguide theory and numerical modeling workshop, 17th-18th April 2015, London, England

4. Vasilios D. Karanikolas, Cristian A. Marocico, and A. Louise Bradley. “Tunable and Efficient Long Range Energy Transfer Via Graphene Plasmon Modes.” METAMATERIALS’ Oxford 2015, 7th-12th September 2015, Oxford, England

Selected list of poster presentations:

1. Vasilios D. Karanikolas, Cristian A. Marocico, and A. Louise Bradley. “Localized surface plasmons, field intensity and energy transfer.” EuroNanoForum 2013, 18th-20th June 2013, Dublin, Ireland

2. Vasilios D. Karanikolas, Cristian A. Marocico, and A. Louise Bradley. “Energy Transfer between a Quantum Well and Quantum Dots for LEDs applications ” International conference on optics of excitons in confined systems - OECS 13, 9th-13th September 2013, Rome, Italy

3. Vasilios D. Karanikolas, Cristian A. Marocico, and A. Louise Bradley. “Energy Transfer Rate between a Pair of Quantum Emitters in the Presence of a Coated Metallic Cylinder.” Nanolight 2014, 2nd-8th March 2014, Benasque, Spain

4. Vasilios D. Karanikolas, Cristian A. Marocico, and A. Louise Bradley. “Long Range Energy Transfer Efficiency Through Graphene Nanostructures.” Photonics Ireland 2015, 2nd-4th September 2015, Cork, Ireland

Contents

Chapter 1

General Introduction

1.1 Motivation: enhance the interaction between quantum emitters over larger distances

Developing new techniques to control and manipulate the interaction between light and matter has been in the spotlight in science and engineering since the advent of Maxwell's equations. The work of James Clerk Maxwell was confirmed by a series of experiments which agreed very well with his equations. It was the first time that physicists had an elegant way of describing light-matter interactions at the classical level.

The revolutionary theory of quanta was able to explain phenomena which up to this point classical physics was unable to explain, like the black body radiation. The discrete nature of light was revealed by the work of Planck and Einstein. The early quantum theory was significantly reformulated in the mid-1920s by Werner Heisenberg, Max Born, Wolfgang Pauli and their collaborators; the Copenhagen interpretation of Niels Bohr became widely accepted. By 1930, quantum mechanics had been further unified and formalized by the work of Paul Dirac and John von Neumann, with a greater emphasis placed on measurement in quantum mechanics, the statistical nature of our knowledge of reality.

The unification of quantum theory with special relativity led to one of the biggest conceptual human achievements: quantum electrodynamics (QED). In essence, QED describes how light and matter interact, and it covers all phenomena involving charged particles interacting by means of exchange of photons. It represents the quantum counterpart of classical electrodynamics giving a complete account of light-matter interactions. The accuracy of this theory is quite remarkable, with discrepancies between theory and experiment being as small as 10^{-8}. Among the pioneers of QED were Sin-Itiro Tomonaga, Julian Schwinger, Freeman Dyson and

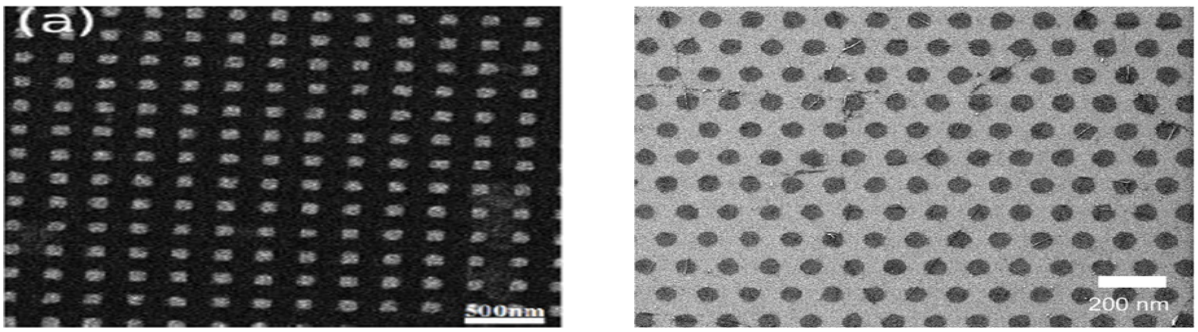

(a) **(b)**

Figure 1.1: *Image of patterned nanostructures. (a) Ag nanoboxes array fabricated by helium ion lithography, taken from [18]. (b) Graphene nanodisk array fabricated by electron beam lithography, taken from [19].*

Richard Feynman.

Feynman made many contributions to different areas in physics and is also considered to be the first to propose that it could be possible to manipulate matter at nanoscale dimensions. Feynman predicted the emergence of quantum effects when considering dimensions of the order of a nanometer at the border between the macroscopic and microscopic worlds [1]. Nanophotonics or nano-optics is the study of the behavior of light on the nanometer scale, and of the interaction of nanometer-scale objects with light. It is a branch of optics, optical engineering, electrical engineering, and nanotechnology [2].

For the last couple of decades the field of plasmonics has been an area of extensive experimental [3–6] and theoretical investigations [7–9]. Confining light to subwavelength structures has various applications such as plasmon rulers [10], biosensing devices [11, 12], light harvesting [13], optical nanoantennas [14], plasmonic tweezers [15] and quantum information processing. The extreme confinement of light in subwavelength structures is achieved by exciting surface plasmon (SP) modes [16]. The SP modes are collective oscillations of electrons and the electromagnetic field that are excited at the interface between a dielectric and a conductor. In the literature, a SP mode is called SP polariton (SPP) mode [17], when the plasmonic nanostructure is extended, and they are called localized SP (LSP) modes [8], when the nanostructure is finite. Throughout this thesis the term SP modes is used to describe both these modes. In plasmonics the most commonly used conductors are the noble metals Ag and Au, since their SP wavelengths lie in the visible part of the electromagnetic spectrum, making them of significant practical importance.

Several technological inventions have been made in the last 20 years that have made the modern field of plasmonics possible. The invention of the scanning tunneling microscope in 1981, which provided unprecedented visualization of individual atoms and bonds, for the

first time, was of indispensable importance for observing individual atoms. Colloidal synthesis techniques have made possible the preparation of complicated conducting nanostructures with shapes such as spheres, boxes and triangles. Fabrication of structures, with nanometer precision can be achieved using lithography, electron beam lithography or helium ion beam lithography. Patterned periodic nanostructures are nowadays routinely fabricated using these techniques. We present in Fig. 1.1a a patterned nanostructure of Ag nanoboxes [18].

Of particular importance are the interactions between quantum emitters and nanostructures for applications such as efficient photon collection, single photon switching and long range optical coupling of quantum-bits. As quantum emitters they can be considered quantum mechanical systems that they can be approximated as two-level systems. There is a variety of these types of quantum systems such as atoms, molecules, semiconductor quantum dots, nitrogen-vacancies color centers in diamonds and superconducting quantum bits.

Spontaneous emission (SE) is the process by which an initially excited quantum emitter spontaneously decays to its ground state by emitting a photon. In 1946 Purcell showed that the environment of the quantum emitter influences its SE rate [20]. Even if the quantum emitter is placed in vacuum, the presence of a material body in its vicinity can influence the local density of states (LDOS) of the electromagnetic field. Various structures have been investigated with respect to their role in modifying the SE of a quantum emitter: planar [21–28], cylindrical [29–40], spherical [41–46], prolate spheroids [47, 48] and metallic nanotip [49–51] geometries.

The second interaction process that is investigated in this thesis is the transfer of the excitation energy of a quantum emitter (donor) to another quantum emitter that is in its ground state (acceptor) [52, 53]. This process is called energy transfer (ET). Considering the distance dependence of the ET rate between the donor-acceptor pair, we can distinguish three regimes (in the following R is the donor-acceptor distance and λ is the emission wavelength of the donor): (a) the short range regime, $R \ll \lambda$, first studied by Förster, where the ET rate dependence is R^{-6}, which is similar to the electrostatic coupling between a pair of dipoles, (b) the radiative long-range regime, where $R \gg \lambda$, which has a R^{-2} dependence, and (c) the intermediate regime, $R \sim \lambda$, where the distance dependence is R^{-4} [54, 55]. The ET rate can also be considered as a photon exchange process. In the Förster regime the photons are virtual and they appear as non-observable intermediate states in the quantum electrodynamic analysis. In the radiative regime, on the other hand, the photons are real and the ET can be viewed as the emission and absorption of a real photon. The energy transfer between a pair of quantum emitters has also been investigated in the presence of various geometries: planar [28, 56–60], cylindrical [37, 38, 61], spherical [62–66], photonic crystal [67, 68] and edge and channel waveguides [69, 69].

As has already been mentioned, plasmonics is used to trap light at subwavelength dimensions. Also, the SE and ET rates can be enhanced when conducting material bodies are placed in close proximity to the quantum emitters, due to the excitation of SP modes [4, 24, 70, 71]. The SP modes exist mainly at a specific resonance wavelength which depends on the geometrical characteristics of the bodies and on their optical properties, i.e. their dielectric permittivity. These unique properties provided by conducting nanostructures when interacting with quantum emitters can be used, and are used, in various applications such as surface enhanced Raman scattering, biosensing devices, plasmonic lasers, quantum computing and as interconnectors for integrated photonic chips. Knowledge of the distance dependence of the SE rate of a single quantum emitter, and the ET rate between a pair of quantum emitters, in the presence of conducting nanoparticles is of absolute importance in order to fully exploit the possibilities provided by plasmonics. In this thesis the main goal is to present ways of understanding the distance dependence of these rates and propose ways to further enhance their interaction distances.

The ET rate between quantum emitters in homogeneous media, with real positive dielectric permittivity, falls off really fast, as R^{-6}. Using the SP modes the interaction distance is enhanced and efficient transfer energy between quantum emitters placed in the vicinity of conducting nanostructures can be achieved. In the last decade graphene has been considered as an alternative to using noble metals for plasmonic applications [72–75].

Graphene is a material with exciting properties which may be used in the near future as an all optical basis due to its tunable material properties [73, 76]. In particular, graphene plasmonics has emerged as a field of intense experimental [19, 74, 75, 77–80] and theoretical [72, 81–86] investigation over the last decade. Graphene has important advantages compared with conventional plasmonic materials, such as noble metals, where large material losses cannot be easily avoided [72]. Some of the desirable properties of graphene are: higher mechanical properties [87], the fact that graphene does not require a substrate, its low losses [72] and, due to its two dimensional nature, huge optical enhancements when interacting with quantum emitters in close proximity.

An undoped graphene monolayer (GM) can absorb $\pi\alpha_0 \approx 2.3\%$ of the light incident upon it, at wavelengths in the visible part of the spectrum, where α_0 is the fine structure constant [88]. Patterned GM nanostructures can give rise to 100% absorption at specific wavelengths, which can be tuned through the applied voltage [89, 90]. The optical response of various graphene nanostructures has been investigated theoretically and experimentally. These varied geometries include, graphene monolayers [91–97], graphene ribbons [90, 98–105], nanotubes [106–109] and nanodisks [89, 110–114].

The interaction of quantum emitters and graphene nanostructures has been theoretically investigated. In particular, the SE rate of quantum emitters in proximity to a graphene monolayer is enhanced several orders of magnitude compared with its free space value [93, 94, 97, 115]. This effect is due to the extreme confinement of light due to the two dimensional nature of the graphene monolayer [99]. Further confinement of light, by reducing the dimensionality, enhances these interactions even more [81]. Another less studied process of particular interest is the ET process between a pair of quantum emitters which, in close proximity to a graphene monolayer, can also be extended over large distances due to the excitation of propagating SP modes [97]. When the 1D confinement of light is considered, as in graphene nanoribbons [81, 99] and nanotubes [106, 109], the propagation length of the SP is increased and so is the interaction distance. For the case of a graphene nanodisk, the confinement of light in all three dimensions [81, 110, 111] produces large field enhancements which might be used in order to extend the interaction between the quantum emitters to larger distances.

In this thesis, in Chapter 6 the interaction between quantum emitters in the presence of a gated graphene nanodisk is studied. Graphene nanodisk structures have been investigated in depth over the last few years and Fig. 1.1b depicts an array of patterned graphene nanodisks. Electrically gated patterned graphene nanostructures [19, 116], nanodisks and nanorings, interact strongly with the incoming light and the confinement parameter is large compared with the radius of these nanostructures, $\lambda^3/R^3 \gg 1$. As previously mentioned, a patterned array of graphene nanodisks has been predicted to provide 100% absorption [89]. Similar predictions have been made concerning a photonic crystal consisting of nanoholes patterned in a graphene substrate in the near infrared optical regime [117]. Furthermore, a graphene monolayer decorated with small metallic nanoparticles, with zero chemical potential, can support strong absorption [118]. These interactions have been predicted to be blue-shifted when considering more layers of graphene nanodisks instead of a single nanodisk [119, 120]. Edge states and an applied magnetic potential can also influence the response of these nanostructures [114, 121]. Further quantum effects have been considered in the regime where non-linear effects emerge in the coupled quantum emitter-graphene nanodisk system [122, 123].

Using the plasmonic response of the conducting, metallic and graphene, nanostructures we can trap the light in nanometer dimensions. The large spatial confinement of light gives rise to large field enhancements compared to free-space. For extended conducting nanostructures interacting with QEs, e.g. metallic slabs, metallic nanocylinders, edge and channel waveguides, graphene monolayers, graphene ribbons, the large field enhancements may be attributed to the strong confinement of the propagating SPs, leading to much larger field values than in free-space [95, 99, 109, 124, 125]. Large field enhancement values are also observed when

the interaction between QEs and zero dimensional nanostructures, e.g. nanospheres and nanodisks, is considered, due to the excitation of localized plasmon modes. However, a large field enhancement does not necessarily mean that the absolute value of the field intensity is large enough to facilitate efficient interactions.

To experimentally probe these interactions, one measures the lifetime of the quantum emitter, whose inverse is the total decay rate, given by an overlap integral of the form [42, 126]

$$k_{\mathrm{SE}} \propto \int_0^\infty \mathrm{d}\lambda\, f_D(\lambda) \mathrm{Im}(\mathbf{n}_{\mathrm{D}} \cdot \mathfrak{G}^{\mathrm{ind}}(\mathbf{r}_{\mathrm{D}}, \mathbf{r}_{\mathrm{D}}, \lambda) \cdot \mathbf{n}_{\mathrm{D}}), \tag{1.1}$$

while the energy transfer rate between a pair of quantum emitters can be written as [59],

$$k_{\mathrm{ET}} \propto \int_0^\infty \frac{\mathrm{d}\lambda}{\lambda^2} f_{\mathrm{D}}(\lambda) \left|\mathbf{n}_{\mathrm{A}} \cdot \mathfrak{G}(\mathbf{r}_{\mathrm{A}}, \mathbf{r}_{\mathrm{D}}, \lambda) \cdot \mathbf{n}_{\mathrm{D}}\right|^2 \sigma_{\mathrm{A}}(\lambda), \tag{1.2}$$

where $f_{\mathrm{D}}(\lambda)$ is the emission spectrum of the donor quantum emitter, placed at $\mathbf{r}_{\mathrm{D}}$, and σ_{A} is the absorption cross-section of the acceptor quantum emitter, placed at $\mathbf{r}_{\mathrm{A}}$. More details for these expression are given in Chapter 2. For both these expressions, the quantity encapsulating the response to the relevant nanostructure is the Green's tensor, $\mathfrak{G}(\mathbf{r}_{\mathrm{A}}, \mathbf{r}_{\mathrm{D}}, \omega)$. Classically, the Green's tensor represents the response of the geometry under consideration to excitation by a point-like dipole. Thus we can see that rather than the field enhancement, it is the field strength that is most important. Furthermore, Eq. (1.2) shows that the ET rate is dependent on the SE rate of the donor QE.

In Ref. [127] the authors investigate the energy transfer efficiency between monolayers of donor and acceptor colloidal quantum dots in the presence of Au nanospheres, experimentally and theoretically. In Fig. 1.2a the structure investigated in Ref. [127] is presented. The probability of efficient coupling between a donor layer and an acceptor layer is given by the energy transfer effeciency. In Fig. 1.2b the energy transfer is presented when a layer of donors is kept fixed and the position of the acceptor layer is varied. When both are embedded in a homogeneous medium their interaction distance fall very fast. When a layer of Au spheres is sandwiched between the donor and acceptor layers, the donor quantum emitters can efficiently transfer energy to the acceptors at unreachable distances compared with the homogeneous space case. Thus, the modification of the energy transfer efficiency by the spontaneous emission rate is verified by explaining experimental results concerning the ET efficiency between quantum emitters in the presence of gold nanospheres [127]. More details will be given in Chapter 2.

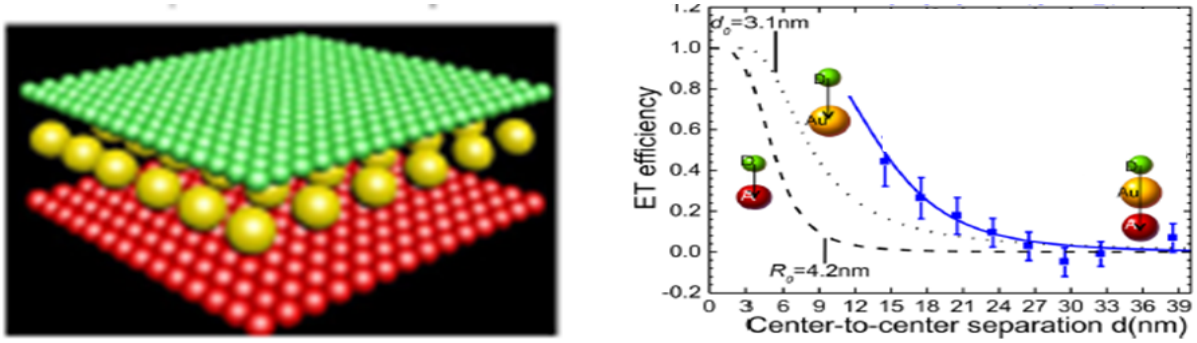

(a) **(b)**

Figure 1.2: *(a) A layer of donor quantum dots, green spheres, is interacting with a layer of acceptor quantum dots, red spheres, in the presence of Au metal nanospheres. (b) Energy transfer efficiency between: (i) a layer of donors and a layer of acceptors, dashed line, (ii) a layer of donors and a layer of Au spheres, dot line, (iii) a layer of donors to a layer of acceptor, when a layer of Au spheres is sandwitched between them, solid line. Taken from Ref. [127].*

The main purpose of this thesis is the theoretical investigation of the SE and ET rates in the presence of the conducting nanostructures [54, 55]. In particular, these rates are investigated for planar and cylindrical Au and Ag metallic nanostructures and a graphene monolayer and nanodisk.

1.2 Plasmonic materials

Noble metals, Au and Ag, contain nearly free electrons. They possess unique electromagnetic properties as compared to normal positive dielectric materials. Furthermore, graphene, a material that has emerged as an alternative to noble metals, has small material losses opening new routes in the field of plasmonics.

There are various ways of exciting SP modes on conducting nanostructures, depending on the source of excitation and the form of nanostructure. As a source of excitation one can consider a plane wave, a low energy electron beam or a quantum emitter. When a plane waves is used to excite extended nanostructures, specific requirements have to be fulfilled to compensate for the momentum mismatch between the plane wave and the SP mode. This can be done if the extended nanostructures have a defect or are corrugated or other special techniques described in this section are employed. When the nanostructures are finite the SP modes can be excited using any source. A low energy electron beam and a quantum emitter can excite directly SP modes in any nanostructure. In this thesis the interaction between quantum emitters in the presence of extended nanostructures is discussed in chapters 3, 4 and 5. The interaction of conducting nanostructures with a low energy electron beam is not the subject of

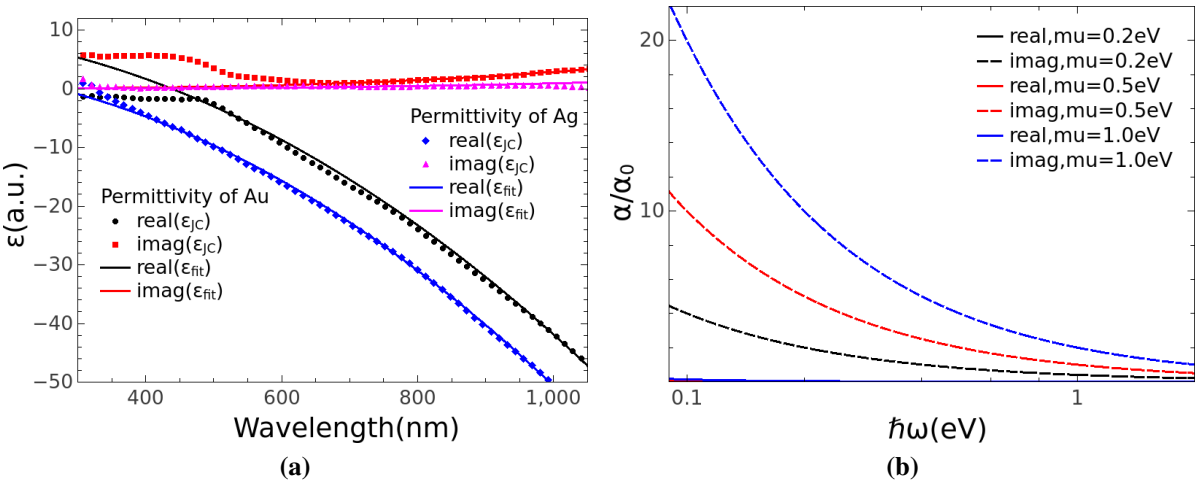

Figure 1.3: *(a) Real and imaginary part of the dielectric permittivity of Au and Ag as a function of wavelength. The point are for experimental data from Ref. [129] and the solid lines are fittings using Eq. 1.4. For Au* $\hbar\omega_p = 8.95\,eV$ *and* $\hbar\Gamma_{Au} = 68.5\,meV$ *and for Ag* $\hbar\omega_p = 9.17\,eV$ *and* $\hbar\Gamma_{Ag} = 21\,meV$*. (b) Surface conductivity,* σ*, as a function of frequency, using Eq. 1.5,* $\tau = 1\,ps$*. Different values of the chemical potential,* μ*, are considered.*

this thesis and more details on this subject can be found in Ref. [128] and references therein.

In this section a brief description of the material properties for Drude metals and graphene is given. Their plasmon dispersion relation is extracted. The Kretschmann and Otto methods for exciting SP modes by plane wave excitation are presented. These methods are used experimentally to excite SP modes for planar nanostructures. The advantage of using quantum emitters for exciting SP modes will become clear.

1.2.1 Optical properties of noble metals

The optical properties of noble metals can be described by a complex dielectric function that depends on the frequency of light. The presence of an electric field leads to a displacement, $\mathbf{r}$, of an electron, moving freely in the bulk. We consider the Drude-Sommerfeld model for describing the free electron gas

$$m_e \frac{\partial^2 \mathbf{r}}{\partial t^2} + m_e \Gamma \frac{\partial \mathbf{r}}{\partial t} = e\mathbf{E}_0 e^{-i\omega t}, \tag{1.3}$$

where e and m_e are the free electron charge and effective mass, respectively, and $\mathbf{E}_0$ and ω are the electric field amplitude and frequency, respectively. The damping term is given by the expression $\Gamma = v_F/l$, where v_F is the Fermi velocity and l is the electron mean free path between scattering events. Making the ansatz $\mathbf{r} = \mathbf{r}_0 e^{-i\omega t}$ and substituting to Eq. (1.3) it can

be shown that [130]

$$\varepsilon_{\text{Drude}} = 1 - \frac{\omega_p^2}{\omega^2 + i\Gamma\omega}, \tag{1.4}$$

where $\omega_p^2 = ne^2/m_e\varepsilon_0$ is the plasma frequency. For gold $\hbar\omega_p = 8.95\,\text{eV}$ and $\hbar\Gamma_{Au} = 68.5$ meV and for silver $\hbar\omega_p = 9.17$ eV and $\hbar\Gamma_{Ag} = 21$ meV. In Fig. 1.3a experimental data of the dielectric permittivity of Au and Ag are presented, from Ref. [129], and fitted data using Eq. 1.4. The experimental data for Au and Ag are used in Chapter 4.

1.2.2 Optical properties of graphene

In this thesis graphene is approximated as an infinitely thin conducting layer. Its optical properties are embedded in the frequency dependent surface conductivity, σ. Ignoring the interband transition, for the moment, the Drude conductivity is given by [72, 87, 131]

$$\sigma(\omega) = \frac{e^2}{\pi\hbar^2}\frac{i\mu}{\omega + i\tau^{-1}}, \tag{1.5}$$

μ is the chemical potential and τ is the finite relaxation time. In Eq. 1.5 the local limit is used where the inplane wavevector contribution is set to zero. The relaxation time, τ, contains information for all admissible decay mechanisms such as scattering of impurities and defects, to acoustic and optical phonons etc. Throughout this thesis the value of $\tau = 1\,\text{ps}$ is used [115, 132]. In Fig. 1.3b the surface conductivity, σ, is presented, as a function of frequency, ω. Different values of the chemical potential, μ, are considered.

The losses in graphene are seen to be much lower than for Au and Ag via $\hbar\Gamma_{Au}/\hbar\tau^{-1} \approx 10^2$ and $\hbar\Gamma_{Ag}/\hbar\tau^{-1} \approx 30$. From this comparison it is clear why graphene has become an area of intensive research in the field of plasmonics.

1.2.3 Excitation of surface plasmon modes

In order to excite the SP mode a transverse magnetic (TM) field is considered impinging a single interface, Fig. 1.4. The incident, reflected and transmitted electric fields have the form

$$\mathbf{E}_q = (-E_{xq}, 0, -E_{zq})e^{-ik_{zq}z + ik_s x} \tag{1.6}$$

where $E_{xq} = E_q\cos(k_q)$, $E_{zq} = E_q\sin(k_q)$ and $k_{zq} = \sqrt{k_q^2 - k_s^2}$, $q = i, r, t$ for the incident, reflected and transmitted electric field, respectively, and k_s is the in-plane wavevector. The relevant magnetic field is found from the expression $\mathbf{B}_q = \sqrt{\varepsilon_q\mu_q}\mathbf{k}_q \times \mathbf{E}_q/k_q$. Applying the

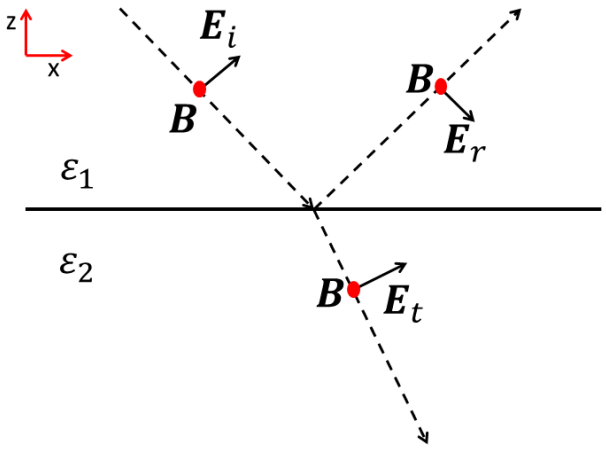

Figure 1.4: *Transverse magnetic field impinging on the interface between semi infinite materials described by ε_1 and ε_2 dielectric permittivities.*

boundary conditions at the $z = 0$ interface

$$\hat{n} \times (\mathbf{E}_i + \mathbf{E}_r - \mathbf{E}_t) = 0 \tag{1.7}$$

$$\hat{n} \times (\mathbf{H}_i + \mathbf{H}_r - \mathbf{H}_t) = \frac{4\pi\sigma}{c} \frac{k_{zt}}{k_t} E_{xt} \hat{y} \tag{1.8}$$

where σ is the surface conductivity, the reflection, $R = E_r/E_i$, and transmission, $T = E_t/E_i$, coefficients have the form

$$R = \frac{k_2^2 k_{z1} - k_1^2 k_{z2} + 4\pi\sigma\omega/c^2 k_{z1} k_{z2}}{k_2^2 k_{z1} + k_1^2 k_{z2} + 4\pi\sigma\omega/c^2 k_{z1} k_{z2}}, \tag{1.9}$$

$$T = \frac{4\pi\sigma\omega/c^2 k_{z1} k_{z2}}{k_2^2 k_{z1} + k_1^2 k_{z2} + 4\pi\sigma\omega/c^2 k_{z1} k_{z2}}, \tag{1.10}$$

where $k_i = \omega/c\sqrt{\varepsilon_i}$ and $k_{zi} = \sqrt{k_i^2 - k_s^2}$, $i = 1, 2$. The generalization of the above expressions can be easily found when considering multilayer stacks.

The case where layer 2 is Au is now considered, with no surface conductivity, $\sigma = 0$. The metal layer properties are given by a Drude type of model, Eq. (1.4), with $\hbar\omega_p = 9\,\text{eV}$ and ignoring the material losses, $\hbar\gamma_p = 0$. The material 1 is simply air. To find the minimum of the reflection at the air-Au interface, the denominator of Eq. (1.9) is set to zero, $k_2^2 k_{z1} + k_1^2 k_{z2} = 0$, from which we obtain the condition

$$k_s = \frac{\omega}{c} \sqrt{\frac{\varepsilon_1 \varepsilon_2}{\varepsilon_1 + \varepsilon_2}}, \tag{1.11}$$

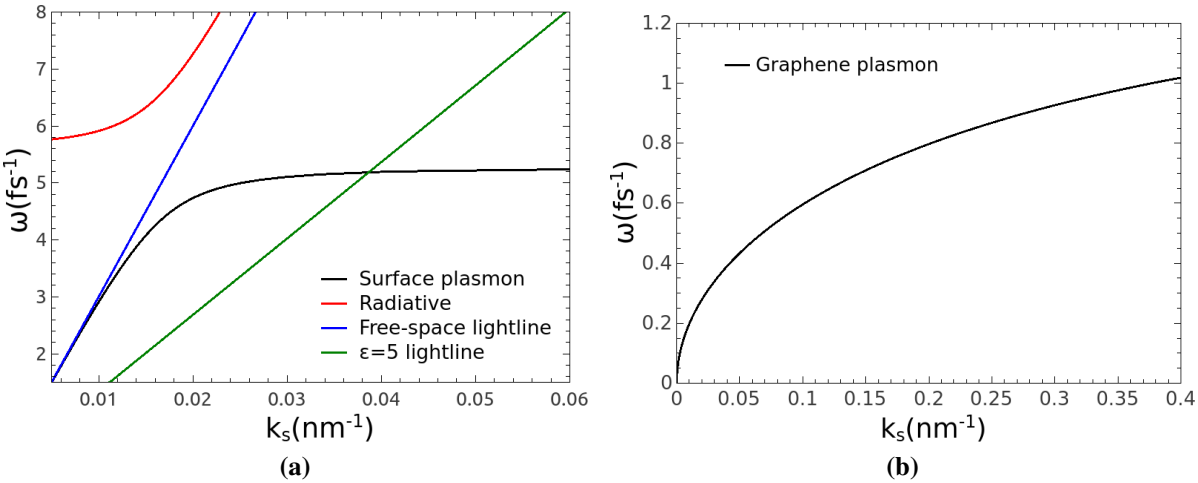

Figure 1.5: *Dispersion relation for (a) air-Au interface and (b) for free standing infinite graphene monolayer.*

which is the dispersion relation, $\omega(k_s)$. In Fig. 1.5a the dispersion relation curve lies below the light line, thus the SP mode cannot be excited due to momentum mismatch between its in-plane wavevector, k_s, and that of the incoming light. In order to overcome this difficulty, the Kretschmann configuration, depicted in Fig. 1.6a, is used [133].

Now the case of a free standing infinite graphene monolayer is considered, with air as the host medium. The surface conductivity of the infinite graphene monolayer is given by Eq. 1.5. To find the minimum SP dispersion relation, the denominator of Eq. (1.9), $k_1^2 + 2\pi\sigma\omega/c^2 k_{z1} = 0$ is set to zero, for $k_1 = k_2 = \omega/c$. The dispersion relation takes the form

$$k_s = \frac{\omega}{c}\sqrt{1 - \frac{c^2}{2\pi^2\sigma(\omega)^2}}. \tag{1.12}$$

The SP dispersion relation, for a chemical potential of $\mu = 1$ eV and relaxation time of $\tau = 1$ ps is shown in Fig. 1.5b. It is observed that the in-plane wavevector, k_s, for the case of graphene has larger values than the air-Au case, due to smaller material losses. Furthermore, in Fig. 1.5b the SP resonance frequencies are in the far infrared region, compared with the optical frequencies for the air-Au case. Also, in Fig. 1.5b the light line would be indistinguishable from the y-axis. In order to excite the SP mode in graphene the Otto configuaration, depicted in Fig. 1.6b, is used [134].

Excitation of SP modes on a flat conducting surface is not possible by direct light illumination, see Fig. 1.5. This is due to the fact that the wave vector of the SP modes, at a given frequency, is much larger than the free space wavevector. In Fig. 1.6a we present the Kretschmann configuration, which is routinely used for exciting SP modes at planar layers.

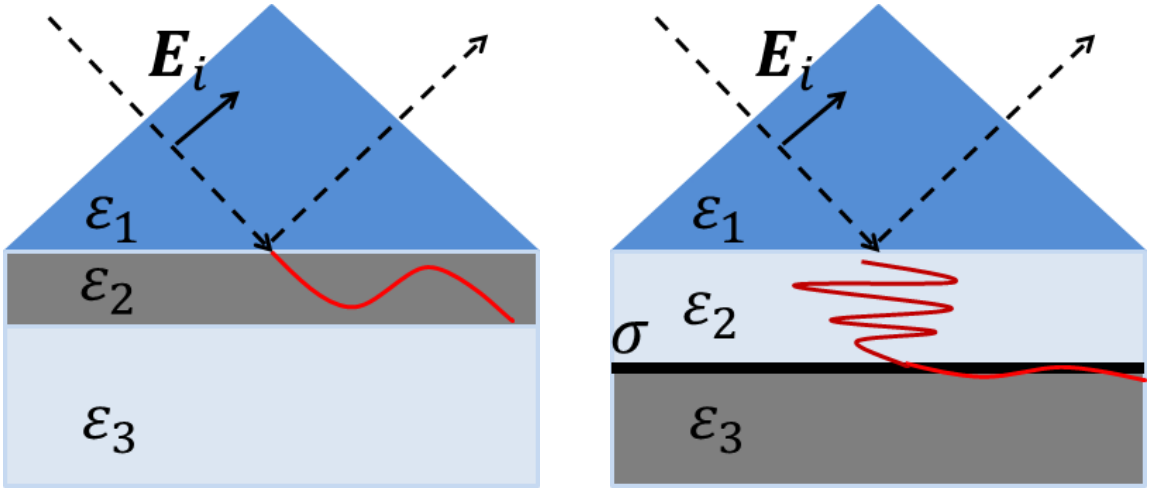

Figure 1.6: *Schematic of experimental setup for describing (a) the Kretschmann and (b) the Otto configuration.*

A thin conducting material is placed directly onto a prism. The dielectric permittivity of the prism is larger than the dielectric permittivity of the substrate, $\varepsilon_1 > \varepsilon_3$. The light again illuminates through the prism, and an evanescent wave penetrates through the metallic thin film. Fig. 1.3a shows that the real part of the dielectric constant is negative. This means that the plane wave can penetrate a metal over a small extent. Thus, since the SP mode is excited at the outer side of the film, the metallic films needs to be thinner than the penetration depth of light into the metal.

The second configuration for exciting SP modes, Fig. 1.6b, uses an attenuated total reflection configuration. Electromagnetic radiation coming from the prism impinges on the interface 1-2 at an angle θ larger than the critical angle for total internal reflection, $\theta > \arcsin(\sqrt{\max(\varepsilon_2, \varepsilon_3)/\varepsilon_1})$. So only evanescent waves can exists in the layer with ε_2, of thickness d, and in the half space ε_3. In this configuration it becomes possible to couple the incident wave to the SP mode in the conducting material because the dielectric permittivity constant of the prism, ε_1, is larger than the separation material ε_2. This is the Otto configuration for exciting the SP modes.

Each of these configurations is experimentally used to investigate excitation of SP modes in metallic planar layers, Kretschmann configuration, and graphene monolayer, Otto configuration, structures.

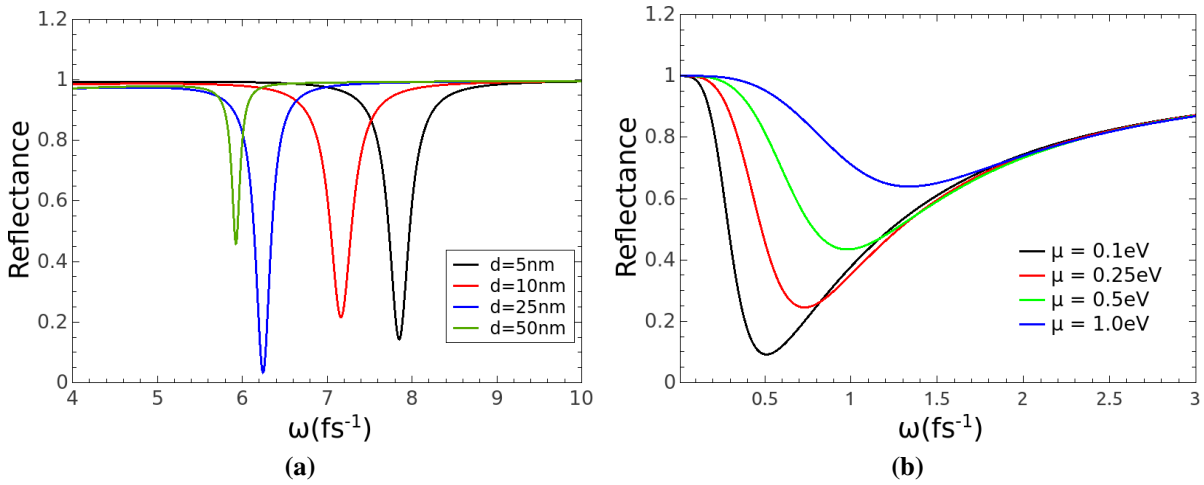

Figure 1.7: *Reflectance using the (a) Kretschmann and (b) Otto configurations for a metallic slab and a gated graphene monolayer.*

1.2.3.1 Metallic layer

The configuration depicted in Fig. 1.6a is considered with the values $\varepsilon_1 = 5$, $\varepsilon_2 = \varepsilon_{Au}$ and $\varepsilon_3 = 1$ for describing the relevant dielectric permittivities. In Fig. 1.5a the light line for $\varepsilon_1 = 5$ is provided and it can be observed that the coupling with the SP branch is now possible. Fig. 1.7a shows the reflectance for an angle of incidence $\alpha = 0.7\pi/2$ as a function of frequency, ω, of the incident plane wave, for different values of the metal thickness d. For different thicknesses we have different plasmon resonance conditions, thus the resonance frequency is presented as dips in the reflection, redshifted as d increases.

1.2.3.2 Graphene layer

In Fig. 1.7b the reflectance is presented for excitation with the Otto configuration. The values of the dielectric permittivity for each layer are $\varepsilon_1 = 5$, $\varepsilon_2 = 1$ and $\varepsilon_3 = 5$. The graphene monolayer is lying at the interface between 2-3 media. The thickness of medium 2 is $d =$ 20 nm. In Fig. 1.7b the reflectance for a fixed angle of incidence, $\alpha = 0.8\pi/2$, is presented as a function of the frequency of the incident plane wave for different values of the chemical potential, μ. For the different values of the chemical potential, different SP resonances are evident, again corresponding to dips in the reflectance in Fig. 1.7b.

Comparing Fig. 1.7a and 1.7b it is observed that by changing the Au thickness, d, and the chemical potential, μ, of the graphene monolayer one can tune the plasmon resonance. On the other hand, the SP resonances for the Au slab lies in the visible part of the spectrum, while, for the graphene monolayer they lie in the infrared part of the spectrum.

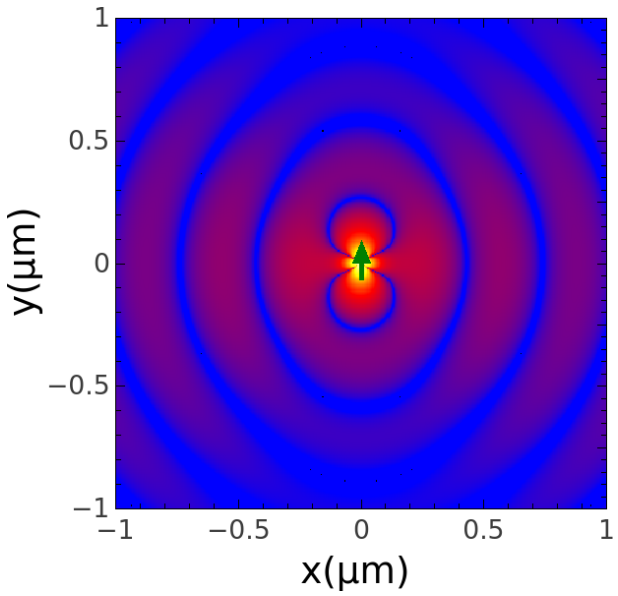

Figure 1.8: *Field distribution of a point dipole, with emission wavelength of* $\lambda = 600$ *nm. The point dipole orientation is implied by the green arrow.*

Exciting the SP modes on planar conducting nanostructures with a plane wave can prove non-trivial. The subject of this thesis is to investigate the interaction between quantum emitters in the presence of conducting nanostructures. The quantum emitters can directly excite the SP modes of the conducting nanostructures. This can be done by the direct coupling of the near field of the quantum emitters, which provides the large momentum k vectors, with the conducting nanostructures. Fig. 1.8 shows the field distribution of a quantum emitter, considered as a point dipole, with emission wavelength of $\lambda = 600$ nm. Close to the dipole position the field intensity is maximized and at distances larger than the emission wavelength it starts resembling a plane wave.

1.3 Structure of the thesis

In this thesis the interaction between quantum emitters and conducting nanostructures is explored. In particular we investigate planar and cylindrical metallic nanostructures, and an infinite graphene monolayer and a graphene nanodisk. These metallic and graphene nanostructures support SP modes.

In Chapter 2 the theoretical formalism used throughout this thesis is presented. The spontaneous emission and energy transfer rates are defined and their connection with the Green's tensor is presented. The integral representation of the free-space Green's tensor is given for cartesian and cylindrical coordinates.

In Chapter 3 the spontaneous emission and energy transfer function are investigated in the presence of a half space, dielectric-metal, and slab geometry, dielectric-metal-dielectric. The method of scattering superposition in cartesian coordinates is presented. The spectral and distance dependence of the spontaneous emission of a quantum emitter are analyzed. Contour plots of the energy transfer function between a pair of quantum emitters are presented when the donor quantum emitter is kept in a fixed position. The importance of the dispersion relation in explaining the spectral and distance dependence is presented. This chapter is used as an introductory chapter to study the SE and ET rates and how they are influenced by the SP modes provided the planar nanostructures.

In Chapter 4 the spontaneous emission and energy transfer rates in the presence of a dielectric coated metallic cylinder is studied. After analyzing the spectral and distance dependences of the spontaneous emission we present contour plots of the normalized energy transfer function. Using realistic parameters for the emission and absorption spectra of the quantum emitters, the energy transfer efficiency is investigated and the influence of the physical dimensions of the coated cylinder in enhancing the interaction distance between quantum emitters is presented.

In the last two chapters metallic nanostructures are considered. Metallic structures suffer from large losses, while graphene is a conducting two dimensional material with lower losses. In the next two chapters the spontaneous emission and energy transfer rates are investigated in the presence of gated graphene nanostructures.

In Chapter 5 the spontaneous emission and energy transfer rates in the presence of a gated graphene monolayer are studied. Long distance energy transfer efficiency is observed, supported by the graphene SP modes. The propagation length of the plasmon mode is found to characterize the energy transfer rate, between a pair of quantum emitters, along the graphene monolayer, while the penetration depth characterizes the interaction perpendicular to the graphene monolayer.

In Chapter 6 the influence in the spontaneous and energy transfer rates of the plasmon resonances encountered when the quantum emitters are in close proximity to a gated graphene nanodisk are investigated. The distance dependence of the interaction length between a pair of quantum emitters is analyzed and it is found to depend on the geometrical characteristics of the graphene nanodisk. Furthermore, the graphene nanodisk geometry is compared with a graphene monolayer regarding the perpendicular distance dependence of the interaction between the quantum emitters.

Finally, in Chapter 7 the main conclusions of the work presented are given and an outlook of the future steps that may be taken to further enhance and exploit the interaction distance

between quantum emitters are presented.

Chapter 2

Mathematical Introduction

2.1 Overview

In this chapter we introduce the main formalism used throughout this thesis to study the spontaneous emission (SE) rate of a single quantum emitter and the energy transfer (ET) rate between a pair of quantum emitters. A non-Hermitian quantum electrodynamic method is used, which takes account of lossy, plasmonic, materials, to calculate these rates. The plasmonic materials will be described by frequency dependent complex permittivity, $\varepsilon(\mathbf{r},\omega)$.

The main quantity needed to calculate the SE and ET rate is the Green's tensor [126, 135], a quantity that is calculated by solving the Maxwell equations of electrodynamics considering a point dipole excitation and thus can be directly connected with a quantum emitter.

We start by giving the quantum description of light-matter interactions in Sec. 2.2. A detailed derivation of the SE and ET rate and their connection with the Green's tensor is given in Sec. 2.3. Then the ET efficiency between a pair of quantum emitters is introduced in Sec. 2.4. This chapter is completed by giving the integral form of the Green's tensor in planar and cylindrical coordinates. These expressions will be used in the following chapters of the thesis.

2.2 Quantum electrodynamics

2.2.1 Classical electrodynamics

The classical description of electrodynamics is given by a set of differential equations connecting four vector quantities which describe the electromagnetic field: electric field intensity $\mathbf{E}(\mathbf{r},t)$, magnetic field intensity $\mathbf{H}(\mathbf{r},t)$, electric displacement $\mathbf{D}(\mathbf{r},t)$ and the magnetic induc-

tion $\mathbf{B}(\mathbf{r},t)$. The Maxwell's equations have the following form in the frequency domain [136]:

$$\nabla \times \mathbf{E}(\mathbf{r},\omega) = i\omega\mathbf{B}(\mathbf{r},\omega), \tag{2.1a}$$

$$\nabla \times \mathbf{H}(\mathbf{r},\omega) = -i\omega\mathbf{D}(\mathbf{r},\omega) + \mathbf{j}(\mathbf{r},\omega), \tag{2.1b}$$

$$\nabla \cdot \mathbf{D}(\mathbf{r},\omega) = \rho(\mathbf{r},\omega), \tag{2.1c}$$

$$\nabla \cdot \mathbf{B}(\mathbf{r},\omega) = 0, \tag{2.1d}$$

where $\rho(\mathbf{r},\omega)$ is the electromagnetic charge distribution and $\mathbf{j}(\mathbf{r},\omega)$ is the electric current distribution. The conservation of charge is implicitly contained in the Maxwell's equations. Taking the divergence of Eq. (2.1b) and substituting into Eq. (2.1c) we get the continuity equation

$$\nabla \cdot \mathbf{j}(\mathbf{r},\omega) - i\omega\rho(\mathbf{r},\omega) = 0, \tag{2.2}$$

for which charge and current distributions describe the external, free, charge and current distributions.

The electromagnetic properties of the medium are most commonly discussed in terms of the macroscopic polarization $\mathbf{P}$ and magnetization $\mathbf{M}$ according to

$$\mathbf{D}(\mathbf{r},\omega) = \varepsilon_0\mathbf{E}(\mathbf{r},\omega) + \mathbf{P}(\mathbf{r},\omega) \tag{2.3a}$$

$$\mathbf{H}(\mathbf{r},\omega) = \frac{1}{\mu_0}\mathbf{B}(\mathbf{r},\omega) - \mathbf{M}(\mathbf{r},\omega) \tag{2.3b}$$

where ε_0 and μ_0 are the permittivity and the permeability of vacuum, respectively. These expressions do not impose any conditions on the medium and are therefore always valid.

To account for free charges, bound up charges, currents and spins the field vectors $\mathbf{D}$ and $\mathbf{H}$ have been introduced, thus, describing the electromagnetic response to an external source. In this thesis only linear, isotropic, local and non-magnetic materials are considered, resulting in

$$\mathbf{D}(\mathbf{r},\omega) = \varepsilon_0\mathbf{E}(\mathbf{r},\omega) + \varepsilon_0 \int_0^\infty \mathrm{d}\tau\chi(\tau)\mathbf{E}(\mathbf{r}), \tag{2.4a}$$

$$\mathbf{B}(\mathbf{r},\omega) = \mu_0\mathbf{H}(\mathbf{r},\omega), \tag{2.4b}$$

where $\chi(\tau)$ is the linear electric susceptibility. Then Maxwell's equations will have the form

$$\nabla \times \mathbf{E}(\mathbf{r},\omega) - i\omega\mathbf{B}(\mathbf{r},\omega) = 0, \tag{2.5a}$$

$$\nabla \times \mathbf{B}(\mathbf{r},\omega) + i\frac{\omega}{c^2}\varepsilon(\omega)\mathbf{E}(\mathbf{r},\omega) = \mathbf{j}(\mathbf{r},\omega), \tag{2.5b}$$

$$\nabla \cdot [\varepsilon_0 \varepsilon(\omega)\mathbf{E}(\mathbf{r},\omega)] = \rho(\mathbf{r},\omega), \tag{2.5c}$$

$$\nabla \cdot \mathbf{B}(\mathbf{r},\omega) = 0, \tag{2.5d}$$

where c is the speed of light and the frequency dependent complex valued dielectric permittivity of the material is introduced,

$$\varepsilon(\omega) = 1 + \int_0^\infty \mathrm{d}\tau \chi(\tau) e^{i\omega\tau}, \tag{2.6}$$

where χ is the linear electric susceptibility.

In this thesis inhomogeneous materials, which will be considered as piece-wise homogeneous materials with abrupt transitions between them, are investigated. Boundary conditions will be applied at the transition between the material layers.

2.2.2 Quantization of the EM field in absorptive materials

Maxwell's equations, Eq. (2.5), together with the constitutive relations Eq. (2.4) can be written in terms of the electric $\hat{\mathbf{E}}$ and magnetic $\hat{\mathbf{B}}$ field operators as the quantum Maxwell's equations [54, 55]

$$\nabla \times \hat{\mathbf{E}}(\mathbf{r},\omega) - i\omega\hat{\mathbf{B}}(\mathbf{r},\omega) = 0, \tag{2.7a}$$

$$\nabla \times \hat{\mathbf{B}}(\mathbf{r},\omega) + i\frac{\omega}{c^2}\varepsilon(\omega)\hat{\mathbf{E}}(\mathbf{r},\omega) = \hat{\mathbf{j}}(\mathbf{r},\omega), \tag{2.7b}$$

$$\nabla \cdot [\varepsilon(\omega)\hat{\mathbf{D}}(\mathbf{r},\omega)] = \hat{\rho}(\mathbf{r},\omega), \tag{2.7c}$$

$$\nabla \cdot \hat{\mathbf{B}}(\mathbf{r},\omega) = 0, \tag{2.7d}$$

In a dielectric material, without average charge and current density, the new operators introduced in the above equations, $\hat{\rho}(\mathbf{r},\omega)$ and $\hat{\mathbf{j}}(\mathbf{r},\omega)$, represent the noise charge density and the noise current density operators, respectively. These noise operators account for absorption in the medium.

In the frequency domain, the electric field operator $\hat{\mathbf{E}}(\mathbf{r},\omega)$ satisfies an inhomogeneous Helmholtz equation of the form:

$$\nabla \times \nabla \times \hat{\mathbf{E}}(\mathbf{r},\omega) - \frac{\omega^2}{c^2}\varepsilon(\omega)\hat{\mathbf{E}}(\mathbf{r},\omega) = i\frac{\omega}{c^2\varepsilon_0}\hat{\mathbf{j}}(\mathbf{r},\omega), \tag{2.8}$$

whose solution can be written as:

$$\hat{\mathbf{E}}(\mathbf{r},\omega) = i\frac{\omega}{c^2\varepsilon_0}\int \mathrm{d}^3 s\, \mathfrak{G}(\mathbf{r},\mathbf{s},\omega)\cdot\hat{\mathbf{j}}(\mathbf{s},\omega), \tag{2.9}$$

where the Green's tensor $\mathfrak{G}(\mathbf{r},\mathbf{s},\omega)$ is introduced. The Green's tensor represents the electromagnetic response of a particular configuration of material bodies to a point-like excitation. $\mathfrak{G}$ is a 3×3 tensor which satisfies the equation:

$$\nabla\times\nabla\times\mathfrak{G}(\mathbf{r},\mathbf{s},\omega) - \frac{\omega^2}{c^2}\varepsilon(\omega)\mathfrak{G}(\mathbf{r},\mathbf{s},\omega) = \mathfrak{I}\delta(\mathbf{r}-\mathbf{s}), \tag{2.10}$$

$\mathbf{s}$ is the position of the point-like excitation and $\mathbf{r}$ is the position where the response to the point-like excitation is measured, $\mathfrak{I}$ is the unit 3×3 tensor.

In the Schrödinger picture the electric and magnetic field operators can be defined as:

$$\hat{\mathbf{E}}(\mathbf{r}) = \frac{1}{\sqrt{2\pi}}\int_0^\infty \mathrm{d}\omega\hat{\mathbf{E}}(\mathbf{r},\omega) + \text{h.c.}, \tag{2.11a}$$

$$\hat{\mathbf{B}}(\mathbf{r}) = \frac{1}{\sqrt{2\pi}}\int_0^\infty \mathrm{d}\omega\hat{\mathbf{B}}(\mathbf{r},\omega) + \text{h.c.}, \tag{2.11b}$$

and they satisfy the usual equal-time commutation relations of QED:

$$[\hat{E}_i(\mathbf{r}),\hat{E}_j(\mathbf{r}')] = [\hat{B}_i(\mathbf{r}),\hat{B}_j(\mathbf{r}')] = 0, \tag{2.12a}$$

$$\left[\hat{E}_i(\mathbf{r}),\hat{B}_j(\mathbf{r}')\right] = -\frac{i\hbar}{\varepsilon_0}\varepsilon_{ijk}\frac{\partial}{\partial x_k}\delta(\mathbf{r}-\mathbf{r}'). \tag{2.12b}$$

The source terms $\hat{\rho}$ and $\hat{\mathbf{j}}$ are closely related to the noise associated with the losses in the medium, which themselves are described by the imaginary part of the permittivity. The current noise operator $\hat{\mathbf{j}}(\mathbf{r},\omega)$ is expressed in terms of the bosonic vector field operator $\hat{\mathbf{f}}(\mathbf{r},\omega)$ as [59, 126]:

$$\hat{\mathbf{j}}(\mathbf{r},\omega) = \omega\sqrt{2\hbar\varepsilon_0\varepsilon''(\mathbf{r},\omega)}\hat{\mathbf{f}}(\mathbf{r},\omega), \tag{2.13}$$

where $\varepsilon''(\mathbf{r},\omega)$ is the imaginary part of the dielectric permittivity, Eq. 2.6. The components of the bosonic field satisfy the canonical commutation relations:

$$[\hat{f}_i(\mathbf{r},\omega),\hat{f}_j(\mathbf{r}',\omega')] = [\hat{f}_i^\dagger(\mathbf{r},\omega),\hat{f}_i^\dagger(\mathbf{r}',\omega')] = 0, \tag{2.14a}$$

$$[\hat{f}_i(\mathbf{r},\omega),\hat{f}_i^{\dagger}(\mathbf{r}',\omega')] = \delta_{ij}\delta(\omega-\omega')\delta(\mathbf{r}-\mathbf{r}'). \tag{2.14b}$$

The bosonic vector field operators, $\hat{\mathbf{f}}^{\dagger}$ and $\hat{\mathbf{f}}$, are creation and annihilation operators for medium-dressed states, which account for lossy surface modes, surface plasmon modes or far-field emission. The surface plasmon modes are the main subject of this thesis.

Using the bosonic vector field $\hat{\mathbf{f}}(\mathbf{r},\omega)$, the electric field operator $\hat{\mathbf{E}}(\mathbf{r})$ has the form:

$$\hat{\mathbf{E}}(\mathbf{r}) = i\sqrt{\frac{\hbar}{\pi\varepsilon_0}}\int_0^{\infty} \mathrm{d}\omega\, \frac{\omega^2}{c^2}\int \mathrm{d}^3 s\, \sqrt{\varepsilon''(\mathbf{s},\omega)}\, \mathfrak{G}(\mathbf{r},\mathbf{s},\omega)\cdot\hat{\mathbf{f}}(\mathbf{s},\omega) + \text{h.c.} \tag{2.15}$$

Calculating the energy density of the EM field, the radiation Hamiltonian is obtained as

$$\hat{H}_{\text{em}} = \frac{1}{2}\int \mathrm{d}^3 r[\hat{\mathbf{E}}(\mathbf{r})^2 + \hat{\mathbf{B}}(\mathbf{r})^2] = \int \mathrm{d}^3 r \int_0^{\infty} \mathrm{d}\omega\, \hbar\omega\, \hat{\mathbf{f}}^{\dagger}(\mathbf{r},\omega)\cdot\hat{\mathbf{f}}(\mathbf{r},\omega). \tag{2.16}$$

2.3 Spontaneous emission and energy transfer rate

Now a pair of two-level systems, A and B, located at $\mathbf{r}_A$ and $\mathbf{r}_B$, respectively, is considered [137]. The ground state of system $A(B)$ is denoted as $|g_A\rangle$ ($|g_B\rangle$) and the excited state as $|e_A\rangle$ ($|e_B\rangle$). The transition frequencies and dipole matrix element are denoted as $\omega_{A'A}$ ($\omega_{B'B}$) and $\mu_{A'A}$ ($\mu_{B'B}$), respectively.

The multipolar Hamiltonian is used to describe this system interacting with the electromagnetic field. In this description, direct Coulomb interactions between the two systems are absent. They interact via the electromagnetic field and the total Hamiltonian has the form

$$\hat{H} = \hat{H}_{\text{em}} + \hat{H}_{\text{qs}} + \hat{H}_{\text{int}}, \tag{2.17}$$

where the electromagnetic field Hamiltonian $\hat{H}_{\text{em}}$ has the form (2.16), the quantum system Hamiltonian is

$$\hat{H}_{\text{qs}} = \hbar\omega_{A'A}\sigma_A^{\dagger}\sigma_A + \hbar\omega_{B'B}\sigma_B^{\dagger}\sigma_B, \tag{2.18}$$

where $\sigma_A^{\dagger}$ and σ_A are the Pauli raising and lowering operators for system A (similar for system B) and the interaction Hamiltonian is

$$\hat{H}_{\text{int}} = -\hat{\mu}_A\hat{E}(r_A) - \hat{\mu}_B\hat{E}(r_B). \tag{2.19}$$

$\hat{\mu}_\alpha = \mu_\alpha \sigma_\alpha^\dagger + \mu_\alpha^* \sigma_\alpha^-$ is the dipole operator of the two level system α, $\alpha = A, B$, with μ_α being the transition dipole moment of the system between its ground and excited states.

The Hamiltonian (2.17) completely describes, in the electric dipole approximation, the interaction of a system of quantum emitters (atoms, molecules, quantum-dots or superconducting q-bits) with the electromagnetic field. The SE rate of a quantum emitter and the ET rate between a pair of quantum emitters will be the main quantities studied in this thesis and described through the Hamiltonian (2.17).

2.3.1 Spontaneous emission rate

The quantum emitter is described as a two-level quantum mechanical system, with transition frequency ω_0 between the ground and excited states $|0\rangle$ and $|1\rangle$, respectively. An excited quantum emitter interacts with its environment through the electromagnetic field and relaxes from its excited state, to the ground state, by emitting a photon or exciting any of the dressed states supported by its environment. The initial state of the system, $|i\rangle$, can be written as

$$|i\rangle = |e\rangle \otimes |0\rangle, \tag{2.20}$$

where the quantum emitter is in the excited state and the electromagnetic field is in its vacuum state. The quantum emitter system will not stay indefinitely excited, but will relax by emitting a photon and therefore the EM field will be in a $|1(\mathbf{k}, p)\rangle$ state; p and $\mathbf{k}$ are the polarization and wavevector, respectively. This state can be expressed by introducing the creation operator $\hat{f}_i^\dagger(\mathbf{r}, \omega)$ which acts on the vacuum state of the electromagnetic field produce the one excitation state. The final state of the entire system therefore has the form

$$|f\rangle = |g\rangle \otimes \hat{f}_i^\dagger(\mathbf{r}, \omega)|0\rangle. \tag{2.21}$$

Now the rate of passage from the initial to the final state is calculated. By applying Fermi's golden rule to this particular problem we get the following expression for the transition rate $|i\rangle \to |f\rangle$

$$w_{fi} = \frac{2\pi}{\hbar^2} |\langle f|\hat{T}|i\rangle|^2 \delta(\omega - \omega_0), \tag{2.22}$$

where ω_0 is the transition frequency of the quantum emitter and ω represents the frequency of the medium dressed electromagnetic excitation into which it decays. The Dirac δ-function ensures the conservation of energy in this process. The $\hat{T}$ operator is called the transition operator and it accounts for the relaxation of the quantum system. By considering the interac-

tion with the electromagnetic field as a small perturbation, this operator can be written, up to second order, as

$$\hat{T} = \hat{H}_{\text{int}} + \hat{H}_{\text{int}} \frac{1}{\hbar\omega_0 - \hat{H}_0 + i\eta^+} \hat{H}_{\text{int}}, \tag{2.23}$$

where $\hat{H}_0$ is the unperturbed part of the total Hamiltonian

$$\hat{H}_0 = \hat{H}_{\text{qs}} + \hat{H}_{\text{em}}, \tag{2.24}$$

η^+ is an infinitesimal small positive constant, and $\hbar\omega_0$ is the energy of the initial state. The energy of the final state is $\hbar\omega$, and the conservation of energy states that $\hbar\omega = \hbar\omega_0$.

Using the Eq. (2.21) and summing over all the final states the expression for the SE rate γ is obtained as:

$$\gamma = \sum_f w_{fi} = \int_0^\infty \mathrm{d}\omega \frac{2\omega^2}{\hbar\varepsilon_0 c^2} \mu_i \mathrm{Im}\mathfrak{G}_{ij}(\mathbf{r},\mathbf{r},\omega)\mu_j \delta(\omega-\omega_0) = \frac{2\omega^2}{\hbar\varepsilon_0 c^2} \mu_i \mathrm{Im}\mathfrak{G}_{ij}(\mathbf{r},\mathbf{r},\omega)\mu_j. \tag{2.25}$$

Throughout this thesis the emission rate of the quantum emitter in inhomogeneous media is expressed in units of the free-space emission rate γ_0 of the same two-level system. So we define the quantity

$$\tilde{\gamma} = \frac{\gamma}{\gamma_0}. \tag{2.26}$$

The expression for γ_0 is given by the Einstein A-coefficient:

$$\gamma_0 = \frac{\omega^3}{c^3\hbar\varepsilon_0} \frac{\mu^2}{3\pi}. \tag{2.27}$$

Later, in the next subsection, it is described how this expression is calculated. From the above expressions

$$\tilde{\gamma} = n + \frac{6\pi c}{\omega} \hat{\mu}_i \mathrm{Im}\,\mathfrak{G}_s^{ij}(\mathbf{r},\mathbf{r},\omega)\hat{\mu}_j, \tag{2.28}$$

is obtained, where n is the refractive index of the medium in which the two-level system is embedded, $\mathfrak{G}_s^{ij}$ is the scattering part of the Green's tensor and $\hat{\mu}_i = \mu_i/\mu$. The normalized SE $\tilde{\gamma}$ is used in this thesis as a measure of how much the material bodies influence the SE rate of a quantum system compared with its vacuum value.

When dealing with statistical ensembles of emitters, the emission spectrum will be different from that of a single emitter, which we have taken to have a δ shape. The emission rate for an ensemble can be expressed as:

$$k_{\mathrm{SE}} = \int_0^\infty \mathrm{d}\lambda f_D(\lambda)\gamma(\lambda), \tag{2.29}$$

where $f_{\mathrm{D}}(\lambda)$ is the area-normalized emission spectrum of the emitter, with $\int_0^\infty \mathrm{d}\lambda f_{\mathrm{D}}(\lambda) = 1$, and λ is the emission wavelength.

2.3.2 Resonance energy transfer rate

Next a pair of quantum systems, A and B, is considered and the ET between them is studied [54, 55, 137]. The initial state is

$$|i\rangle = |e_A\rangle \otimes |g_B\rangle \otimes |0\rangle, \tag{2.30}$$

where $|e\rangle$ and $|g\rangle$ are the excited and ground state of the quantum system, A and B, while $|0\rangle$ is the vacuum state of the electromagnetic field. In the final state system A has relaxed to the ground state, transferring its excitation energy to system B, which now is in the excited state; the electromagnetic field is still in the vacuum state:

$$|f\rangle = |g_A\rangle \otimes |e_B\rangle \otimes |0\rangle. \tag{2.31}$$

The quantity

$$\langle f|\hat{T}|i\rangle = \sum_{|\alpha\rangle} \langle f|\hat{H}_{\mathrm{int}} \frac{1}{E_i - \hat{H}_0 + i\eta^+} |\alpha\rangle\langle\alpha|\hat{H}_{\mathrm{int}}|i\rangle, \tag{2.32}$$

is computed, where the states $|\alpha\rangle$ over which we perform the summation, are of two types

$$|\alpha_I\rangle = |g_A\rangle \otimes |g_B\rangle \otimes \hat{f}_i^\dagger(\mathbf{s},\omega)|0\rangle, \tag{2.33a}$$

$$|\alpha_{II}\rangle = |e_A\rangle \otimes |e_B\rangle \otimes \hat{f}_i^\dagger(\mathbf{s},\omega)|0\rangle. \tag{2.33b}$$

For the Hamiltonian operators the expressions introduced above are used.

Second order perturbation theory is used for the transition operator and thus the expression

for the ET rate between two two-level has the form

$$\Gamma(\mathbf{r}_A,\mathbf{r}_B,\omega)=\frac{2\pi}{\hbar^2}\left(\frac{\omega_0^2}{c^2\varepsilon_0}\right)^2|\mathbf{d}_A\cdot\mathfrak{G}(\mathbf{r}_A,\mathbf{r}_B,\omega)\cdot\mathbf{d}_B|^2 \tag{2.34}$$

Again, the normalized ET rate is defined as the ratio between the ET rate in the nanostructured environment and the ET rate between the same two-level systems, at the same positions, but in free space. This quantity measures the effect of the presence of the nanostructure on the ET rate between the two two-level systems. The expression of interest has the form

$$\tilde{\Gamma}(\omega)=\frac{\Gamma(\omega)}{\Gamma_0(\omega)}=\frac{|\mathbf{d}_A\cdot\mathfrak{G}(\mathbf{r}_A,\mathbf{r}_B,\omega)\cdot\mathbf{d}_B|^2}{|\mathbf{d}_A\cdot\mathfrak{G}_0(\mathbf{r}_A,\mathbf{r}_B,\omega)\cdot\mathbf{d}_B|^2}, \tag{2.35}$$

where $\mathfrak{G}_0(\mathbf{r}_A,\mathbf{r}_B,\omega)$ is the Green's tensor in free space. The importance of the Green's tensor in calculating the SE and ET rates needs to be stressed again since this quantity encapsulates all the information on the response of material bodies to electromagnetic fields. The knowledge of the Green's tensor is an important element in order to calculate various quantities such as: a low energy electron beam interacting with nanostructures [83, 128], the heat distribution created by a quantum emitter [138, 139] and the trapping potential interacting with a quantum emitter [135]. In the following chapters we present a method for calculating the Green's tensor in planar and cylindrical geometries.

Analogously to the case of the SE rate, when considering statistical ensembles of donors and acceptors, the donor emission spectrum $f_{\mathrm{D}}(\lambda)$ and acceptor absorption cross-section $\sigma_{\mathrm{A}}(\lambda)$ need to be taken into account when calculating the ET rate,

$$k_{\mathrm{ET}}=36\pi^2 Y_D k_{\mathrm{SE}}\int_0^\infty\frac{\mathrm{d}\lambda}{\lambda^2}f_{\mathrm{D}}(\lambda)\,|\mathbf{n}_{\mathrm{A}}\cdot\mathfrak{G}(\mathbf{r}_{\mathrm{A}},\mathbf{r}_{\mathrm{D}},\omega)\cdot\mathbf{n}_{\mathrm{D}}|^2\sigma_{\mathrm{A}}(\lambda), \tag{2.36}$$

where k_{SE} is given by Eq. (2.29) and Y_D is the intrinsic quantum yield of the donor QE [130]. This expression is used in order to calculate the ET rate between donors and acceptors with specific emission and absorption spectra and to investigate how the energy process competes with the emission process of the donor.

2.4 Energy transfer efficiency between quantum emitters

The ET between particles plays a crucial role in photophysical processes such as light harvesting proteins in photosynthetic membranes. The optical energy absorbed by chlorophyll molecules has to be channeled over large distances to a protein called the reaction center. ET can be also observed between closely arranged semiconductor nanoparticles (although we will see at the end of this thesis they are ways to expand this interaction distance), and is the basis of Förster energy-transfer (FRET) studies of biological processes.

In the previous section the SE rate, Eq. (2.29), of a single quantum emitter and the ET rate, Eq. (2.36), between a pair of quantum emitters were introduced. An excited donor has two ways of relaxing: it can either transfer its excitation energy to the acceptor dipole with an ET rate k_{ET}, or it can relax with decay rate k_{SE}, where no nonradiative internal decay is assumed, in other words the intrinsic quantum yield of the donor quantum emitter is $Y_0 = 1$ [130, 140]. The decay rate, k_{SE}, takes account of photon emission into the far field, coupling to surface plasmon modes or to Ohmic losses of no propagating nature. The SE and ET processes are, therefore, in competition.

The ET efficiency η is defined as

$$\eta = \frac{k_{\mathrm{ET}}}{k_{\mathrm{SE}} + k_{\mathrm{ET}}}. \tag{2.37}$$

This quantity gives the relative contribution of the ET process to the total decay rate of the donor quantum emitter. If the ET efficiency, η, has a value $\eta > 50\%$, then the decay of the excited state of donor quantum emitter occurs mainly by ET to the acceptor, rather than relaxation into photon or surface plasmon modes.

The donor quantum emitter's emission and the acceptor quantum emitter's absorption spectra are both described by Gaussian distributions of the form:

$$A_{\mathrm{q}}\, \mathrm{e}^{-(\lambda-\lambda_{\mathrm{q}})^2/\Delta\lambda_{\mathrm{q}}^2}, \tag{2.38}$$

where $q = \mathrm{D}, \mathrm{A}$ represents the donor or acceptor quantum emitter, respectively. A_q is a normalization constant, λ_q gives the position of the spectral peak and $\Delta\lambda_q$ is related to the full width at half maximum of the spectrum.

In order to calculate the SE rate, Eq. (2.29), and the ET rate, Eq. (2.36), knowledge of the

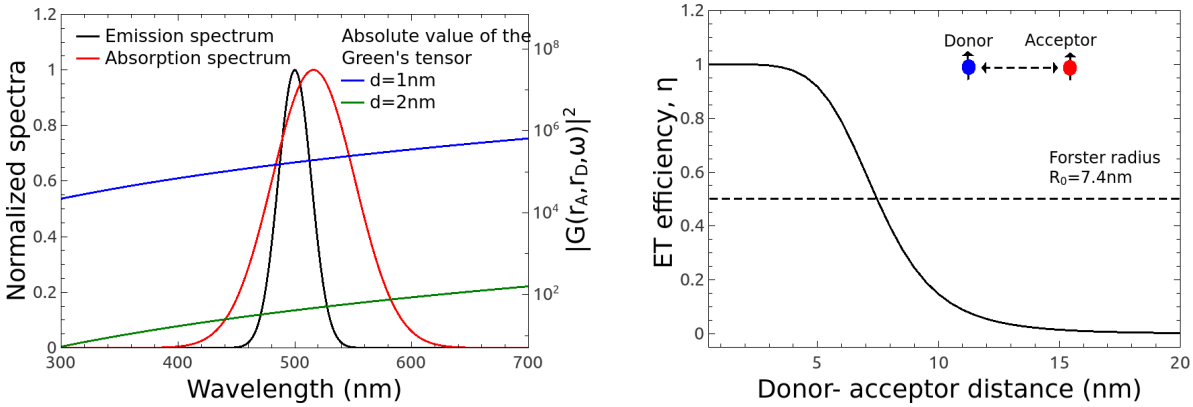

Figure 2.1: *(a) Normalized donor emission and acceptor absorption spectra and the field intensity, for two donor-acceptor separations, as a function of wavelength. (b) ET efficiency as a function of the donor-acceptor distance, the donor emission and acceptor absorption of (a) are used.*

Green's tensor is needed, which in free space has the form

$$\mathfrak{G}_h^{ij}(\mathbf{r}_\mathrm{A},\mathbf{r}_\mathrm{D},\omega) = -\frac{1}{k^2}\frac{e^{ikR}}{4\pi R^3}[(1-ikR)(\delta_{ij}-3\hat{R}_i\hat{R}_j)-k^2R^2(\delta_{ij}-\hat{R}_i\hat{R}_j)] \tag{2.39}$$

where $\mathbf{R} = \mathbf{r}_\mathrm{A} - \mathbf{r}_\mathrm{D}$ is the relative distance between the donor and the acceptor, and $k = \omega/c$ is the emission wavenumber [141].

A very important parameter characterizing the interaction length is the Förster radius, R_0, which is defined as the donor-acceptor separation at which the ET efficiency η is 50% [52]. The Förster radius can be calculated from the spectral overlap of the normalized donor emission, f_D, and the acceptor absorption, σ_A, spectra as

$$R_0 = \left[\frac{3c}{32\pi^4 n^4}\int_0^\infty \mathrm{d}\lambda\,\lambda^2 f_\mathrm{D}(\lambda)\,\sigma_\mathrm{A}(\lambda)\right]^{1/6} \tag{2.40}$$

where n is the refractive index of the host medium.

In order to better illustrate the form of the interaction a specific pair of quantum emitter spectra is considered. The emission peak is at $\lambda_\mathrm{D} = 500\,\mathrm{nm}$ and the acceptor absorption maximum at $\lambda_\mathrm{A} = 516\,\mathrm{nm}$. The normalization constant of the donor emission is given by $A_\mathrm{D}^{-1} = \int_0^\infty \mathrm{d}\lambda f_D(\lambda)$. The normalization constant for the acceptor absorption spectrum is $A_\mathrm{A} = 0.021\,\mathrm{nm}^2$, while the width is $\Delta\lambda_\mathrm{A} = 50\,\mathrm{nm}$. The ET rate, Eq (2.36), is given by the overlap integral between the donor emission and the acceptor absorption spectra with the absolute value of the Green's tensor, Eq. (2.39). In Fig. 2.1a the normalized donor emission

and acceptor absorption spectra are presented, and a strong overlap can be seen. In the same figure, Fig. 2.1a, the field intensity is presented for two different distances between the donor and the acceptor as a function of emission wavelength of the donor. Eq. (2.39) shows that the field strength falls as r^{-6} as the distance between them is increased. Thus, the ET rate decreases quickly as the distance between the donor-acceptor is increased. In Fig. 2.1b the ET efficiency is presented for the aforementioned pair of quantum emitters. It can be seen that the Förster radius, calculated from Eq. (2.40), has a value $R_0 = 7.4\,\text{nm}$. This shows that the interaction distance is very short, and this value has been obtained under the assumption that the quantum yield is $Y = 1$. In this thesis some methods for enhancing this interaction distance are presented.

2.5 Integral form of the Green's tensor

From Eq. (2.25) and (2.34) it is evident how crucial is the knowledge of the Green's tensor for calculating the SE and the ET rates . In this section the integral form of the Green's tensor is given for the case of Cartesian and Cylindrical coordinates [141,142], obtaining expressions that will be used in the following chapters of the thesis.

2.5.1 The Green's tensor in Cartesian coordinates

In order to calculate the Green's tensor in Cartesian coordinates, the vacuum case is firstly considered, $\varepsilon(\omega) = 1$. The differential equation for the Green's tensor has the form

$$\nabla_{\mathbf{r}} \times \nabla_{\mathbf{r}} \times \mathfrak{G}(\mathbf{r},\mathbf{s},\omega) - \frac{\omega^2}{c^2}\mathfrak{G}(\mathbf{r},\mathbf{s},\omega) = \mathfrak{I}\delta(\mathbf{r}-\mathbf{s}), \tag{2.41}$$

with the differential operators acting on $\mathbf{r}$. The goal would be to find an expansion of the Green's tensor in terms of the vector wave functions (VWFs) in Cartesian coordinates. These VWFs are solutions of the homogeneous Helmholtz equation in Cartesian coordinates:

$$\nabla \times \nabla \times \mathbf{F}(\mathbf{k},\mathbf{r}) - k^2\mathbf{F}(\mathbf{k},\mathbf{r}) = 0, \tag{2.42}$$

where $k^2 = k_x^2 + k_y^2 + k_z^2$ denotes the eigenvalue of the differential operator $\nabla \times \nabla \times$. One can construct the VWFs solutions from the corresponding scalar Helmholtz equation

$$\nabla^2\psi(\mathbf{k},\mathbf{r}) + k^2\psi(\mathbf{k},\mathbf{r}) = 0, \tag{2.43}$$

which have a plane-wave form

$$\psi(\mathbf{k},\mathbf{r}) = \mathrm{e}^{i\mathbf{k}\cdot\mathbf{r}}, \tag{2.44}$$

as follows:

$$\mathbf{M}(\mathbf{k},\mathbf{r}) = \nabla\times[\psi(\mathbf{k},\mathbf{r})\hat{\mathbf{z}}] = i(\mathbf{k}\times\hat{\mathbf{z}})\mathrm{e}^{i\mathbf{k}\cdot\mathbf{r}}, \tag{2.45a}$$

$$\mathbf{N}(\mathbf{k},\mathbf{r}) = \frac{1}{k}\nabla\times\nabla\times[\psi(\mathbf{k},\mathbf{r})\hat{\mathbf{z}}] = -\frac{1}{k}\mathbf{k}\times(\mathbf{k}\times\hat{\mathbf{z}})\mathrm{e}^{i\mathbf{k}\cdot\mathbf{r}}, \tag{2.45b}$$

$$\mathbf{L}(\mathbf{k},\mathbf{r}) = \nabla\psi(\mathbf{k},\mathbf{r}) = i\mathbf{k}\,\mathrm{e}^{i\mathbf{k}\cdot\mathbf{r}}. \tag{2.45c}$$

It can be shown that these VWFs form an orthogonal and complete set of eigenfunctions, which means that one can expand the Green's tensor as follows

$$\mathfrak{G}(\mathbf{r},\mathbf{s},\omega) = \frac{1}{2\pi^3}\int \mathrm{d}^3k\left[\frac{\mathbf{M}(\mathbf{k},\mathbf{r})\otimes\hat{\mathbf{M}}(-\mathbf{k},\mathbf{s})}{k_s^2(k^2-k_0^2)} + \frac{\mathbf{N}(\mathbf{k},\mathbf{r})\otimes\hat{\mathbf{N}}(-\mathbf{k},\mathbf{s})}{k_s^2(k^2-k_0^2)} - \frac{\mathbf{L}(\mathbf{k},\mathbf{r})\otimes\hat{\mathbf{L}}(-\mathbf{k},\mathbf{s})}{k_s^2k_0^2}\right], \tag{2.46}$$

where $k_0 = \omega/c$ and $k_s^2 = k_x^2 + k_y^2$. We can further simplify this expression by performing the integrals over k_z. Each of the terms has a number of poles in the complex k_z plane. The **M**-term has poles at $k_z = \pm\sqrt{\omega^2 - k_s^2}$. The **N**-term also has poles at $k_z = \pm\sqrt{\omega^2 - k_s^2}$, as well as a static pole at $k_z = \pm ik_s$. The static pole exactly cancel the contribution from the poles coming from the **L**-term. Performing these integrations we are left with a two-dimensional integral for the Green's tensor

$$\begin{aligned}\mathfrak{G}(r,s,\omega) = &-\frac{\delta(\mathbf{r}-\mathbf{s})}{k_0^2}\hat{\mathbf{z}}\otimes\hat{\mathbf{z}} + \frac{i}{8\pi^2}\int \mathrm{d}^2k_s\frac{1}{k_zk_s^2}\left[\mathbf{M}(\mathbf{k}_s,\pm k_z,\mathbf{r})\otimes\mathbf{M}^*(\mathbf{k}_s,\pm k_z,\mathbf{s}) + \right.\\ &\left.+\mathbf{N}(\mathbf{k}_s,\pm k_z,\mathbf{r})\otimes\mathbf{N}^*(\mathbf{k}_s,\pm k_z,\mathbf{s})\right], \qquad z \lessgtr z_s,\end{aligned} \tag{2.47}$$

where z_s is the z-component of the source position vector **s**. This is the free space Green's tensor, the field created by a dipole source in the absence of material bodies.

2.5.2 The Green's tensor in cylindrical coordinates

The same method as illustrated in section 2.5 is used to solve Eq. (2.41) in cylindrical coordinates by expanding the Green's tensor in the appropriate basis of VWFs [141, 142].

Eq. (2.43) in cylindrical coordinates has the form

$$\left(\frac{\partial^2}{\partial\rho^2}+\frac{1}{\rho}\frac{\partial}{\partial\rho}+\frac{1}{\rho^2}\frac{\partial^2}{\partial\theta^2}+\frac{\partial^2}{\partial z^2}+k^2\right)\psi(\mathbf{k},\mathbf{r})=0, \tag{2.48}$$

where $\mathbf{r}=(\rho,\theta,z)$ in cylindrical coordinates. The solution to this equation is

$$\psi_n(k_\rho,k_z,\mathbf{r})=J_n(k_\rho\rho)e^{in\theta}e^{ik_z z}, \tag{2.49}$$

where $J_n(k_\rho\rho)$ are the regular Bessel functions of first kind and integer order n, which are regular at the origin. Now the solution of Eq. (2.42) is constructed by using Eq. (2.45), resulting in

$$\mathbf{M}_n(k_\rho,k_z,\mathbf{r})=\nabla\times\psi_n(k_\rho,k_z,\mathbf{r})\hat{\boldsymbol{\rho}}=\left(\frac{in}{\rho}J_n(k_\rho\rho)\hat{\boldsymbol{\rho}}-\frac{\partial J_n(k_\rho\rho)}{\partial\rho}\hat{\boldsymbol{\theta}}\right)e^{in\theta}e^{ik_z z}, \tag{2.50}$$

$$\mathbf{N}_n(k_\rho,k_z,\mathbf{r})=\frac{1}{k}\nabla\times\nabla\times\psi_n(k_\rho,k_z,\mathbf{r})\hat{\boldsymbol{\rho}}=\frac{1}{k}\left(ik_z\frac{\partial J_n(k_\rho\rho)}{\partial\rho}\hat{\boldsymbol{\rho}}-\frac{nk_z}{\rho}\hat{\boldsymbol{\theta}}+k_\rho^2 J_n(k_\rho\rho)\hat{z}\right)e^{in\theta}e^{ik_z z}, \tag{2.51}$$

$$\mathbf{L}_n(k_\rho,k_z,\mathbf{r})=\nabla\psi_n(k_\rho,k_z,\mathbf{r})=\left(\frac{\partial J_n(k_\rho\rho)}{\partial\rho}\hat{\boldsymbol{\rho}}+\frac{in}{\rho}J_n(k_\rho\rho)\hat{\boldsymbol{\theta}}+ik_z J_n(k_\rho\rho)\hat{z}\right)e^{in\theta}e^{ik_z z}. \tag{2.52}$$

These VWFs form an orthogonal complete set. The Green's tensor is expressed in cylindrical coordinates as

$$\mathfrak{G}(\mathbf{r},\mathbf{s},\omega)=\frac{\delta(\mathbf{r}-\mathbf{s})}{k_0^2}\hat{\boldsymbol{\rho}}\otimes\hat{\boldsymbol{\rho}}+\frac{i}{8\pi}\sum_{n=-\infty}^{\infty}\int_{-\infty}^{\infty}\mathrm{d}k_z\frac{1}{k_\rho^2}W_n(k_z,\mathbf{r},\mathbf{s}), \tag{2.53}$$

with

$$W_n(k_z,\mathbf{r},\mathbf{s})=\mathbf{M}_n^{(1)}(k_\rho,k_z,\mathbf{r})\otimes\hat{\mathbf{M}}_n(k_\rho,k_z,\mathbf{r})+\mathbf{N}_n^{(1)}(k_\rho,k_z,\mathbf{r})\otimes\hat{\mathbf{N}}_n(k_\rho,k_z,\mathbf{r}),\quad \rho>\rho_s, \tag{2.54a}$$

$$W_n(k_z,\mathbf{r},\mathbf{s})=\mathbf{M}_n(k_\rho,k_z,\mathbf{r})\otimes\hat{\mathbf{M}}_n^{(1)}(k_\rho,k_z,\mathbf{r})+\mathbf{N}_n(k_\rho,k_z,\mathbf{r})\otimes\hat{\mathbf{N}}_n^{(1)}(k_\rho,k_z,\mathbf{r}),\quad \rho<\rho_s. \tag{2.54b}$$

where $k_\rho=\sqrt{k^2-k_z^2}$, $k=\frac{\omega}{c}\sqrt{\varepsilon}$. The notation is introduced in a similar manner to section 2.5.1. The vector wave functions now are expanded in basis of Bessel and Hankel functions. The superscript (1), e.g. $\mathbf{M}_n^{(1)}(k_\rho,k_z,\omega)$, denotes that the Hankel functions of the first kind should be used.

One should emphasize the fact that the expressions given by Eq. (2.39), (2.47) and (2.53)

are completely equivalent. Until this point the field created by a quantum emitter in a homogeneous medium, in particular free space, is considered. For the rest of the thesis piece-wise non-homogeneous material bodies are considered and the main goal is to find ways for enhancing the interaction distance between quantum emitters. This is a crucial effect from the point of view of applications.

Chapter 3

Planar Multilayer Geometries

3.1 Introduction

The interaction between quantum emitters and multilayer planar structures is the simplest and thus the first that has been investigated, both experimentally [3,24,53,70] and theoretically [4, 9, 27, 28, 58, 143], in depth. Thus it will be instructive from a pedagogical point of view to investigate in this chapter the spontaneous emission (SE) rate, of a single quantum emitter, and the energy transfer (ET) rate, between a pair of quantum emitters, in the presence of planar multilayer geometries. In particular, the influence on the SE and ET rates of the excitation of surface plasmon (SP) modes is investigated. The SP modes are collective oscillations of electrons and the electromagnetic field that can be excited at the interface between a dielectric and a conductor.

In this chapter the focus is on two geometries: the planar single interface geometry, between a dielectric and a conductor, and a metallic slab in a dielectric host. The metallic slab geometry is interesting from an application point of view. Our investigation is concentrated on the SE and ET rates and it is observed that these rates are enhanced several orders of magnitude compared with the free-space values. The importance of knowing the dispersion relation [16, 144], the relation between the frequency and the in-plane wavevector, will be apparent. The spectral and distance dependences of a single quantum emitter interacting with the planar geometries are explained through the dispersion relation. The penetration depth characterizes the perpendicular distance dependence of the interaction distance between QEs and multilayer planar geometries. Furthermore, the propagation length characterizes the parallel to the metal/dielectric distance dependence of the interaction distance, between QEs in the presence of planar multilayer structures.

In this chapter the method of scattering superposition, Sec. 3.2, is introduced for calculating

the Green's tensor. Then, this method is applied for calculating the Green's tensor for the single interface and slab geometry, Sec. 3.3. In the same section the SE and ET rates are investigated. In Sec. 3.4 the main points summarized and conclusions are drawn.

3.2 Method of scattering superposition for planar geometries

A multilayer planar geometry is considered consisting of a number of N layers, which are indexed by their layer number $i = 1,\ldots,N$ where each layer has thickness d_i and dielectric permittivity ε_i. The layers are of infinite extent in the xy plane and the z axis is perpendicular to the surface of each layer. As we have seen in section 2.3, in order to calculate the SE and ET rates we have to calculate the Green's tensor for a particular geometry.

The method of scattering superposition is used [141, 142, 145] where the Green's tensor splits into two parts

$$\mathfrak{G}(\mathbf{r},\mathbf{s},\omega) = \mathfrak{G}_h(\mathbf{r},\mathbf{s},\omega) + \mathfrak{G}_s(\mathbf{r},\mathbf{s},\omega), \tag{3.1}$$

where $\mathfrak{G}_h(\mathbf{r},\mathbf{s},\omega)$ is the homogeneous part that accounts for direct interaction between the source and target point at $\mathbf{s}$ and $\mathbf{r}$ respectively, and is non zero when both points are in the same media and there is no discontinuity between them, see Eq. (2.39). $\mathfrak{G}_s(\mathbf{r},\mathbf{s},\omega)$ is the scattering part, is always present and accounts for the multiple reflections and transmissions taking place at the interfaces.

The general form of the scattering part of the Green's tensor has the form

$$\mathfrak{G}_s(\mathbf{r},\mathbf{s},\omega) = \frac{i}{8\pi^2}\int \mathrm{d}^2k_s \frac{1}{k_{zi}k_s^2}\sum_T R_T^{\pm(ij)\pm}\mathbf{T}(\mathbf{k}_s,\pm k_{zi},\mathbf{r})\otimes\mathbf{T}^*(\mathbf{k}_s,\pm k_{zj},\mathbf{s}). \tag{3.2}$$

A summation is implied for each pair of $\pm$ indices. These indices show the direction of propagation of the electromagnetic modes, the first index for the acceptor and the second for the donor. Also the summation over $\mathbf{T}$ is over the $\mathbf{M}$ and $\mathbf{N}$ modes which are connected with the transverse electric and transverse magnetic modes, respectively. For the planar geometries there are no hybrid modes. The boundary conditions imposed on the system of multilayers are the continuity condition and the radiation condition. The first condition is denoted by continuity equations at each interface:

$$\hat{\mathbf{z}}\times\left[\mathfrak{G}^{(ij)}(\mathbf{r},\mathbf{s},\omega) - \mathfrak{G}^{((i+1)j)}(\mathbf{r},\mathbf{s},\omega)\right]\Big|_{z=d_i} = 0, \tag{3.3a}$$

$$\hat{\mathbf{z}} \times \left[\nabla \times \mathfrak{G}^{(ij)}(\mathbf{r},\mathbf{s},\omega) - \nabla \times \mathfrak{G}^{((i+1)j)}(\mathbf{r},\mathbf{s},\omega) \right] \Big|_{z=d_i} = 0. \tag{3.3b}$$

By applying these boundary equations an inhomogeneous system of 2^{N-1} equations is defined which have 2^{N-1} unknowns, the generalized $R_{M(N)}^{\pm(ij)\pm}$ coefficients. These coefficients are sufficient to uniquely determined the problem under consideration through the exact knowledge of the scattering part of the Green's tensor. Using equations (2.28) and (2.35) the spontaneous emission and resonance energy transfer rates, γ and Γ, respectively, are calculated.

In order to find the generalized coefficients a matrix equation is solved which has the form

$$\Delta_{M(N)} \cdot R_{M(N)}^{(i)\pm} = V_{M(N)}^{(i)\pm}, \tag{3.4}$$

where Δ is the characteristic matrix of the system of equations from the boundary conditions at the interfaces, $R^{(i)\pm}$ is the column of the generalized coefficients $R_{M(N)}^{\pm(ij)\pm}$ and $V^{(i)\pm}$ is the free term vector whose terms are given by the homogeneous part of the Green's tensor.

3.3 Spontaneous emission and energy transfer rates

In this section the spontaneous emission and energy transfer rates are investigated for the half space and slab geometries. The full expressions regarding the calculation of the generalized Fresnel coefficients are given using the method of scattering superposition developed in Sec. 3.2. Then, calculating the scattering part of the Green's tensor the SE and ET rates are calculated using the formalism developed in Sec. 2.3.

3.3.1 The half space geometry

In this subsection the simplest geometry supporting SP modes is considered, a planar interface between two half-spaces: a dielectric and a metal, Fig. 3.1a. The space for $z > 0$ is filled by a dielectric material with dielectric constant ε_1, while the region with $z < 0$ is occupied by a metal, having a frequency-dependent, complex permittivity, $\varepsilon_2(\omega)$. In this chapter we use a Drude permittivity for the metal given by:

$$\varepsilon_2(\omega) = 1 - \frac{\omega_p^2}{\omega^2 + i\omega\gamma}, \tag{3.5}$$

ω_p is the plasma frequency for the metal and γ is the linewidth which accounts for ohmic losses in the metal.

This subsection presents how the scattering part of the Green's tensor is constructed, Eq. (3.2),

by applying the boundary conditions Eq. (3.3). Due to the form of the geometry the choice of Cartesian coordinates is natural, see Sec. 2.5.1. The case where the quantum emitter is placed in medium 1 is considered. The VWFs form a complete set of eigenfunctions, thus, the scattering term has the form [141, 142]:

$$\mathfrak{G}_s^{(11)}(\mathbf{r},\mathbf{s},\omega) = \frac{i}{8\pi^2}\int \mathrm{d}^2k_\rho \frac{1}{k_{z1}k_\rho^2}\Big(R_M^{+11-}\mathbf{M}(k_\rho,k_{z1},\mathbf{r})\otimes\mathbf{M}^*(k_\rho,-k_{z1},\mathbf{s}) + \\ + R_N^{+11-}\mathbf{N}(k_\rho,k_{z1},\mathbf{r})\otimes\mathbf{N}^*(k_\rho,-k_{z1},\mathbf{s})\Big) \tag{3.6a}$$

$$\mathfrak{G}_s^{(21)}(\mathbf{r},\mathbf{s},\omega) = \frac{i}{8\pi^2}\int \mathrm{d}^2k_\rho \frac{1}{k_{z1}k_\rho^2}\Big(R_M^{-11-}\mathbf{M}(k_\rho,-k_{z2},\mathbf{r})\otimes\mathbf{M}^*(k_\rho,-k_{z1},\mathbf{s}) + \\ + R_N^{-11-}\mathbf{N}(k_\rho,-k_{z2},\mathbf{r})\otimes\mathbf{N}^*(k_\rho,-k_{z1},\mathbf{s})\Big) \tag{3.6b}$$

where $k_{zi} = \sqrt{k_i^2 - k_\rho^2}$ is the in-plane propagation constant and $k_i = \omega/c\sqrt{\varepsilon_i}$ is the wavenumber in medium i $(i = 1,2)$. We have already applied the radiation condition. This condition ensures that there are no incoming waves from $z \to \pm\infty$ as there are no scatterers there.

The R coefficients are calculated by applying the boundary conditions at $z = 0$, where the continuity of the tangential component of the electric field $\mathbf{E}$ and the normal component of the magnetic field $\mathbf{B}$ translates into the following conditions in terms of the Green's tensor

$$\hat{z}\times\Big[\mathfrak{G}^{(21)}(\mathbf{r},\mathbf{s},\omega) - \mathfrak{G}^{(11)}(\mathbf{r},\mathbf{s},\omega)\Big]_{z=0} = 0, \tag{3.7a}$$

$$\hat{z}\times\Big[\nabla\times\mathfrak{G}^{(21)}(\mathbf{r},\mathbf{s},\omega) - \nabla\times\mathfrak{G}^{(11)}(\mathbf{r},\mathbf{s},\omega)\Big]_{z=0} = 0. \tag{3.7b}$$

The continuity conditions Eq. (3.7) can then be written in matrix form as

$$\Delta_{M(N)}\cdot\mathbf{R}_{M(N)} = \mathbf{V}_{M(N)}, \tag{3.8}$$

where the characteristic matrices for the two polarizations, TE and TM, have the form,

$$\Delta_M = \begin{pmatrix} 1 & -1 \\ k_{z1} & k_{z2} \end{pmatrix}, \quad \Delta_N = \begin{pmatrix} \frac{k_{z1}}{k_1} & \frac{k_{z2}}{k_2} \\ k_1 & k_2 \end{pmatrix}, \tag{3.9}$$

the unknown coefficients vectors are,

$$\mathbf{R}_M = \begin{pmatrix} R_M^{+(11)-} \\ R_M^{-(21)-} \end{pmatrix}, \quad \mathbf{R}_N = \begin{pmatrix} R_N^{+(11)-} \\ R_N^{-(21)-} \end{pmatrix}, \tag{3.10}$$

and the free-vectors

$$\mathbf{V}_M = \begin{pmatrix} -1 \\ k_{z1} \end{pmatrix}, \quad \mathbf{V}_N = \begin{pmatrix} 1 \\ k_{z2} \end{pmatrix}, \tag{3.11}$$

The usual Fresnel coefficients are the solution of Eq. (3.8):

$$R_M^{+(11)-} = \frac{k_{z1} - k_{z2}}{k_{z1} + k_{z2}}, \quad R_M^{-(21)-} = \frac{2k_{z1}}{k_{z1} + k_{z2}}, \tag{3.12}$$

$$R_N^{+(11)-} = \frac{\varepsilon_2 k_{z1} - \varepsilon_1 k_{z2}}{\varepsilon_2 k_{z1} + \varepsilon_1 k_{z2}}, \quad R_N^{-(21)-} = \frac{2\sqrt{\varepsilon_1}\sqrt{\varepsilon_2} k_{z1}}{\varepsilon_2 k_{z1} + \varepsilon_1 k_{z2}}. \tag{3.13}$$

The SP modes are now discussed. The SP modes are purely TM in nature and are obtained by requiring the $\det(\Delta_N) = 0$ which leads to the expression

$$\varepsilon_2 k_{z1} + \varepsilon_1 k_{z2} = 0. \tag{3.14}$$

The z- components of the wavevector, k_{z1} and k_{z2}, are given by $k_{zi} = \sqrt{k_i^2 - k_\rho^2}$, $i = 1,2$, which leads to

$$k_\rho = \frac{\omega}{c}\sqrt{\frac{\varepsilon_1 \varepsilon_2}{\varepsilon_1 + \varepsilon_2}}, \tag{3.15}$$

the dispersion relation. The electric field is evanescent along the z-direction in both media, with

$$k_{z1} = \frac{\omega}{c}\sqrt{\frac{\varepsilon_1^2}{\varepsilon_1 + \varepsilon_2}}, \quad k_{z2} = \frac{\omega}{c}\sqrt{\frac{\varepsilon_2^2}{\varepsilon_1 + \varepsilon_2}}, \tag{3.16}$$

pictured in Fig. 3.1a. In case that the metal losses are ignored, $\gamma = 0$, then the physical conditions for the existence of SP modes are that they propagate along the interface, i.e. k_ρ is real, and decay away from the interface between metal-dielectric, k_{zi} imaginary. Then using Eq. (3.5) the SP modes are in the range $\omega \in (0, \omega_{\mathrm{SP}})$, where $\omega_{\mathrm{SP}} = \omega_{\mathrm{P}}/\sqrt{1+\varepsilon_1}$ is the surface plasmon frequency. By increasing the value of the permittivity of the dielectric medium then the SP frequency is redshifted.

In Fig. 3.1b the modes supported by a planar metal-dielectric interface are considered [16, 144]. The dielectric permittivity has a value of $\varepsilon_1 = 2$ and the value of the plasma frequency $\omega_p = 8\,\mathrm{fs}^{-1}$, also $\gamma = 0$. The SP frequency has a value of $\omega_{\mathrm{SP}} = 4.6\,\mathrm{fs}^{-1}$, and the SP branch asymptotically tends to this value. The SP branch is in the $(0, \omega_{\mathrm{SP}})$ and lies beneath the light-line in medium 1, thus the SP modes cannot be excited by direct plane wave illumination. In the region between $(\omega_{\mathrm{SP}}, \omega_p)$ there are no modes, this is the stop-gap region. Finally, in the (ω_p, ∞) region the modes are radiative and propagate freely in both media.

Using all the above expressions, the scattering part of the Green's tensor, Eq. (3.6), is calcu-

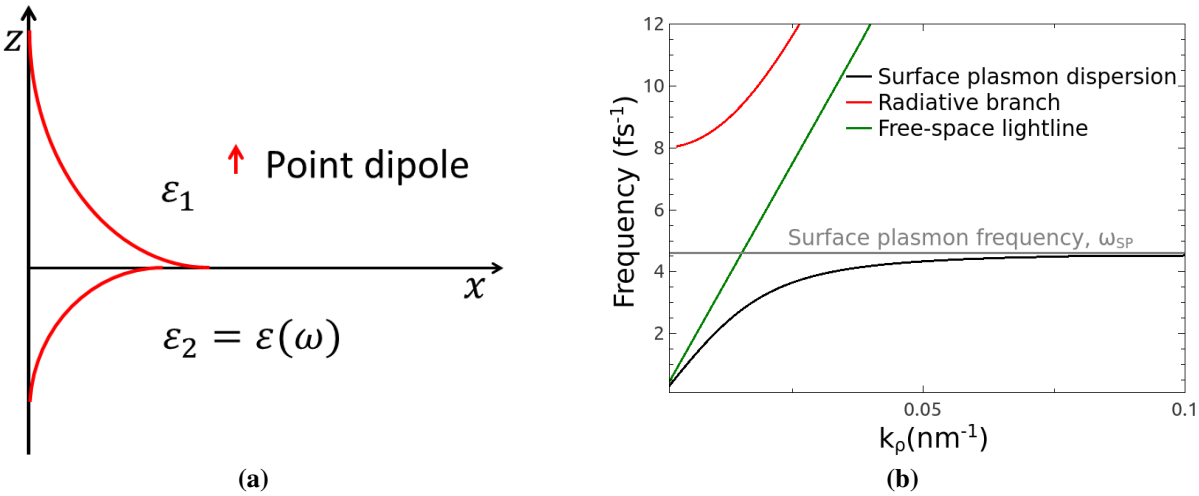

Figure 3.1: *(a) Infinite half space geometry between a dielectric, $\varepsilon_1 = 2$, and a frequency dependent Drude type of metal, $\varepsilon_2(\omega)$. The solid red lines show the field distribution of the electric field. (b) Band structure for the half space geometry shown in (a).*

lated by switching to polar coordinates, $\mathbf{k}_\rho = (k_\rho, k_\theta)$, where the k_θ integral can be performed analytically. The reflection coefficients R do not depend on k_θ. The form of the z component of the scattering part of the Green's tensor is presented in the case of a quantum emitter with the transition dipole moment oriented along z and the emitter and target points are in medium 1,

$$\mathfrak{G}^{11}_{zz}(\mathbf{r},\mathbf{s},\omega) = \frac{i}{4\pi}\int_0^\infty \mathrm{d}k_\rho \frac{k_\rho^3}{k_{z1}k_1^2} R_N^{+(11)-} J_0(k_\rho\,|\rho-\rho_s|) e^{ik_{z1}(z+z_s)}, \tag{3.17}$$

where J_0 is the regular Bessel function of zero order and $\mathbf{r} = (\rho, z)$ and $\mathbf{s} = (\rho_s, z_s)$. This integral is calculated with numerical methods. In the following paragraphs the zz-component of the transition dipole moment of the quantum emitters and the SE and ET rates are calculated. The quantum emitters considered in this chapter have emission and absorption spectra described by Dirac delta distributions .

3.3.1.1 Spontaneous emission rate

In Fig. 3.2 a quantum emitter embedded in the dielectric medium 1 is considered, with $\varepsilon_1 = 2$, at different distances, $\mathbf{r}_{\mathrm{QE}} = (0,0,z)$, from the frequency dependent medium 2, $\varepsilon_2(\omega)$. The emission frequency of the quantum emitter is varied. The SE rate is given by Eq. (2.28) and the scattering part of the Green's tensor is given by Eq. (3.17). The normalized SE rate is given by

$$\tilde{\gamma}(\omega) = \frac{\gamma}{\gamma_0} = \sqrt{\varepsilon_1} + \frac{3c}{2\omega}\mathrm{Im}\left(i\int_0^\infty \mathrm{d}k_\rho \frac{k_\rho^3}{k_{z1}k_1^2} R_N^{+(11)-} e^{2ik_{z1}z} \right). \tag{3.18}$$

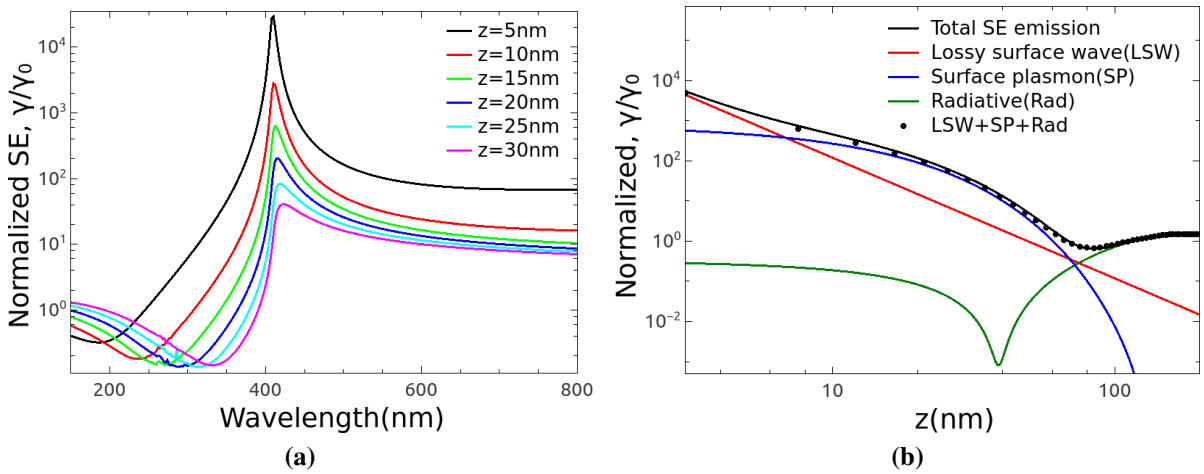

Figure 3.2: *Normalized SE rate of a QE embedded in a dielectric medium, $\varepsilon_1 = 2$, placed above a frequency dependent Drude-type metal, $\varepsilon_2(\omega)$. (a) Varying the emission wavelength of the QE, λ, for different distances away from the metal. (b) Distance dependence of the SE rate for a QE with emission $\lambda = 430\,nm$ where the lossy surface wave (LSW), surface plasmon (SP) and radiative (Rad) emission contributions are depicted.*

As can be observed in Fig. 3.2a when we are close to the SP resonance condition the SE rate is enhanced several orders of magnitude, compared with its free space value. The SP wavelength is $\lambda_{SP} = 408\,\text{nm}$ when $\text{Re}(\varepsilon_2(\omega)) = -\varepsilon_1$. As the distance between the QE and the Drude metal half space is increased the SE rate drops and at distances larger than the emission wavelength, $z \gg \lambda$, it drops to its free space value. This effect is due to the fact that the SP branch, Fig. 3.1b, lies below the light-line and we need large values of the in plane wavevector k_ρ to excite the SP modes. The near field of the QE provides these high values of k_ρ, but as the distance of the QE to the metal half space is increased, the near field of the QE drops rapidly. It is well known that by placing a dipole source at infinity its signal is received as a plane wave. Furthermore, for wavelengths smaller than the λ_{SP} the SE is suppressed, compared to the free space emission, due to the fact that these wavelengths lie in the stop-gap region and there are no modes to be excited by the QE. For larger values of the emission wavelength, $\lambda > \lambda_{SP}$, the QE can couple with the SP branch and a considerable enhancement of the SE rate is observed.

In Fig. 3.2b the distance dependence of a QE away from the Drude half space is investigated, for an emission wavelength close to SP wavelength, $\lambda = 430\,\text{nm}$. Three different contributions are presented, namely:

- At small separations of the QE-Drude media the lossy surface waves (LSW) dominate. These modes are non-radiative in nature and non-propagating. They are excited by very large wavevectors, thus, we need to be well within the near field of the QE. We can get an analytical expression for describing these modes by setting $k_\rho \to \infty$, then $k_{z1} = ik_\rho$.

The integral in Eq. (3.18) can be analytically calculated

$$\tilde{\gamma}_{\mathrm{LSW}} = \frac{\gamma_{\mathrm{LSW}}}{\gamma_0} = \frac{3}{8}\frac{1}{(k_0 z)^3}\mathrm{Im}\left(\frac{\varepsilon_2(\omega)-\varepsilon_1}{\varepsilon_2(\omega)+\varepsilon_1}\right). \tag{3.19}$$

The $\tilde{\gamma}_{\mathrm{LSW}}$ falls off rapidly as $1/z^3$ and, thus, is the main path of relaxation for the QE when it is very close to the Drude metal half space.

- The excitation of SP modes along the metal-dielectric interface. These modes appear as the pole contribution to the reflection coefficient, R_N^{+11-}, in the integral of Eq. (3.18) and we get the expression

$$\tilde{\gamma}_{\mathrm{SP}} = \frac{\gamma_{\mathrm{SP}}}{\gamma_0} = -\frac{3\pi k_0^3}{\varepsilon_1}\mathrm{Im}\left(\frac{k_{z1}^{\mathrm{SP}}}{k_{\mathrm{SP}}^6}(\varepsilon_2(\omega)-\varepsilon_1)e^{2ik_{z1}^{\mathrm{SP}}z}\right), \tag{3.20}$$

where the SP wavenumber, k_{SP}, is given by Eq. (3.15), and was shown in Fig. 3.1b as the SP dispersion, and $k_{z1}^{\mathrm{SP}} = \sqrt{k_1^2 - k_{\mathrm{SP}}^2}$. For wavelengths above the SP wavelength the k_{z1}^{SP} has a complex component, thus, the exponent in Eq. (3.20) drops as the separation between the QE-metal is increased.

- Finally, by integrating the integral of Eq. (3.18) in the $(0, k_1)$ interval we get the radiation of the QE to the far field. For these modes the k_{z1} is real. The contribution of these modes to the total SE is given by:

$$\tilde{\gamma}_{\mathrm{Rad}} = \frac{\gamma_{\mathrm{Rad}}}{\gamma_0} = \sqrt{\varepsilon_1} + \frac{3c}{2\omega}\mathrm{Im}\left(i\int_0^{k_1} \mathrm{d}k_\rho \frac{k_\rho^3}{k_{z1}k_1^2}R_N^{+(11)-}e^{2ik_{z1}z}\right). \tag{3.21}$$

Thus, the normalized total SE rate of the QE has the form

$$\tilde{\gamma}_{\mathrm{Total}} = \tilde{\gamma}_{\mathrm{Rad}} + \tilde{\gamma}_{\mathrm{SP}} + \tilde{\gamma}_{\mathrm{LSW}}. \tag{3.22}$$

where the different contributions are given by Eq. (3.19-3.21) for a QE whose transition dipole moment is along z. In Fig. 3.2b the full numerical integration of Eq. (3.18) is presented and the various contributions extracted earlier. Very close to the metal there is a considerable contribution to the SE rate from the SP mode but the main path of relaxation is through the LSW, which drops rapidly as this distance is increased. At the intermediate distances between 5 nm to 60 nm the SP modes are the main path of relaxation. Up to these distances the far field emission is suppressed and is below the free space values. At distances above 100 nm the QE

is only emitting in the far field.

3.3.1.2 Energy transfer rate

In Fig. 3.3 a contour plot of the logarithm of ET rate, $\Gamma(\mathbf{r},\mathbf{s},\omega) \propto |\mathfrak{G}(\mathbf{r},\mathbf{s},\omega)|^2$ is presented, with the Green's tensor given by Eq. (3.2). The position of the donor QE is kept fixed, $\mathbf{r}_\mathrm{D} = (0,0,z_\mathrm{D})$, and we scan the xz-plane varying the acceptor QE position, $\mathbf{r}_\mathrm{A} = (x,0,z)$. The emission wavelength of the donor QE is close to the SP wavelength, $\lambda = 430\,\mathrm{nm}$. The zz-transition dipole moments of the donor and acceptor QEs are considered. Three different positions of the donor QE above the Drude metal half space are investigated, $z_\mathrm{D} = 5\,\mathrm{nm},\ 10\,\mathrm{nm}$ and $15\,\mathrm{nm}$, in Fig. (3.3a-3.3c) respectively. As the separation between the donor QE and the metal surface is increased, the ET rate drops, since the coupling with the near field of the donor QE drops. Moreover, the ET rate has its largest values very close to the metal-dielectric interface. The closer the donor QE is to the metal, the larger is the field extent along the interface. This shows the importance of exciting the SP modes in order to enhance the interaction distance and, also that the donor-acceptor position plays a crucial role. As we increase the acceptor position away from the interface the ET rate falls off rapidly, due to the tight confinement of the field at the metal-dielectric interface.

3.3.2 Metallic slab geometry between dielectric substrates

In this subsection the focus is on the geometry presented in Fig. 3.4 comprised of three different materials. The material labeled with 1 has a dielectric permittivity $\varepsilon_1 = 2$, material 2 is described by the frequency dependent Drude dielectric permittivity given by Eq. (3.5), and finally material 3 has $\varepsilon_3 = 4$. The metallic slab has a thickness d and its center is placed at the $z = 0$ plane. Eq. (3.5) is used with $\omega_p = 8\,\mathrm{fs}^{-1}$ and $\gamma = 0.07\,\mathrm{fs}^{-1}$, the same parameters as have been used for the single interface geometry. The focus here is on the case where the donor QE is placed in medium 1, cf. Fig. 3.4.

The construction of the scattering part of the Green's tensor is described following the same method as in Sub. 3.3.1. After applying the boundary conditions, Eq. (3.3), at the $z = \pm d/2$ we end up with a system of equations described by Eq. (3.8) where now the characteristic

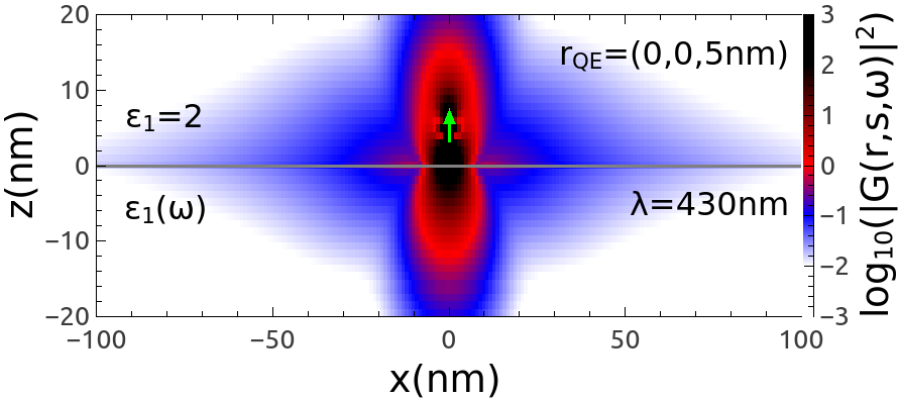

(a)

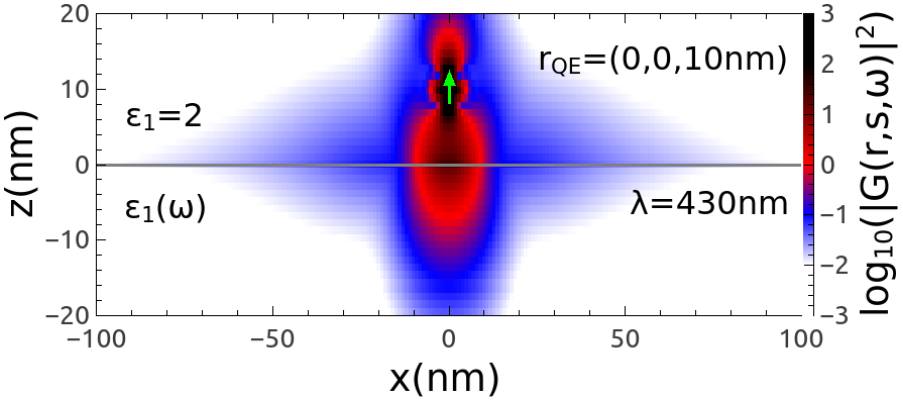

(b)

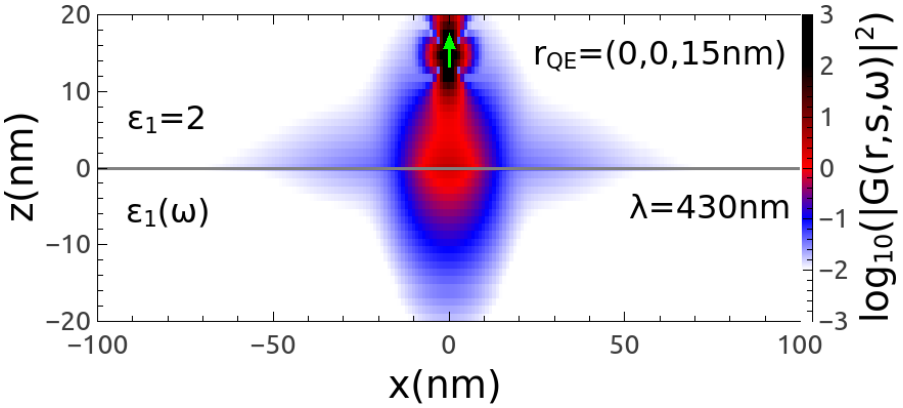

(c)

Figure 3.3: *Contour plot of the ET rate for fixed donor position,* $\mathbf{r}_D = (0,0,z_D)$*, and varying acceptor position,* $\mathbf{r} = (x_A,0,z_A)$*, in the xz-plane. The z-orientation of the transition dipole moment of the donor and acceptor QEs is considered. The emission wavelength of the donor QE is* $\lambda_D = 430\,nm$*. Three positions for the donor QE (a)* $z_D = 5\,nm$*, (b)* $z_D = 10\,nm$ *and (c)* $z_D = 15\,nm$ *are considered.*

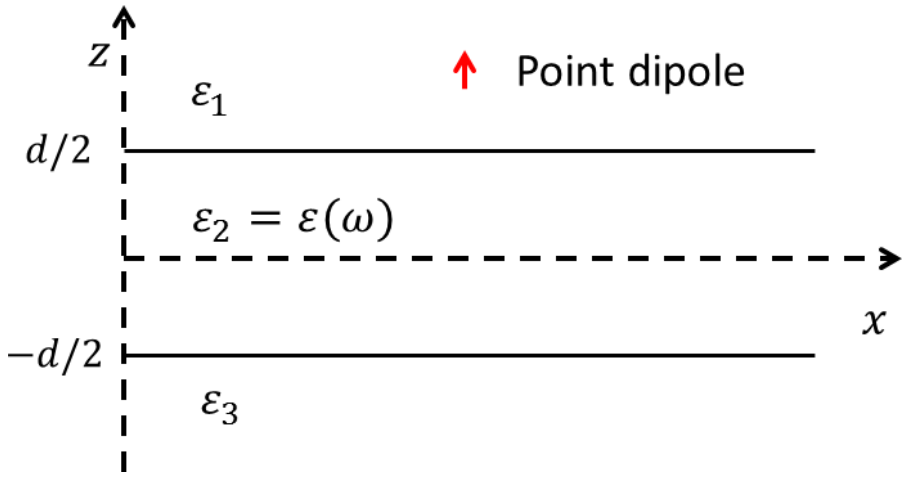

Figure 3.4: *Drude metal slab geometry with dielectric permittivities of* $\varepsilon_1 = 2, \varepsilon_2(\omega), \varepsilon_3 = 4$ *. We focus on the case where the QE is placed in medium 1,* $\varepsilon_1 = 2$*, for the SE and ET rates.*

matrices describing the TE and TM polarizations are given by:

$$\Delta_M = \begin{pmatrix} e^{i/2k_{z1}d} & -e^{i/2k_{z2}d} & -e^{-i/2k_{z2}d} & 0 \\ k_{z1}e^{i/2k_{z1}d} & -k_{z2}e^{i/2k_{z2}d} & k_{z2}e^{-i/2k_{z2}d} & 0 \\ 0 & e^{-i/2k_{z2}d} & e^{i/2k_{z2}d} & -e^{i/2k_{z3}d} \\ 0 & k_{z2}e^{-i/2k_{z2}d} & -k_{z2}e^{i/2k_{z2}d} & -k_{z1}e^{i/2k_{z3}d} \end{pmatrix}, \tag{3.23}$$

$$\Delta_N = \begin{pmatrix} \frac{k_{z1}}{k_1}e^{i/2k_{z1}d} & -\frac{k_{z2}}{k_2}e^{i/2k_{z2}d} & \frac{k_{z2}}{k_2}e^{-i/2k_{z2}d} & 0 \\ k_1e^{i/2k_{z1}d} & -k_2e^{i/2k_{z2}d} & k_2e^{-i/2k_{z2}d} & 0 \\ 0 & \frac{k_{z2}}{k_2}e^{-i/2k_{z2}d} & -\frac{k_{z2}}{k_2}e^{i/2k_{z2}d} & \frac{k_{z3}}{k_3}e^{i/2k_{z3}d} \\ 0 & k_2e^{-i/2k_{z2}d} & k_2e^{i/2k_{z2}d} & -k_1e^{i/2k_{z3}d} \end{pmatrix}, \tag{3.24}$$

the generalized unknown coefficients have the form:

$$\mathbf{R}_M^{11} = \begin{pmatrix} R_M^{+(11)-} \\ R_M^{+(21)-} \\ R_M^{-(21)-} \\ R_M^{-(31)-} \end{pmatrix}, \quad \mathbf{R}_N^{11} = \begin{pmatrix} R_N^{+(11)-} \\ R_N^{+(21)-} \\ R_N^{-(21)-} \\ R_N^{-(31)-} \end{pmatrix}, \tag{3.25}$$

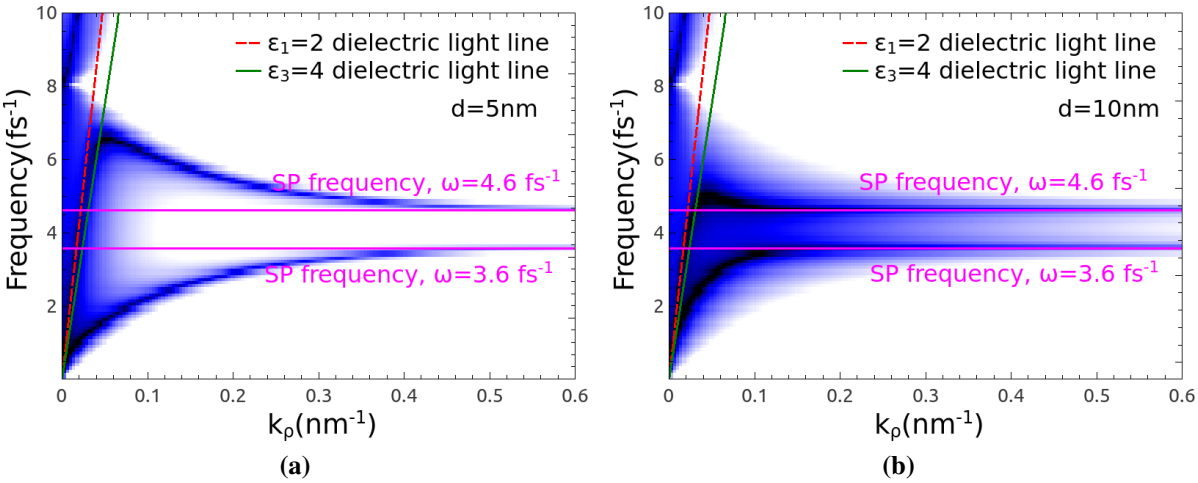

Figure 3.5: *Band structure of the slab geometry. Contour plot of* $1/Det(\Delta_N)$ *as a function of frequency,* ω*, and the in plane wavevector,* k_ρ*, for two slab thicknesses (a)* $d = 5\,nm$ *and (b)* $d = 10\,nm$*.*

and the free-terms vectors are given by:

$$\mathbf{V}_M^{11} = \begin{pmatrix} -e^{-i/2k_{z1}d} \\ -k_{z1}e^{-i/2k_{z1}d} \\ 0 \\ 0 \end{pmatrix}, \quad \mathbf{V}_N^{11} = \begin{pmatrix} \frac{k_{z1}}{k_1}e^{-i/2k_{z1}d} \\ k_1 e^{-i/2k_{z1}d} \\ 0 \\ 0 \end{pmatrix}. \tag{3.26}$$

With the above method, the generalized reflection coefficients, R, are calculated, which fully characterize the problem under consideration. Before doing that, the modes provided by the slab geometry are discussed. In Fig. 3.5 a contour plot of the expression $1/\mathrm{Det}(\Delta_N(\omega, k_\rho))$ is presented, as a function of the frequency, ω, and the in-plane wavevector, k_ρ. The dark colors in Fig. 3.5 are connected with large values of this expression, which, in turn, are connected with the poles of the expression $1/\mathrm{Det}(\Delta_N)$. This provides all the available modes supported by the slab geometry, in particular the dispersion relation [16, 144]. Two thicknesses for the slab, $d = 5\,$nm, Fig. 3.5a, and $d = 10\,$nm, Fig. 3.5b are considered. Firstly, in both figures is observed that two SP branches are present due to the fact that two dielectric-metal interfaces are included. Also, for higher values of the in-plane wavevector, k_ρ, the two branches asymptotically tend to the SP frequencies given by the expression $\omega_{\mathrm{SP}i} = \omega_p/\sqrt{\varepsilon_i + 1}$, where for our case $i = 1, 3$. The SP frequencies have the values $\omega_{\mathrm{SP1}} = 4.6\,\mathrm{fs}^{-1}$, ($\lambda_{\mathrm{SP1}} = 430\,$nm), and $\omega_{\mathrm{SP3}} = 3.6\,\mathrm{fs}^{-1}$($\lambda_{\mathrm{SP3}} = 524\,$nm). In Fig. 3.5a, where the slab thickness is $d = 5\,$nm, the upper SP branch lies in the stop gap, a region which for the half space geometry was inaccessible. As the thickness of the metallic slab is increased, Fig. 3.5b, the upper SP branch lies also below

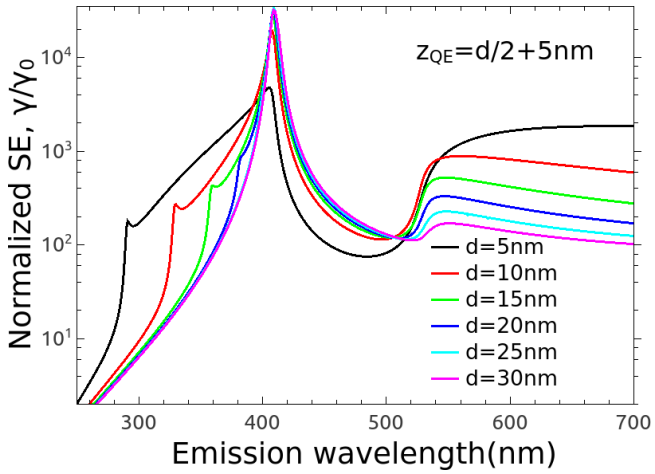

Figure 3.6: *Normalized SE of a QE above a metallic slab, embedded in $\varepsilon_1 = 2$, for different thicknesses of the metallic slab, d, as a function of the emission wavelength of the QE. The position of the quantum emitter is given by $z_{QE} = d/2 + 5\,nm$.*

the asymptotically value of ω_{SP1}. Moreover, a main difference between the single interface and the slab geometries, regarding their dispersion relation is that, for the smaller thickness of the slab, Fig. 3.5a, it tends to the SP frequencies at large values of the wavevector k_ρ, while as we increase the thickness, smaller values are required. For comparison, for the $d = 5\,nm$ thickness they tend to the asymptotic values for wavevectors $k_\rho = 0.4\,nm^{-1}$ while for the half space geometry the dispersion branch tends to the asymptotic value at $k_\rho = 0.1\,nm^{-1}$.

In the following, the SE of a single QE, and the ET between a pair of QEs, are discussed for a transition dipole moment along the z-axis. The scattering part of the Green's tensor, for the case that the QE and the target position are in medium 1 is given by expression Eq. (3.17).

3.3.2.1 Spontaneous emission rate

In this subsection the normalized spontaneous emission rate, $\tilde{\gamma}$, of a QE is studied, for a dipole moment oriented along the z-axis and placed above a metallic slab of thickness d, embedded the medium 1, $\varepsilon_1 = 2$. In Fig. 3.6 the normalized SE rate is presented as a function of the emission wavelength, λ, for different thicknesses of the metallic slab. Fig. 3.6 shows that there are two resonance wavelengths, as is expected from the dispersion relation Fig. 3.5, at $\lambda_{SP1} = 430\,nm$ and $\lambda_{SP2} = 524\,nm$. Close to λ_{SP1}, for all the slab thicknesses d, the SE rate has values up to 10^5 due to the excitation of the SP mode. For the surface plasmon λ_{SP2}, which is the SP wavelength connected with the lower metal-dielectric interface, $\varepsilon_2(\omega)/\varepsilon_3$, the normalized SE rate has a peak that is more broad compared with the case λ_{SP1}. Furthermore, as the slab thickness is increased, the coupling of the near field of the QE with the opposite

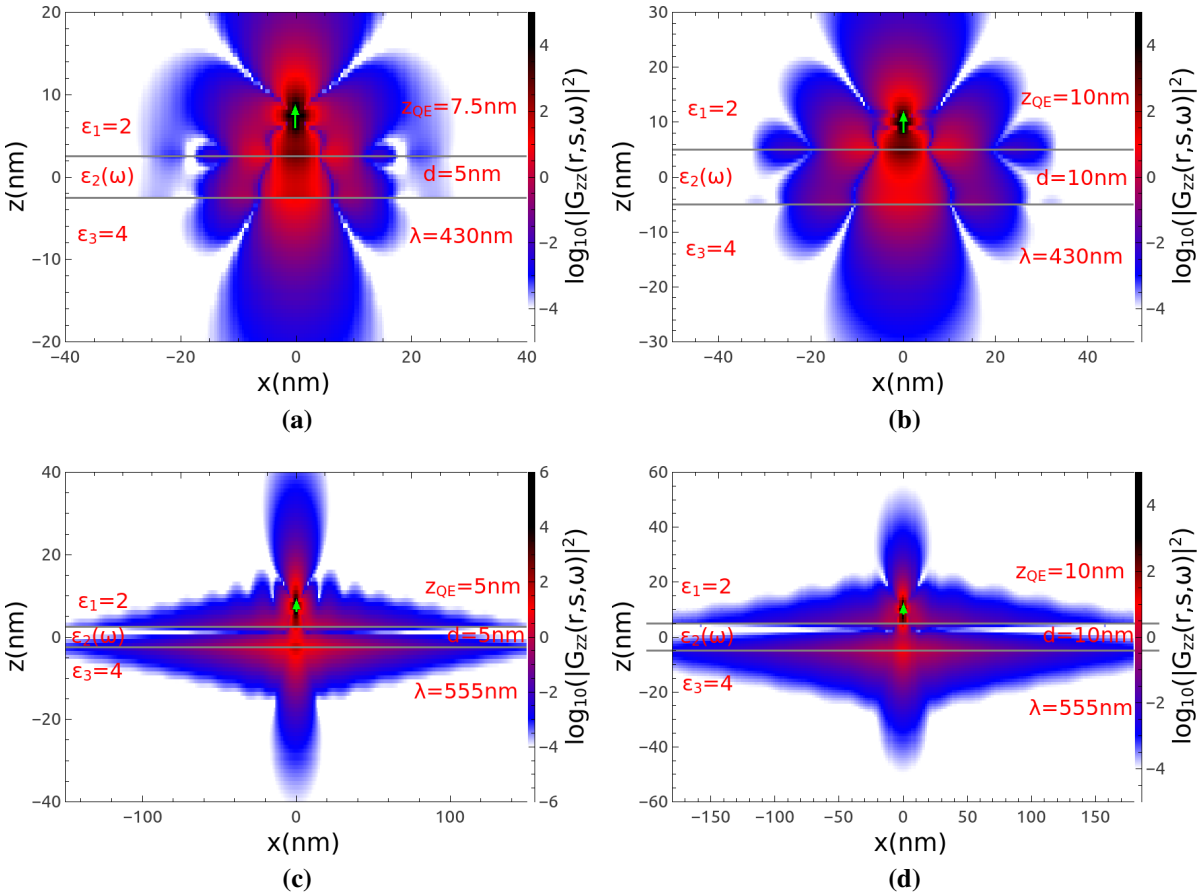

Figure 3.7: *Contour plot of the ET rate for fixed donor position,* $\mathbf{r}_D = (0,0,5\,nm + d/2)$*, as a function of the acceptor position,* $\mathbf{r} = (x_A, 0, z_A)$*, in the* $xz-$*plane. We consider the* $zz-$*orientation for the transition dipole moment for the donor and acceptor QEs. The emission wavelength of the donor QE is (a-b)* $\lambda_D = 430\,nm$ *and (c-d)* $\lambda_D = 555\,nm$*. Two thickness for the metallic slab are considered, (a,c)* $d = 5\,nm$ *and (b,d)* $d = 10\,nm$*.*

surface is smaller, hence the normalized SE rate is decreased.

The shoulder observed in Fig. 3.6 for the thickness of 5 nm at around 290 nm is attributed to the intersection of the upper branch of the SP mode with the light line, see Fig. 3.5a. As the thickness of the slab is increased this shoulder is redshifted, because the intersection of the upper SP branch with the light line is also redshifted. Compare Fig. 3.5a and 3.5b. For larger thicknesses this shoulder disappears, $d = 30$ nm.

3.3.2.2 Energy transfer rate

In this subsection the ET rate, Γ, between two QEs is investigated, when their dipole moments are along the z-axis, near a metallic slab. Two thicknesses, $d = 5\,\text{nm}$ and $d = 10\,\text{nm}$, of the Drude metal slab are investigated. In Fig. 3.7 a contour plot of the xz cross section of the

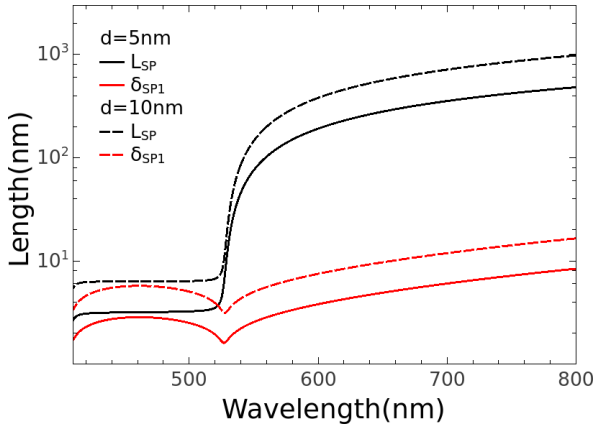

Figure 3.8: *Propagation length, L_{SP} , and penetration depth in medium 1, δ_{SP1}, of a metallic slab for different slab thicknesses.*

ET rate $\Gamma(\mathbf{r},\mathbf{s},\omega) \propto |\mathfrak{G}(\mathbf{r},\mathbf{s},\lambda)|^2$ is presented for donor emission wavelengths of $\lambda = 430\,\text{nm}$ and $\lambda = 555\,\text{nm}$. These wavelengths are close to the SP wavelengths but the wavelength $\lambda = 430\,\text{nm}$ lies in the band gap between the two surface plasmon wavelengths, see Fig. 3.5. The color map scale is the same in all graphs, thus the color differences can directly be connected with the ET rate strength. When the ET rate investigated for the case of the half space geometry, Fig. 3.3, as the donor QE -metal surface separation increased the interaction strength decreased, thus the donor QE is placed 5 nm above the metal slab in all cases considered for the rest of this section.

In Fig. 3.7a and 3.7b, the donor emission wavelength is $\lambda = 430\,\text{nm}$, for metal thicknesses $d = 5\,\text{nm}$ and 10 nm, respectively. This wavelength lies in the region between the two SP modes, see Fig. 3.5, in that region the upper branch of the SP mode is very close to the light line, thus the coupling with the propagating SP modes is poor. The ET rate has large values when the acceptor QE is close to the donor QE and has a similar spatial distribution in the xz-plane as for the free space case, with a minimum coupling with the slab geometry. On the other hand, in Fig. 3.7c and 3.7d, the donor emission wavelength is $\lambda = 555\,\text{nm}$, a large influence in the ET, between the donor and acceptor QEs, is observed from the slab geometry due to the coupling with the propagating SP modes. The lobes observed in Fig. 3.7c and 3.7d, when placing the donor QE close to the metal/dielectric interfaces, are connected with the surface plasmon wavelength, $\lambda_{\text{SP}} = 2\pi/k_{\text{SP}}$. In particular, for the $d = 5$ nm we have $\lambda_{\text{SP}} = 20$ nm and for $d = 10$ nm is $\lambda_{\text{SP}} = 60$ nm. The surface plasmon wavevector, k_{SP}, is extracted from the SP dispersion, see Fig. 3.5.

In Fig. 3.8 the propagation length, $L_{SP} = 1/\text{Im}(k_s^{\text{SP}})$ and the penetration depth, $\delta_{SP1} = 1/\text{Im}(k_{z1}^{\text{SP}})$, are plotted for the two thicknesses discussed in Fig. 3.7. In the the region be-

tween the two surface plasmon modes the propagation length is quenched, thus explaining the behavior observed in Fig. 3.7a and 3.7b. Considering the case that the emission wavelength of the donor QE is $\lambda = 555\,\text{nm}$ for the thicknesses $d = 5\,\text{nm}$, Fig. 3.7c, and $d = 10\,\text{nm}$, Fig. 3.7d, the propagation lengths are 90 nm and 145 nm, respectively. This explains why the interaction distance between the donor-acceptor QEs is increased compared with the case where the donor emission wavelength is $\lambda = 430\,\text{nm}$. Furthermore, in Fig. 3.8 the penetration depth, $\delta_{SP1} = 1/\text{Im}(k_{z1}^{\text{SP}})$, is smaller in the region between the two SP wavelengths thus for $\lambda = 430\,\text{nm}$ in Fig. 3.7 the extent of the ET is smaller compared with the $\lambda = 555$ nm.

3.4 Summary and conclusions

In the beginning of this chapter the method of scattering superposition was introduced for multilayer planar structures in order to calculate the Green's tensor. This method was applied in Sec. 3.3 for calculating the Green's tensor for a single interface and slab geometries. The method of scattering superposition will be applied in Chapter 4, for a dielectric coated cylinder, and in Chapter 5, for a graphene monolayer.

The knowledge of the Green's tensor is needed for investigating the SE and ET rates for a single interface and slab geometries. The SE rate of a quantum emitter is enhanced several orders of magnitude, compared with its free space value, due to the excitation of the SP modes. The spectral and distance dependence of a QE interacting with the planar geometries is investigated and explained with the help of the dispersion relation. The ET rate is observed to have large values when the donor and acceptor quantum emitters are close to the dielectric-metal interface, and when the near field of the donor can efficiently excite the surface plasmon mode. The form of the interaction is explained by the properties of the SP mode, its penetration depth, its propagation length and its plasmon wavevector.

This Chapter is used as a pedagogical introduction to the interaction between QEs and conducting planar multilayer nanostructures. In the next chapter a dielectric coated metallic cylinder is considered for enhancing the interaction distance between quantum emitters through the SP mode provided by the metallic core.

Chapter 4

Spontaneous Emission and Energy Transfer Rates Near a Coated Metallic Cylinder

4.1 Introduction

In this chapter the spontaneous emission (SE) rate of a single quantum emitter (QE), and energy transfer (ET) rate between a pair of QEs, are investigated in the presence of a dielectrically coated metallic infinite cylinder as a function of the material and dimensions of the core and coating, as well as the emission wavelength of the donor. For the material of the core we consider gold and silver, whose surface plasmon wavelengths lie in the visible part of the electromagnetic spectrum. Tabulated experimental data are used to describe the optical response of these materials [129]. The SE and ET rates are calculated using a semi-analytical Green's tensor method [141, 142]. A variety of quantum systems can be investigated this way, e.g. atoms, molecules, quantum dots and fluorescent dyes.

The SE and ET rates have been studied extensively for cylindrical geometries during the past decade, the focus being mainly on the SE rate in the presence of dielectric and metallic cylinders. Furthermore, it has been shown that the ET rate between a pair of quantum emitters can be significantly enhanced due to coupling to SP modes on a metallic cylinder [37, 40].

When a dielectric coating to a metallic core is considered, it can support SP modes [32]. Moreover, it is found that the spontaneous emission rate is enhanced by several orders of magnitude when the emission wavelength is close to the surface plasmon wavelength. The energy transfer rate enhancement is found to be concentrated in hot spots around the circumference of the coated cylinder. Introducing the energy transfer efficiency as a parameter, it is found that, when the donor emission and acceptor absorption spectra are resonant with the SP modes excited on the coated cylinder, the energy transfer efficiency can be significantly enhanced

compared to the off-resonance situation. Tuning the SP wavelength to the emission wavelength of the donor via the geometrical and material parameters of the coated cylinder allows control of the energy transfer efficiency.

Top-down techniques, e.g. electron-beam lithography, or bottom-up techniques, e.g. colloidal synthesis, can be used to fabricate hybrid nanostructures with dimensions of a few tens of nanometers. These structures form the building blocks for a variety of potential technological applications. Nanowires and coated nanowire structures can be used in light harvesting [146,147] and switching devices [148], imaging [149,150], light conversion [150,151] and quantum optics applications [50]. A good understanding of the SE and ET processes in these environments is important for manipulation of light below the diffraction limit.

The chapter is structured as follows: In Sec. 4.2 an outline of the formalism used is presented, while in Sec. 4.3 the results of our simulations of the SE and ET rates for various material and dimensions of the dielectric coated cylinder are presented and discussed. Finally, Sec. 4.4 is reserved for a summary of the results and the conclusions that can be drawn.

4.2 Spontaneous emission, energy transfer and the Green's tensor formalism

The Green's tensor encapsulates all the information for the response of material bodies to electromagnetic fields and determines the normalized SE rate, Eq. (2.28), and normalized ET function, Eq. (2.35). In what follows a method for calculating the Green's tensor for a coated cylinder geometry is presented [152].

A coated cylinder with core radius, a, and outer radius, b, is considered, embedded in a homogeneous medium with dielectric permittivity ε_3, as in Fig. 4.1. The cylinder axis is along the z-direction. The dielectric permittivity of the core cylinder is ε_1 which is taken from the tabulated experimental data of Ref. [129], see Fig. 1.3a, while the coating will have a constant dielectric permittivity ε_2. Due to the cylindrical symmetry of the structure, throughout this chapter the cylindrical coordinate system, (ρ,θ,z), is used.

In order to calculate the Green's tensor for the coated cylinder geometry the method of scattering superposition is used [141,142] which was introduced in Sec. 3.2 for planar geometries. When the source point is located in the background medium outside the coated cylinder, the Green's tensor has the form

$$\mathfrak{G}^{(13)}(\mathbf{r},\mathbf{s},\omega) = \mathfrak{G}_s^{(13)}(\mathbf{r},\mathbf{s},\omega), \tag{4.1}$$

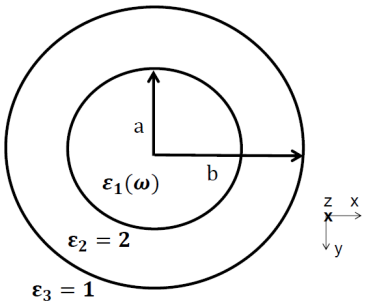

Figure 4.1: *Cross-section of an infinitely long coated cylinder, with its axis along the z-direction, core radius a and outer radius b. The dielectric permittivity of the core is ε_1, the dielectric permittivity of the coating is ε_2 and that of the surrounding medium is ε_3.*

$$\mathfrak{G}^{(23)}(\mathbf{r},\mathbf{s},\omega) = \mathfrak{G}_s^{(23)}(\mathbf{r},\mathbf{s},\omega), \tag{4.2}$$

$$\mathfrak{G}^{(33)}(\mathbf{r},\mathbf{s},\omega) = \mathfrak{G}_h^{(33)}(\mathbf{r},\mathbf{s},\omega) + \mathfrak{G}_s^{(33)}(\mathbf{r},\mathbf{s},\omega), \tag{4.3}$$

where the first of the two labels in the superscript $(i3)$, $i = 1,2,3$, denotes the field point, while the second denotes the source point. The subscript s denotes the scattering term, always present, while the homogeneous term $\mathfrak{G}_h^{(33)}(\mathbf{r},\mathbf{s},\omega)$ contributes only when the source and field points are in the same medium. When calculating the ET rate, the source and field points correspond to the donor and acceptor positions, respectively, while for the SE rate, the source and field points coincide and correspond to the position of the quantum emitter.

The scattering term has the following general expression, see Sec. 2.5.2 and Eq. (2.53),

$$\mathfrak{G}_s^{(i3)}(\mathbf{r},\mathbf{s},\omega) = \frac{i}{8\pi}\sum_{n,K}\int_{-\infty}^{\infty} \mathrm{d}k_z \left[R_{MK}^{i3}\mathbf{M}_n(k_{\rho i},\mathbf{r}) + R_{NK}^{i3}\mathbf{N}_n(k_{\rho i},\mathbf{r})\right] \otimes \mathbf{K}_n^{(1)}(k_{\rho 3},\mathbf{s}), \tag{4.4}$$

where $k_{\rho i} = \sqrt{k_i^2 - k_z^2}$ is the radial propagation constant in medium i, and $k_i = \frac{\omega}{c}\sqrt{\varepsilon_i}$ is the wavenumber in medium i ($i = 1,2,3$). The above expression involves a summation over $\mathbf{K}$ which represents $\mathbf{M}_n^{(1)}(k_{\rho 3})$ and $\mathbf{N}_n^{(1)}(k_{\rho 3})$, or the transverse electric (TE) and transverse magnetic (TM) modes. As is evident, the field has a hybrid nature, and cannot be separated into TE and TM modes. The vector wave functions are solutions of the Helmholtz equation in cylindrical coordinates and involve Bessel and Hankel functions. The superscript (1) in $\mathbf{M}_n^{(1)}(k_\rho)$ denotes the fact that we use the Hankel function of the first kind. This form of the Green's tensor already takes into account the radiation condition at infinity and the regularity condition on the z axis, i.e. at $\rho = 0$, where the regular Bessel functions are used.

The following continuity conditions are imposed at the surface of the core ($\rho_1 = a$) and

coating ($\rho_2 = b$),

$$\hat{\rho} \times \left[\mathfrak{G}^{(i3)}(\mathbf{r},\mathbf{s},\omega) - \mathfrak{G}^{((i+1)3)}(\mathbf{r},\mathbf{s},\omega) \right] \Big|_{\rho=\rho_i} = 0, \tag{4.5}$$

$$\hat{\rho} \times \left[\nabla \times \mathfrak{G}^{(i3)}(\mathbf{r},\mathbf{s},\omega) - \nabla \times \mathfrak{G}^{((i+1)3)}(\mathbf{r},\mathbf{s},\omega) \right] \Big|_{\rho=\rho_i} = 0. \tag{4.6}$$

Using equation (4.2) in the continuity conditions, two inhomogeneous systems of linear equations are obtained, one for each polarization **M** or **N**. This system of equations can be written in matrix form as

$$\Delta(n,k_z) \cdot \mathbf{R}_{M(N)}(n,k_z) = \mathbf{V}_{M(N)}(n,k_z), \tag{4.7}$$

where $\Delta(n,k_z)$ represents the characteristic matrix, the same for both polarizations TE and TM, $\mathbf{R}_M(n,k_z)$ and $\mathbf{R}_N(n,k_z)$ are the unknown coefficients vectors, and $\mathbf{V}_M(n,k_z)$ and $\mathbf{V}_N(n,k_z)$ are the free-term vectors, known quantities emerging from the homogeneous part of the Green's tensor $\mathfrak{G}^{(33)}(\mathbf{r},\mathbf{s},\omega)$, and associated with the field of a point dipole source.

The characteristic matrix, $\Delta(n,k_z)$, has the form:

$$\Delta_n = \tag{4.8}$$

$$\begin{pmatrix}
k_{\rho 1}J'_{n1a} & \frac{nk_z}{ak_1}J_{n1a} & -k_{\rho 2}H'^{(1)}_{n2a} & -\frac{nk_z}{ak_2}H^{(1)}_{n2a} & -k_{\rho 2}J'_{n2a} & -\frac{nk_z}{ak_2}J_{n2a} & 0 & 0 \\
0 & \frac{k_{\rho 1}^2}{k_1}J_{n1a} & 0 & -\frac{k_{\rho 2}^2}{k_2}H^{(1)}_{n2a} & 0 & -\frac{k_{\rho 2}^2}{k_2}J_{n2a} & 0 & 0 \\
\frac{nk_z}{a}J_{n1a} & k_1k_{\rho 1}J'_{n1a} & -\frac{nk_z}{a}H^{(1)}_{n2a} & -k_2k_{\rho 2}H'^{(1)}_{n2a} & -\frac{nk_z}{a}J_{n2a} & k_2k_{\rho 2}J'_{n2a} & 0 & 0 \\
k_{\rho 1}^2J_{n1a} & 0 & -k_{\rho 2}^2H^{(1)}_{n2a} & 0 & -k_{\rho 2}^2J_{n2a} & 0 & 0 & 0 \\
0 & 0 & 0 & \frac{k_{\rho 2}^2}{k_2}H^{(1)}_{n2b} & 0 & \frac{k_{\rho 2}^2}{k_2}J_{n2b} & 0 & -\frac{k_{\rho 3}^2}{k_3}H^{(1)}_{n3b} \\
0 & 0 & k_{\rho 2}H'^{(1)}_{n2b} & \frac{nk_z}{bk}H^{(1)}_{n2b} & k_{\rho 2}J'_{n2b} & \frac{nk_z}{ak_2}J_{n2b} & -k_{\rho 3}H'^{(1)}_{n3b} & -\frac{nk_z}{k_3b}H^{(1)}_{n3b} \\
0 & 0 & k_{\rho 2}^2H^{(1)}_{n2b} & 0 & k_{\rho 2}^2J_{n2b} & 0 & -k_{\rho 3}^2H^{(1)}_{n3b} & 0 \\
0 & 0 & \frac{nk_z}{b}H^{(1)}_{n2b} & k_2k_{\rho 2}H'^{(1)}_{n2b} & -\frac{nk_z}{b}J_{n2b} & k_2k_{\rho 2}J'_{n2b} & -\frac{nk_z}{b}H^{(1)}_{n3b} & -k_3k_{\rho 3}H'^{(1)}_{n3b}
\end{pmatrix},$$

where we use the compact notation $J_{n1a} = J_n(k_{\rho 1}a)$, $H^{(1)}_{n2a} = H^{(1)}_n(k_{\rho 2}a)$ and so on. The free-

term vectors, $\mathbf{V}_M^3(n,k_z)$ and $\mathbf{V}_N^3(n,k_z)$, have the form:

$$\mathbf{V}_M^3(n,k_z)=\begin{pmatrix}0\\0\\0\\0\\0\\k_{\rho 3}J_n'(k_{\rho 3}b)\\k_{\rho 3}^2J_n(k_{\rho 3}b)\\\frac{nk_z}{b}J_n(k_{\rho 3}b)\end{pmatrix},\ \mathbf{V}_N^3(n,k_z)=\begin{pmatrix}0\\0\\0\\0\\\frac{k_{\rho 3}^2}{k_3}J_n(k_{\rho 3}b)\\\frac{nk_z}{bk_3}J_n(k_{\rho 3}b)\\0\\k_3k_{\rho 3}J_n'(k_{\rho 3}b)\end{pmatrix}, \tag{4.9}$$

while the coefficients vectors are:

$$\mathbf{R}_M=\begin{pmatrix}R_{MM}^{13}\\R_{NM}^{13}\\R_{MM}^{H23}\\R_{NM}^{H23}\\R_{MM}^{J23}\\R_{NM}^{H23}\\R_{MM}^{33}\\R_{MM}^{33}\end{pmatrix},\ \mathbf{R}_N=\begin{pmatrix}R_{MN}^{13}\\R_{NN}^{13}\\R_{MN}^{H23}\\R_{NN}^{H23}\\R_{MN}^{J23}\\R_{NN}^{H23}\\R_{MN}^{33}\\R_{MN}^{33}\end{pmatrix}. \tag{4.10}$$

Using these expressions, Eq. (4.7) can be readily solved.

As an example, the expression of the scattering part of the Green's tensor is given for the case when the donor and the acceptor are both oriented along the z direction:

$$\mathfrak{G}_{s(zz)}^{(13)}(\mathbf{r},\mathbf{s},\omega)=\frac{i}{8\pi}\sum_{n=-\infty}^{\infty}\int_{-\infty}^{\infty}\mathrm{d}k_z\frac{k_{\rho 1}^2}{k_1k_3}R_{NN}^{13}\,J_n(k_{\rho 1}\rho)\,H_n(k_{\rho 3}\rho_s)\,\mathrm{e}^{in\theta}\,\mathrm{e}^{ik_zz}. \tag{4.11}$$

The integrals above do not depend on θ_s, because of the rotational symmetry, or z_s, because of translation symmetry along the axis of the cylinder. The integrals are also symmetric with respect to k_z, which means that the integration interval of k_z can be replaced with the interval $(0,\infty)$. The various scattering coefficients have a complicated form, and we implement numerical methods to calculate these integrals and thereafter the SE and ET rates. One can distinguish three contributions in the above integrals: for $k_z\in(0,k_3)$, one integrates over contributions from radiative modes traveling freely in the surrounding medium, in this case air; for

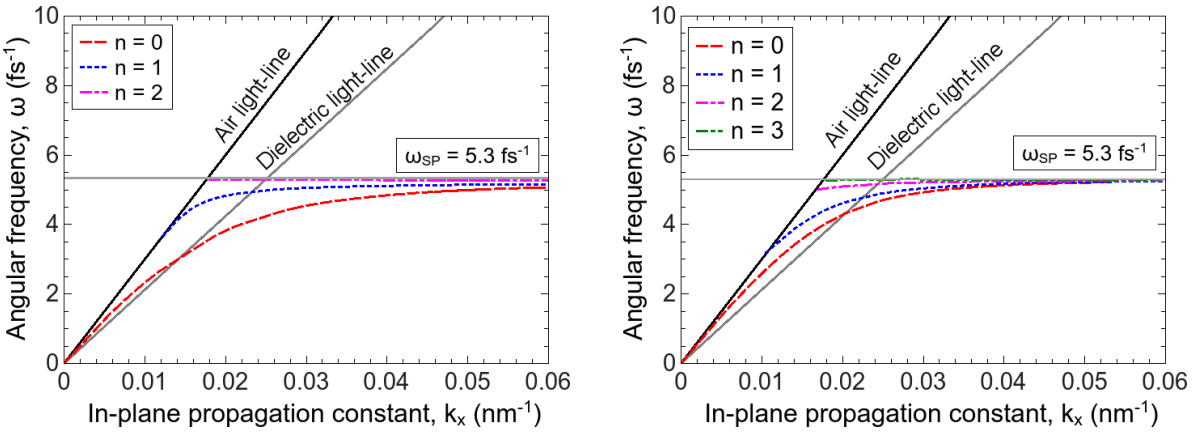

(a) $a = 40$ *nm*, $b = 50$ *nm* **(b)** $a = 80$ *nm*, $b = 90$ *nm*

Figure 4.2: *Dispersion curves of surface plasmons of different orders n on a coated cylinder with a Ag core, dielectric coating* $\varepsilon_2 = 2$ *and embedded in air, for two different sets of geometric parameters: (a)* $a = 40$ *nm and* $b = 50$ *nm (b)* $a = 80$ *nm and* $b = 90$ *nm.*

$k_z \in (k_3, k_2)$, the integral gives the contribution from guided modes within the dielectric coating. These modes are evanescent in the surrounding medium, and thus only contribute when the donor and acceptor are both close to the surface of the coating. Finally, for $k_z \in (k_2, \infty)$, the integral has contributions from surface plasmon modes on the metallic core [38], as well as from lossy surface waves with larger values of k_z [51].

One can obtain the normal modes of the geometry under consideration by setting the free vectors to zero in Eq. (4.5) and solving the resulting homogeneous system of equations [32]. This kind of system has a non-trivial solution only when the determinant of the characteristic matrix $\Delta(n, k_z)$ is set to zero. Due to the complex form of $\Delta(n, k_z)$ we solve this equation numerically. We consider the case of a Ag core, where experimental data are used for the dielectric permittivity, $\varepsilon_1 = \varepsilon_{\mathrm{Ag}}(\omega)$ [129], coated with a dielectric with ε_2 and embedded in air, $\varepsilon_3 = 1$. Fig. 4.2 presents the dispersion curves for surface plasmons of different orders n. In panel 4.2a the core radius is $a = 40$ nm and the outer radius is $b = 50$ nm while for panel 4.2b we have $a = 80$ nm and $b = 90$ nm. The dielectric permittivity of the coating is $\varepsilon_2 = 2$ in both panels. The horizontal line with the value $\omega = \omega_{\mathrm{SP}} = 5.3\,\mathrm{fs}^{-1}$ represents the surface plasmon frequency, i.e. the asymptotic value of ω for $k \to \infty$, for all the surface plasmon dispersion curves. This frequency corresponds to a surface plasmon wavelength of $\lambda_{\mathrm{SP}} = 355\,\mathrm{nm}$. In panel 4.2a the surface plasmon dispersion curves with $n > 1$ lie close to the SP frequency ω_{SP}, while in panel 4.2b the surface plasmon dispersion curves reach their asymptotic value for $n > 2$. The value of n above which the dispersion curves are close to ω_{SP} increases with the size of the metallic core.

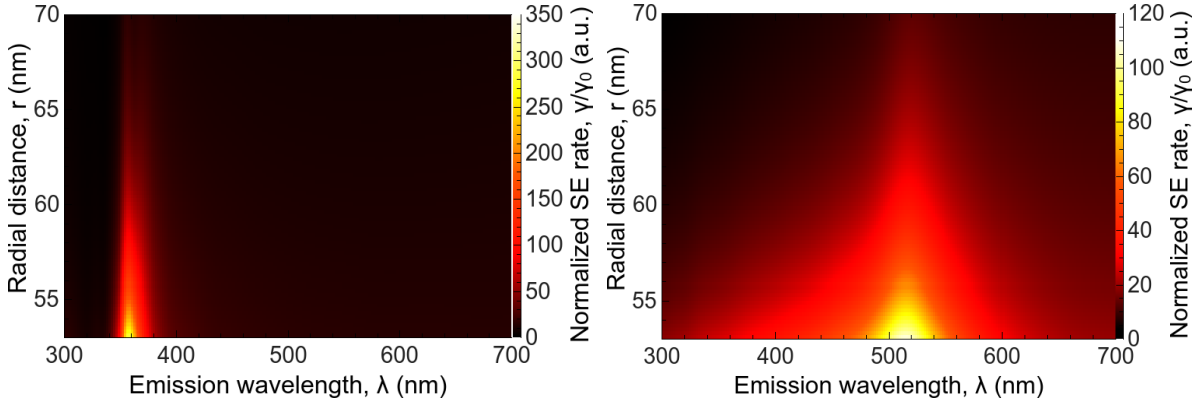

(a) *Ag core* **(b)** *Au core*

Figure 4.3: *Normalized SE rate, $\tilde{\gamma} = \gamma/\gamma_0$, near a coated metallic cylinder as a function of the radial distance, r, and emission wavelength, λ, of the emitter. The core radius is $a = 40$ nm and outer radius is $b = 50$ nm. The coating has constant dielectric permittivity $\varepsilon_2 = 2$ and the surrounding medium is air, $\varepsilon_3 = 1$. (a) Ag core, $\varepsilon_1 = \varepsilon_{Ag}(\omega)$ (b) Au core, $\varepsilon_1 = \varepsilon_{Au}(\omega)$. The dipole moment of the emitter is radial.*

4.3 Results and Discussion

Using the formalism developed in the previous section, the SE and ET functions and rates are now calculated for quantum systems in the presence of a dielectrically coated metallic cylinder, with core radius a and outer radius b. All the results have been obtained for transition dipoles that are radially oriented, and we therefore use the $\rho\rho$ component of the Green's tensor.

4.3.1 Spontaneous emission rate

In this section the influence of the coated cylinder on the SE rate of a nearby quantum emitter is investigated. The normalized SE rate of the quantum emitter is defined as $\tilde{\gamma} = \gamma/\gamma_0$ which is the ratio of the SE rate in the presence of the coated metallic cylinder, γ, to the free space SE rate, γ_0, see Sec. 2.3.1. Thus the normalized SE rate, $\tilde{\gamma}$, gives the enhancement or the inhibition of the SE rate with respect to the free space value due to the presence of the coated metallic cylinder.

Firstly, the case of a coated cylinder of core radius $a = 40$ nm and outer radius $b = 50$ nm is considered. Figure 4.3 shows contour plots of the normalized SE rate, $\tilde{\gamma}$, as a function of the position of the emitter and its emission wavelength, for both Ag and Au cores. The normalized SE rate is enhanced close to the metallic core and for an emission wavelength close to the SP wavelength. Excitation of SPs on the coated cylinder requires momentum matching between the excitation field and the SP mode. This momentum matching is provided, in this case, by the dipole near-field of the quantum emitter. Consequently, as the dipole is moved away from

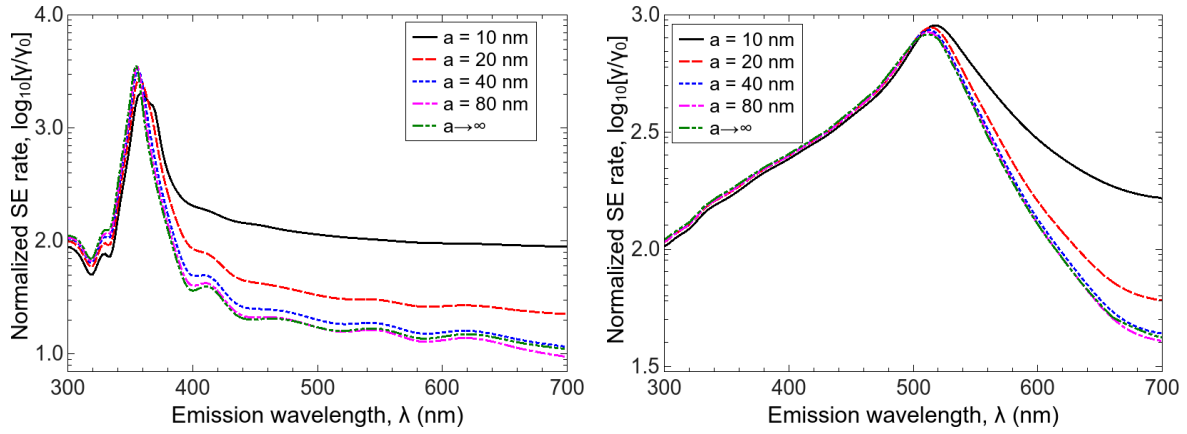

(a) *Ag core* **(b)** *Au core*

Figure 4.4: *Normalized SE rate, $\tilde{\gamma} = \gamma/\gamma_0$, as a function of the emission wavelength, λ, of the emitter, for several core radii, a. The position of the emitter is fixed at $r = a + 5$ nm, and its dipole moment is radial. The surrounding medium is air, $\varepsilon_3 = 1$, the coating has $\varepsilon_2 = 2$ and the core is metallic. (a) Ag core $\varepsilon_1 = \varepsilon_{Ag}(\omega)$ (b) Au core $\varepsilon_1 = \varepsilon_{Au}(\omega)$. The SE rate in the limit $a \to \infty$ is also shown for comparison.*

the metallic core, its near-field cannot excite the SP modes and, at larger distances, we recover the free space value of the SE rate. The SP wavelength for the Ag core is $\lambda_{\mathrm{Ag}} = 356$ nm while the Au SP wavelength is $\lambda_{\mathrm{Au}} = 520$ nm.

In Fig. 4.4 the normalized SE rate is investigated as a function of the emission wavelength of the emitter, for a fixed coating thickness $d = 10$ nm, and a fixed position of the emitter, $r = a + 5$ nm, in the middle of the coating. Four cases for the core radius, $a = 10$ nm, $a = 20$ nm, $a = 40$ nm and $a = 90$ nm are considered. As the core radius is increased, the SP wavelength does not change, as it does not depend on the cylinder radius, see Fig. 4.2. When the emission wavelength is above the SP wavelength, corresponding to frequencies below ω_{SP} in Fig. 4.2, the SE rate exhibits a strong dependence on the size of the core. More precisely, the SE is reduced as the size of the core is increased and this can be explained by the fact that in this wavelength regime, the emitter can couple to the SP modes of the coated cylinder. SPs with a larger wavenumber give a larger contribution to the SE rate, though their influence is more constrained to the surface of the core. For a given frequency in this range, the SP wavenumber varies inversely as the core size, and, therefore, smaller cores produce larger SE rates of the emitter. For core radii above $a = 40$ nm, the SE rate no longer depends on the core size and is, in essence, the same as the SE rate for a core of infinite size, also shown in Fig. 4.4. When the emission wavelength is close to or below the SP wavelength, SPs of higher order and with a dispersion curve very close to the SP wavelength begin to contribute to the SE rate. Coated cylinders with a larger core support a larger number of these high-order SPs which, therefore, give a larger contribution to the SE rate of the emitter. The dependence of the SE rate on the

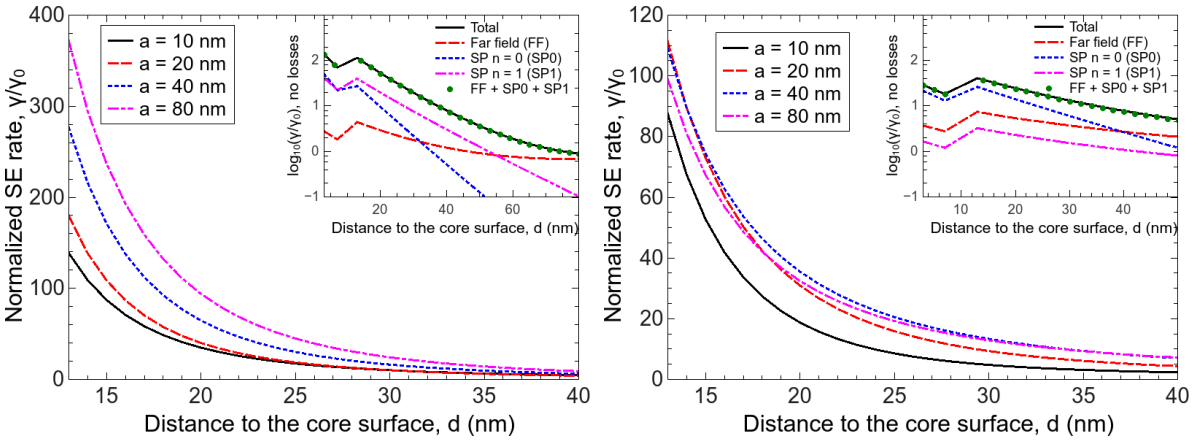

(a) *Ag core* **(b)** *Au core*

Figure 4.5: *Normalized SE rate, $\tilde{\gamma} = \gamma/\gamma_0$, as a function of the distance of the emitter from the surface of the core, d, for several core radii, $a = 10nm, 20nm, 40nm, 80nm$. The surrounding medium is air, $\varepsilon_3 = 1$, the coating has a constant dielectric permittivity $\varepsilon_2 = 2$ and thickness $b - a = 10$ nm, and the core is metallic with: (a) Ag core and (b) Au core. The dipole moment of the emitter is radial. The insets of both panels show the different contributions of the radiative and SP modes to the total SE rate in the absence of losses, for $a = 40nm$ and $b = 50nm$.*

size of the core is then reversed, increasing with core size, though not very strongly. The limit $a \to \infty$ is seen to hold in both wavelength regimes, above and below the SP wavelength.

Apart from a larger SE rate for the Ag core, the main difference between the Au and Ag cores is that the features for a Ag core are sharper than those for a Au core. For the latter, the dependence of the normalized SE rate, $\tilde{\gamma}$, on the emission wavelength has a broader and shallower peak around the SP wavelength. This is due to the larger absorption of Au compared with Ag, $\mathrm{Im}[\varepsilon_{\mathrm{Au}}(\omega)] > \mathrm{Im}[\varepsilon_{\mathrm{Ag}}(\omega)]$. Furthermore, the convergence of the SE rate to the limiting value for $a \to \infty$ occurs at a lower value of the core size, $a \gtrsim 20\,\mathrm{nm}$.

In Figure 4.5 the normalized SE rate, $\tilde{\gamma}$, is presented as a function of the distance of the emitter from the surface of the core for the four different core radii. The emission wavelength of the quantum emitter is the same for all curves in each panel, for Fig. 4.5a $\lambda = 356\,\mathrm{nm}$ and for Fig. 4.5b $\lambda = 520\,\mathrm{nm}$, respectively, placing it in the regime where the SE rate increases with the size of the core. In Fig. 4.5 the emitter is always outside the coating, in contrast to Fig. 4.4 where the emitter was placed in the middle of the coating. Because the transition dipole moment of the emitter is normal to the surface of the coating, its SE rate will have a discontinuity as the emitter moves from the coating in the background medium. As a result of this, the values of the SE rate in the background medium can be considerably different from the values inside the coating. Again, it is evident that for the Ag core, the normalized SE rate, $\tilde{\gamma}$, has larger values compared with the Au core. This different behavior of the coated cylinders

with Ag and Au core can once again be attributed to the larger absorption of Au.

The insets in the Fig. 4.5 show the different contributions to the SE rate when the core radius is $a = 40$ nm and the outer radius $b = 50$ nm using the same parameters described in the previous paragraph. For these calculations, the losses in the metal are set to zero [40], to better illustrate the SP contributions. In order to analyze the different contributions to the SE rate depicted in Fig. 4.5 the SP wavenumber, k_{SP}, needs to be extracted. This is done by using the dispersion curves shown in Fig. 4.2 for the relevant geometrical and material parameters. In general, for a specific emission frequency of the quantum emitter the surface plasmon dispersion curves determine the number of SP modes that can be excited by the emitter and their wavenumber. As panel 4.2a shows, the quantum system cannot excite any SP mode when its emission frequency is above the SP frequency $\omega_{\mathrm{SP}} = 5.3\ \mathrm{fs}^{-1}$. For emission frequencies smaller than $\omega_{\mathrm{min}} = 3.5\ \mathrm{fs}^{-1}$, the quantum system can only couple with the fundamental mode, $n = 0$ [38, 51].

By choosing the emission frequency of the quantum system in the interval $(\omega_{min}, \omega_{SP})$, the SP with angular momentum numbers $n = 0, 1$ can be excited, see Fig. 4.2. These SPs have wavenumbers k_{SP0} and k_{SP1}, respectively, which correspond to two poles of the generalized scattering coefficients from (4.10). The integrand from Eq. (4.11) when, $\mathbf{r} = \mathbf{r}_s = r$, has the general expression

$$\mathrm{d}\mathfrak{G}_n^{ii}(k_z, r) = \frac{1}{\mathrm{Det}\big(\Delta_n(k_z)\big)} F_n^{ii}(k_z, r), \tag{4.12}$$

where $i = 1, 2, 3$ for the three different media, $F_n^{ii}(k_z, r)$ is a function containing all the different contributions to the integrand, except the pole contribution which is given by the determinant of the characteristic matrix. Using Cauchy's residue theorem, the contributions of the two poles to the Green's tensor can be written as

$$\mathfrak{G}_{s(rr)}^{ii}(\mathbf{r}, \mathbf{r}, \omega)_{\mathrm{SP}} = \pi i \left(\frac{F_0^{ii}(k_{SP0}, r)}{\frac{\partial}{\partial k_z}\big(\mathrm{Det}(\Delta_0(k_z))\big)\Big|_{k_z = k_{SP0}}} + \frac{2F_1^{ii}(k_{SP0}, r)}{\frac{\partial}{\partial k_z}\big(\mathrm{Det}(\Delta_1(k_z))\big)\Big|_{k_z = k_{SP1}}} \right), \tag{4.13}$$

where the factor of 2 for the second SP contribution of comes from the fact that the $n = 1$ and $n = -1$ modes have equal contributions.

Using all the above, the contribution of each SP mode to the total SE rate in the inset of Fig. 4.5 is becoming clear. For the case of Ag core, inset Fig. 4.5, the main contribution to the SE rate comes from the $n = \pm 1$ modes close to the interface between media 2 to 3. Inside the dielectric coating the contributions from the SP modes $n = 0$ and $n = \pm 1$ becomes almost

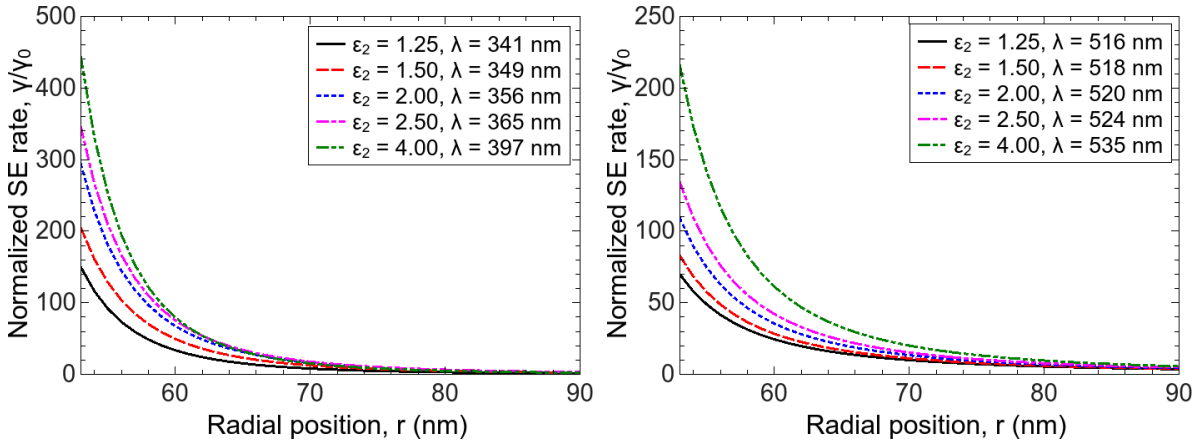

(a) *Ag core* **(b)** *Au core*

Figure 4.6: *Normalized SE rate, $\tilde{\gamma} = \gamma/\gamma_0$, as a function of the radial position of the emitter, r, for several dielectric permittivities of the coating. The surrounding medium is air, $\varepsilon_3 = 1$, the coating thickness is $b - a = 10$ nm and the core is metallic, with: (a) Ag core and (b) Au core. The radius of the core is $a = 40$ nm. The dipole moment of the emitter is radial.*

equal due to the fact that the near field of the QE is strongly coupled with the Ag core, thus fully exciting the SP modes. As the distance between the QE and the Ag core is increased, the near field of the QE begins to decouple from the Ag core and the emission to the far field dominates. Similar behavior is followed for the Au core, inset of Fig. 4.5, but now the coupling with the modes $n = \pm 1$ is smaller due to the poorer coupling with this mode in the dispersion relation. In both insets, the sum of the contributions from radiative and SP modes of order $n = 0$ and $n = 1$ and the full numerical integration overlap perfectly. When losses are considered, there is an additional contribution from lossy surface modes, especially for the case when the emitter is close to the surface of the core.

In Figure 4.6 the effect of different values of the dielectric permittivity of the coating on the SE rate is investigated. The x-axis shows the radial position of the emitter. In panel 4.6a a Ag core and in panel 4.6b a Au core are considered, where the coated cylinder has a core radius $a = 40$ nm and an outer radius $b = 50$ nm. In both panels the normalized SE rate, $\tilde{\gamma}$, increases as we increase the dielectric permittivity of the coating. The emission wavelength of the emitter is chosen to be close to the SP wavelength and as the dielectric permittivity is increased, the SP wavelength redshifts, as can be seen in the legends in Figure 4.6. This redshift is due to the fact that the SP condition depends on ε_2 (for a planar interface, this condition is $\mathrm{Re}(\varepsilon_1) = -\varepsilon_2$ at ω_{SP}).

4.3.2 Energy transfer function

In this section we consider the ET function, see Sec. 2.3.2, for a pair of quantum emitters where the donor is excited and the acceptor is in the ground state.

In Fig. 4.7 a contour plot of the normalized ET function is presented for 4 different coated cylinder geometries. The figure shows a *xy* cross-section of a coated cylinder with a core radius $a = 40$ nm and an outer radius $b = 50$ nm. The position of the donor is fixed on the *x*-axis at $r_D = 55$ nm and is indicated by the arrow. The ET function is calculated for the acceptor positioned at each point in the plot. The emission wavelength of the donor has been chosen to be close to the SP wavelength in each case.

Firstly the Ag core and Au core geometries are considered, shown in panels 4.7a and 4.7b respectively. The donor wavelength, λ_D, is 356 nm for the Ag core and 520 nm for the Au core. Panel 4.7a shows that the normalized ET function, $\tilde{\Gamma}$, is concentrated in hot spots around the circumference of the coated cylinder. The number of hot spots is associated with the contributions of modes of different orders, n, of the Bessel and Hankel functions. In general, the number of hot spots, δ, is given by $\delta = 2n + 1$. It can be seen that excitation of surface plasmon modes can significantly enhance the ET function, by up to 4 orders of magnitude.

Panel 4.7b shows the normalized ET function, $\tilde{\Gamma}$, when the material of the core is Au. The behavior is similar to the case of a Ag core, showing the same number of hot spots around the circumference. However, because of the higher losses in Au, the enhancement is much lower.

To investigate the influence of the dielectric coating on the ET function two additional cases have been considered, that of a metallic core with no coating and that of a simple dielectric cylinder. Panel 4.7c shows a contour plot of the *xy* cross-section of the normalized ET function for a Ag cylinder of radius $a = 40$ nm, for which the position of the donor is the same as in panel 4.7a. The emission wavelength of the donor is chosen close to the SP wavelength for this case, which is $\lambda_{SP} = 340$ nm. It is clear that in the absence of the dielectric coating, the normalized ET function, $\tilde{\Gamma}$, across the Ag cylinder is considerably smaller. Therefore, for the case of the coated metal core cylinder the dipole near field is able to couple with the coating. Additionally, the dielectric material enhances the strength of the near field, as we have already shown in the section on the SE rate, i.e. Fig. 4.6.

It is also instructive to consider a purely dielectric cylinder, where the metallic core is replaced with a material with a constant dielectric permittivity, $\varepsilon_1 = 4$. The emission wavelength, $\lambda_D = 356$ nm, and the donor position are identical to those in Fig. 4.7a to allow for direct comparison. It can be seen that the normalized ET function, $\tilde{\Gamma}$, is significantly smaller than in the other panels. Outside the cylinder it has a value $\tilde{\Gamma} \approx 7$ very close to the dielectric interface and, as the distance is increased, it reverts to the free space value. The importance of the excitation

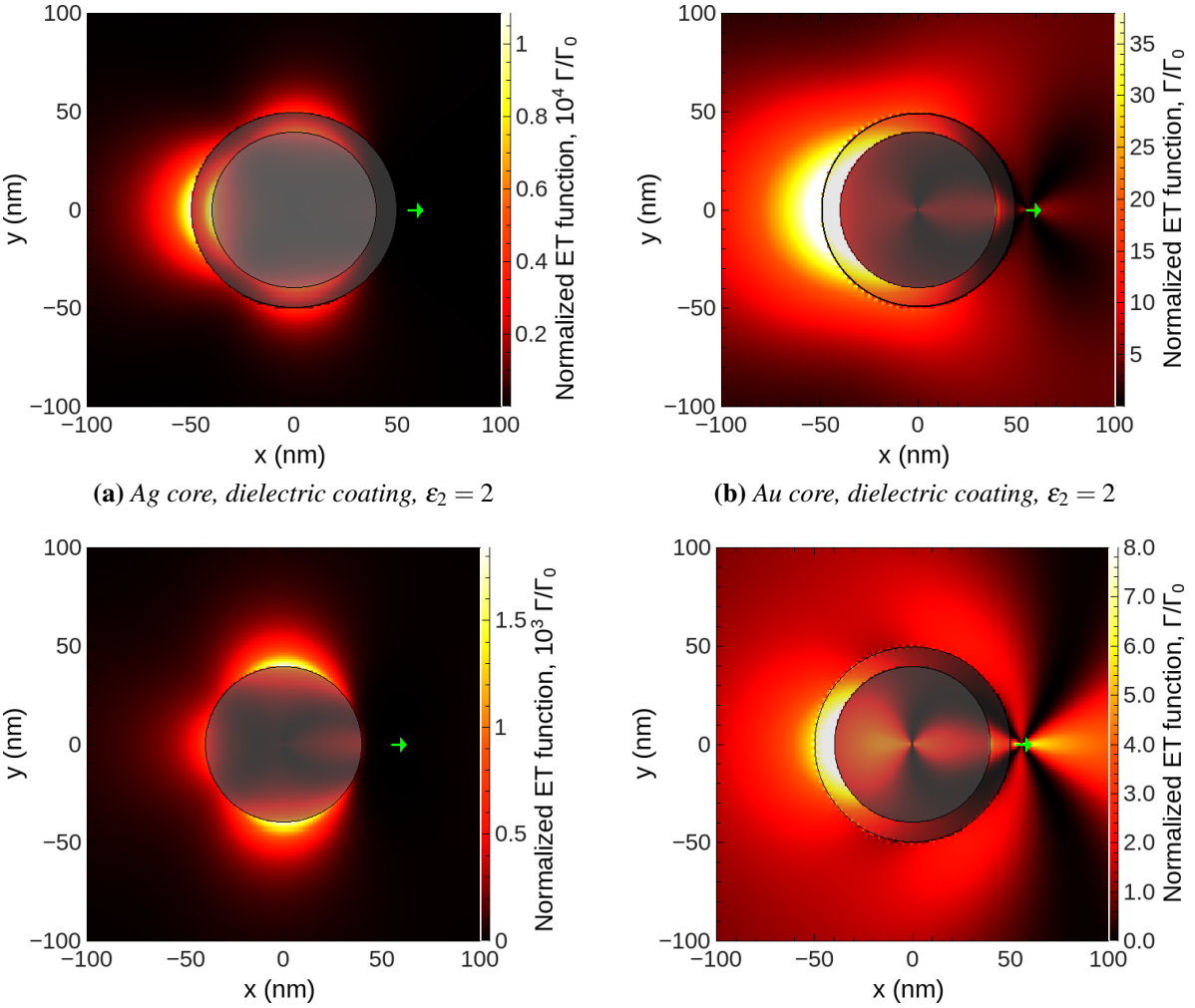

(a) *Ag core, dielectric coating,* $\varepsilon_2 = 2$

(b) *Au core, dielectric coating,* $\varepsilon_2 = 2$

(c) *Ag core, no coating,* $\varepsilon_2 = 1$

(d) *Dielectric core,* $\varepsilon_1 = 4$*, dielectric coating,* $\varepsilon_2 = 2$

Figure 4.7: *An xy contour plot of the normalized ET rate,* $\tilde{\Gamma} = \Gamma/\Gamma_0$*, near a coated metallic cylinder with a core radius* $a = 40$ *nm and an outer radius* $b = 50$ *nm. The dielectric permittivity of the coating is* $\varepsilon_2 = 2$ *and the surrounding medium is air,* $\varepsilon_3 = 1$*. The position of the donor is fixed for all panels at* $r_D = 55$ *nm on the x-axis. The material of the core cylinder and the emission wavelength of the donor are different for each panel: (a) Ag core with* $\lambda_D = 356$ *nm (b) Au core with* $\lambda_D = 520$ *nm (c) Ag core, no coating and* $\lambda_D = 340$ *nm (d) Dielectric core with* $\varepsilon_1 = 4$ *and* $\lambda_D = 356$ *nm. For each case where the core is metallic, the emission wavelength matches the SP wavelength. Both the donor and acceptor dipole moments are radial.*

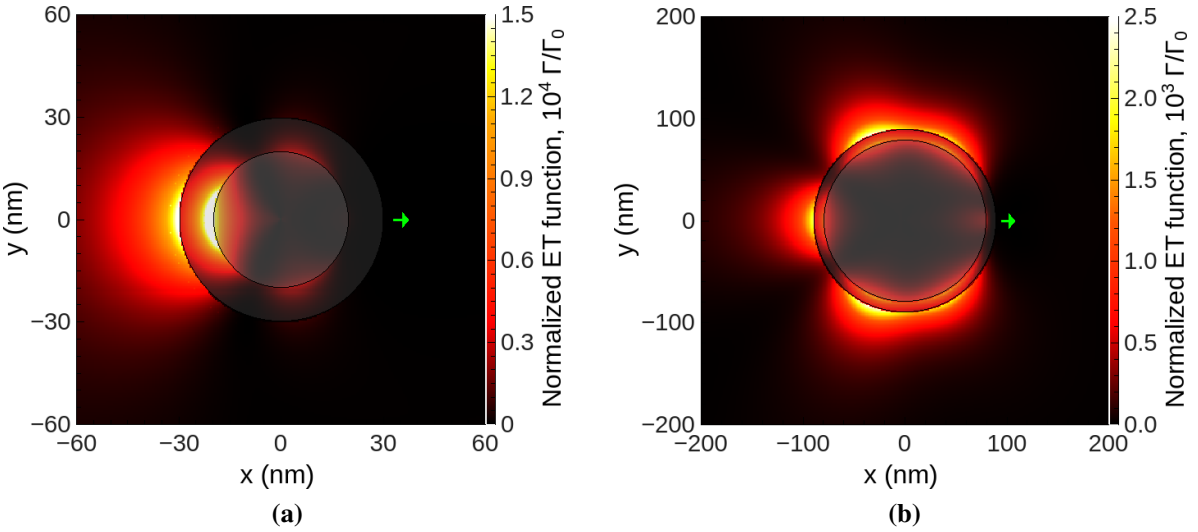

Figure 4.8: *A xy contour plot of the normalized ET rate, $\tilde{\Gamma} = \Gamma/\Gamma_0$, near a coated cylinder with a Ag core, and a dielectric coating ($\varepsilon_2 = 2$), embedded in air ($\varepsilon_3 = 1$). (a) $a = 20$ nm, $b = 30$ nm, $r_D = 35$ nm and $\lambda_D = 356$ nm; (b) $a = 80$ nm, $b = 90$ nm, $r_D = 100$ nm and $\lambda_D = 356$ nm. Both the donor and acceptor dipole moments are radial.*

of the SP modes for a large enhancement of the ET function is thus evident when we compare the dielectric core case with the metallic core cases considered in the rest of Fig. 4.7. The reader should note the different orders of magnitude for the color maps shown in Fig. 4.7.

In Fig. 4.8 the effect of changing the size of the coated cylinder on the ET mechanism is investigated. The normalized ET function, $\tilde{\Gamma}$, is presented in a *xy* cross-section of the coated cylinder. In both panels the core material is Ag, with $\varepsilon_2 = 2$ and $\varepsilon_3 = 1$. For Fig. 4.8a we have $a = 20$ nm, $b = 30$ nm, the position of the donor $r_{\mathrm{D}} = 35$ nm on the *x*-axis, and the emission wavelength of the donor is close to the SP wavelength at $\lambda_{\mathrm{D}} = 356$ nm. It can be seen that the normalized ET function, $\tilde{\Gamma}$, exhibits one hot spot at a position on the opposite side of the cylinder relative to the donor and is confined around the periphery of the coated cylinder. When larger dimensions for the coated cylinder are considered, $a = 80$ nm, and $b = 90$ nm as shown in Fig. 4.8b, the number of hot spots increases and the spatial extent of the enhancement of the normalized ET function, $\tilde{\Gamma}$, also increases. For panel 4.8b, the position of the donor is $r_{\mathrm{D}} = 100$ nm on the *x*-axis and the donor emission wavelength is close to the SP wavelength, $\lambda_{\mathrm{D}} = 356$ nm. The number of hot spots is given by the coupling to surface plasmons of different orders *n*, the dispersion curves of which are shown in Fig. 4.2.

4.3.3 Energy transfer efficiency

In the previous two sections generic donor-acceptor pairs with δ-like emission and absorption spectra have been considered, i.e. single-frequency spectra. As such, the normalized SE or ET rates were determined by the optical response of the coated metallic cylinder, through the Green's tensor.

This constraint now will be relaxed and realistic donor emission spectra, $f_{\mathrm{D}}(\lambda)$, and acceptor absorption spectra, $\sigma_{\mathrm{A}}(\lambda)$ are considered [3, 130]. These spectra describe statistical ensembles of donor-acceptor pairs. When the donor dipole is excited it has two ways of relaxing to the ground state: it can either transfer its excitation energy to the acceptor dipole with an ET rate k_{ET}, or it can relax with decay rate k_{SE}. The decay rate k_{SE} takes account of photon emission into the far-field, intrinsic non-radiative recombination paths, coupling to surface plasmon modes and losses in the metallic core. The SE and ET processes are, therefore, in competition with each other and we introduce an energy transfer efficiency to describe this competition. In what follows, they will be considered donors with a quantum yield of one, $Y_0 = 1.0$, which assumes no intrinsic losses such as phonon relaxation, etc.

Using the expressions introduced in Eqs. (2.29) and (2.36) for the SE and ET rates of ensembles of emitters and donor-acceptor pairs, the energy transfer efficiency η is calculated using the expression Eq. (2.37) as [140]

$$\eta = \frac{k_{\mathrm{ET}}}{k_{\mathrm{SE}} + k_{\mathrm{ET}}}. \tag{4.14}$$

This quantity gives the relative contribution of the energy transfer process to the total decay rate of the donor. If the ET efficiency, η, has a value $\eta > 50\%$, then the decay of the excited state of the donor occurs mainly by energy transfer to the acceptor, rather than relaxation into photon or SP modes.

Two donor-acceptor pairs will be considered. The donor emission and acceptor absorption spectra are both given by a Gaussian distribution Eq. (2.38), we rewrite here the expression

$$A_{\mathrm{q}i}\, \mathrm{e}^{-(\lambda-\lambda_{\mathrm{q}i})^2/\Delta\lambda_{\mathrm{q}i}^2}, \tag{4.15}$$

where $\mathrm{q} = D$ represents the donor, $\mathrm{q} = A$ represents the acceptor, $i = 1$ corresponds to the on-resonance case, and $i = 2$ corresponds to the off-resonance case. $A_{\mathrm{q}i}$ is a normalization constant, $\lambda_{\mathrm{q}i}$ gives the position of the spectral peak and $\Delta\lambda_{\mathrm{q}i}$ is the half width half maximum (HWHM) of the spectrum. The normalization constant of the donor emission spectrum is given as $A_{\mathrm{D}i}^{-1} = \int_0^\infty \mathrm{d}\lambda\, f_{\mathrm{D}}(\lambda)$. The HWHM will be $\Delta\lambda_{\mathrm{D}i} = 20$ nm for both donor-acceptor

pairs, which corresponds to a typical spectrum of a fluorescent dye, e.g. fluorescein [130]. The constant for the acceptor absorption spectrum is $A_{\mathrm{A}i} = 0.021$ nm^2, while the HWHM is $\Delta\lambda_{\mathrm{A}i} = 50$ nm. The preceding values are common to both donor-acceptor pairs. The two donor-acceptor pairs do however differ with respect to the positions of their emission and absorption peaks. For the first pair, the donor emission peak is at $\lambda_{\mathrm{D1}} = 363$ nm, while the absorption maximum is at $\lambda_{\mathrm{A1}} = 373$ nm; for the second pair $\lambda_{\mathrm{D2}} = 453$ nm and $\lambda_{\mathrm{A2}} = 463$ nm. Panels 4.9a and 4.9b show the normalized emission spectrum of the donor, $f_{\mathrm{D}}(\lambda)$, and the absorption cross section spectrum of the acceptor, $\sigma_{\mathrm{A}}(\lambda)$, together with the energy transfer function, $\Gamma(\lambda)$. Since the energy transfer function, $\Gamma(\lambda)$, is given by the Green's tensor of the coated metallic cylinder, Eq. (2.34), it is the same for both donor-acceptor pairs, with a peak close to the surface plasmon wavelength, $\lambda_{\mathrm{SP}} \approx 365$ nm. This SP wavelength is different from what we used in the previous sections, as the thickness of the coating is now $b - a = 5$ nm, whereas before it was 10 nm. The permittivity of the coating is the same, $\varepsilon_2 = 2$, and the background medium is air, $\varepsilon_3 = 1$. The donor emission spectrum, $f_{\mathrm{D}}(\lambda)$, and acceptor absorption spectrum, $\sigma_{\mathrm{A}}(\lambda)$, of the first donor-acceptor pair considered both have a good overlap with $\Gamma(\lambda)$, i.e. this pair is on-resonance, see Fig. 4.9a. The overlap is poor for the second donor-acceptor pair, i.e. it is off-resonance, see Fig. 4.9b.

The Förster radius, R_0, is defined as the donor-acceptor separation at which η is 50% [52]. The Förster radius is calculated to be 6.07 nm and 7.04 nm in free space for the first and second donor-acceptor pair, respectively. These values were calculated from the spectral overlap of the normalized donor emission and acceptor absorption spectra from Eq. (2.40), where the host medium is air with a refractive index of 1.

The next step will be to consider the influence of the coated cylinder on the ET efficiency η. The core radius is $a = 10$ nm and the outer radius is $b = 15$ nm. The position of the donor is kept fixed at $r_{\mathrm{D}} = 20$ nm on the x-axis. In panel 4.9c we plot the value of the ET efficiency, η, as a function of the radial position of the acceptor diametrically opposite to the donor, for the two donor-acceptor pairs, the shaded area defining the area inside the coating. For the on-resonance case, the ET efficiency has values of $\eta = 23\%$ close to the Ag-dielectric interface while for the off-resonance case, cf. 4.9b, the value of the ET efficiency is $\eta = 1.3\%$ close to the Ag-dielectric interface. These values can be compared with the free-space energy transfer efficiency of 0.0077% and 0.017% at a donor-acceptor separation of 30 nm, corresponding to the diameter of the coated metallic cylinder, for the first and second donor-acceptor pair, respectively. It can also be noted that the Förster radius in free-space for the first donor-acceptor pair is smaller than for the second. Therefore, the enhanced energy transfer range near the coated metallic cylinder, is a consequence of the excitation of SP modes on the coated

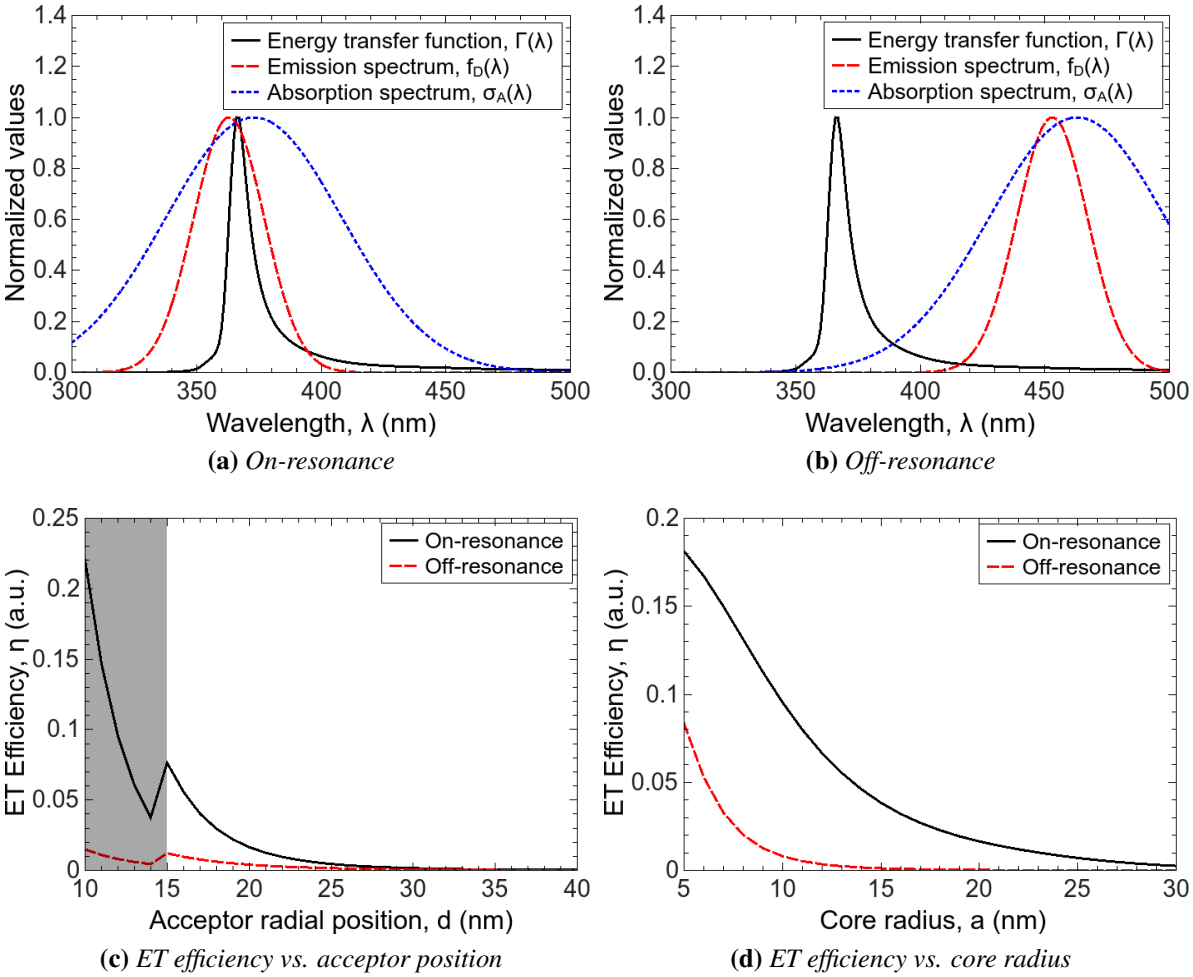

(a) *On-resonance* **(b)** *Off-resonance*

(c) *ET efficiency vs. acceptor position* **(d)** *ET efficiency vs. core radius*

Figure 4.9: *(a) - (b) Normalized donor emission spectrum, $f_D(\lambda)$, acceptor absorption spectrum, $\sigma_A(\lambda)$, and ET function, $\Gamma(\lambda)$, for two different donor/acceptor pairs: (a) On-resonance and (b) Off-resonance. (c) ET efficiency, η, for a coated metallic cylinder, with a core radius $a = 10$ nm, outer radius $b = 15$ nm, for a donor placed at $r_D = 20$ nm on the x-axis, as a function of acceptor distance, d, from the core surface, diametrically opposite the donor. (d) ET efficiency, η, as a function of core radius, a, for an outer radius $b = a + 5$ nm, donor position $r_D = a + 10$ nm and acceptor position $r_A = -a - 2$ nm, both on the x-axis.*

cylinder.

In panel 4.9d the influence of the core radius, a, of the coated cylinder on the ET efficiency, η, is investigated by keeping the thickness of the coating fixed at 5 nm. The dielectric permittivities of the coated cylinder layers are the same as before. The position of the donor is $r_{\mathrm{D}} = a + 10$ nm, in air, and the position of the acceptor is $r_{\mathrm{A}} = -a - 2$ nm, inside the coating. In panel 4.9d it is observed that for the case where the emission and absorption spectra are on-resonance, the ET efficiency reaches values as high as $\eta = 19.4\%$ at $a = 5$ nm and it has values $\eta > 10\%$ for core radii $a < 10$ nm. When the donor-acceptor pair from panel 4.9b is considered, it is observed that the maximum values of the energy transfer efficiency are smaller, $\eta = 7.9\%$ at $a = 5$ nm and it drops-off more abruptly as a function of core size. Comparing the on- and off-resonance cases shows that a large overlap of the donor emission spectrum and acceptor absorption cross-section with the SP peak in the spectrum of the ET function, $\Gamma(\lambda)$, can significantly enhance the ET efficiency, η, and mediate the interactions over larger distances.

In panel 4.10a the influence of the dielectric permittivity of the coating, ε_2, on the SE rate of a donor, k_{SE}, and the ET rate between a donor and an acceptor, k_{ET}, is investigated for the geometry considered in the previous paragraph with parameters $a = 10$ nm and $b = 15$ nm. For the donor emission and acceptor absorption spectrum, the data from panel 4.9a are used, the on-resonance case. The donor is located at $r_{\mathrm{D}} = 20$ nm and the acceptor is located at $r_{\mathrm{A}} = -20$ nm, both on the x-axis. The SE and ET rates are expressed in units of free space SE rate, γ_0. The SE rate, k_{SE}, is two orders of magnitude larger compared to the ET rate, k_{ET}. This is due to the fact that the distance between the donor and the acceptor is large and thus the factor $|\mathbf{n}_{\mathrm{A}} \cdot \mathfrak{G}(\mathbf{r}_{\mathrm{A}}, \mathbf{r}_{\mathrm{D}}, \omega) \cdot \mathbf{n}_{\mathrm{D}}|^2$ of Eq. (2.36) is weak compared with the factor $\gamma(\lambda)$ of Eq. (2.29). The SE rate reaches a maximum value at $\varepsilon_2 = 2.5$, while the maximum value of the ET rate, k_{ET}, is attained at $\varepsilon_2 = 2.25$. The interplay between the SE and ET contributions to the ET efficiency, η, will determine for which value of the dielectric permitivitty of the coating, ε_2, the ET efficiency reaches its maximum, as seen in panel 4.10b.

Fig. 4.10b shows the influence of the dielectric permitivitty of the coating, ε_2, and its thickness, on the ET efficiency, η, for the same inner core radius, $a = 10$ nm, and donor and acceptor spectral properties. The donor position is $r_{\mathrm{D}} = b + 5$ nm and the acceptor position $r_{\mathrm{A}} = -b - 5$ nm, both on the x-axis. In order to quantify the influence of the coated cylinder geometry on the ET efficiency, the normalized ET efficiency, $\tilde{\eta}$, is introduced as $\tilde{\eta} = \eta/\eta_0$, where η is the ET efficiency in the presence of the coated cylinder and η_0 is the free space ET efficiency. The normalized ET efficiency, $\tilde{\eta}$, decreases as we increase the outer radius, b, due to the decoupling between the near field of the quantum emitters and the SP modes of the

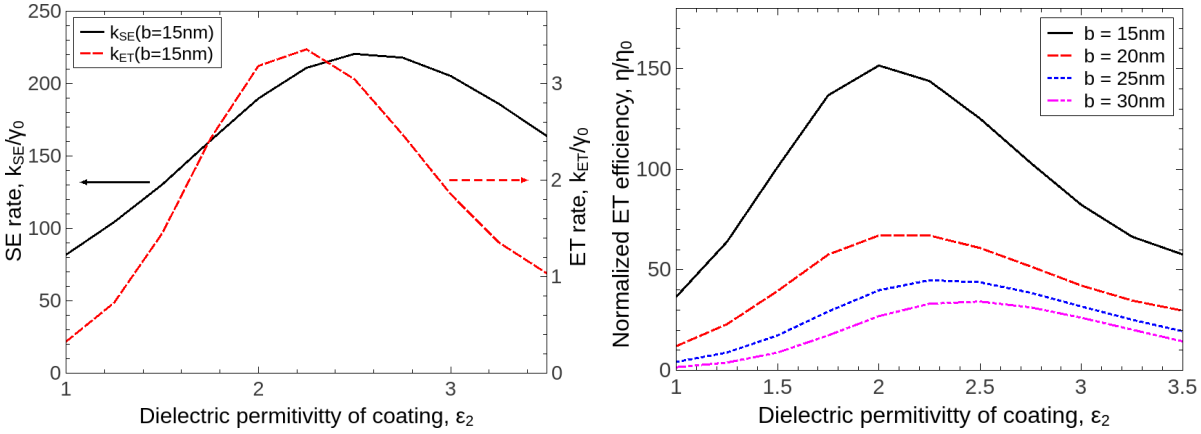

(a) *SE and ET rates, k_{SE} and k_{ET}.* **(b)** *Normalized ET efficiency, $\tilde{\eta}$.*

Figure 4.10: *Coated cylinder of inner radius, $a = 10$ nm, donor position $r_D = b+5$ nm and acceptor position $r_A = -b-5$ nm, both on the x-axis. (a)SE rate, k_{SE}, of the donor and ET rate between donor-acceptor for outer radius $b = 15$ nm. (b) Normalized ET efficiency, $\tilde{\eta}$, as a function of the dielectric permittivity of the coating, for several values of the coating thickness.*

metallic core. As the outer radius, b, is increased even more, the ET efficiency reverts to its free space value and we have $\tilde{\eta} \to 1$. The peak in the normalized ET efficiency for $b = 15$ nm occurs at a value of the dielectric permittivity of the coating of $\varepsilon_2 = 2$. By varying the dielectric permitivitty, the ET function is shifted in wavelength. The $\varepsilon_2 = 2$ is the value for the on-resonance case as shown in Fig. 4.9a. Furthermore, as the outer radius, b, is increased it is seen that the peak in the normalized ET efficiency is shifted from $\varepsilon_2 = 2$ to $\varepsilon_2 = 2.5$, due to the redshifting of the SP resonance wavelength with increasing outer radius b. Thus, the dielectric permitivitty of the coating, ε_2, and the thickness of the coating, constitute separate parameters that can be adjusted to optimally couple donor-acceptor pairs with different optical properties, maximizing the ET efficiency.

4.4 Summary and Conclusions

In this chapter the role of a dielectric coated metallic cylinder in modifying the SE rate of a single emitter and the ET rate in a donor-acceptor pair is presented. The excitation of SP modes, when the emission wavelength is close to the SP wavelength, enhances the SE and ET rates and functions by several orders of magnitude compared with their free space values.

First, the SE rate of an emitter in the presence of a coated cylinder is considered. The SE rate is enhanced through the excitation of SP modes. The enhancement is larger when the emitter is in close proximity to the metallic core and its emission wavelength is close to the SP

wavelength. The SE rate also depends on the radius of the core, and is seen to increase with the radius when the emission wavelength is close to the SP wavelength. When the dielectric permittivity of the coating is increased, the SP wavelength is red-shifted, as expected. The maximum of the SE rate follows the same trend, undergoing a red-shift. Furthermore, the value of this maximum increases with the dielectric permittivity of the coating.

Next the ET function between a donor-acceptor pair is considered. By exciting SP modes, the ET function can be enhanced by orders of magnitude, the enhancement being localized at hot-spots around the circumference of the coated cylinder. The number of these hot-spots is in direct relation to the order of the SP mode or modes being excited. The presence of the coating dielectric layer around the metallic core further increases the ET enhancement provided by the core by itself.

Furthermore, since SE and ET are competitive processes, the ET efficiency, η, is introduced in order to investigate the interplay between them. As examples, two donor-acceptor pairs are chosen, with different donor emission and acceptor absorption spectra. For the first pair, the emission and absorption spectra overlap with the ET function, given by the Green's tensor, while for the second pair, they do not. By considering a fixed geometry for the coated cylinder and varying the position of the acceptor and the core radius, a, a significant difference between on- and off-resonance emission and absorption spectra with the SP mode is evident.

Additionally, it is shown that the SP-mediated coupling between different donor-acceptor pairs can be engineered in a predictable way by controlling the refractive index of the coating as well as its thickness. These parameters can be chosen such that one can obtain an optimal coupling between donors and acceptors with specific optical properties.

For applications in which the energy transfer efficiency needs to be optimized, it is shown that fine tuning of the geometrical parameters of the dielectrically coated metallic cylinder, e.g. thickness of dielectric coating, can lead to large enhancements of the ET rate. Control of the wavelength at which the ET efficiency is maximum can be achieved through the refractive index of the dielectric coating and, for a more coarse-grained tuning, through the material of the core, i.e. Ag vs. Au.

Using noble metals, Au and Ag, the interaction length for efficient ET between pairs of donors and acceptors is enhanced compared with their free-space value, see Sec. 4.3, when there is a strong overlap of the donor emission and the acceptor absorption spectra with the SP mode. Thus, the emitters used have to emit and absorb in the visible part of the spectrum. In Sec. 1.2, see Fig. 1.3a, the dielectric permittivity of Ag and Au is presented, their main disadvantage are their material properties, due to large losses. On the other hand graphene is a material with lower losses compared with the noble metals, see Sec. 1.2. In the next chapter

graphene is used as the platform for facilitating long range tunable interactions between a pair of quantum emitters, by exciting graphene SP modes. The SP modes provided by graphene are in the infrared part of the spectrum, an area of interest for applications in telecommunication.

Chapter 5

Dynamical tuning of energy transfer efficiency on a graphene monolayer

5.1 Introduction

For the last two decades the field of plasmonics has grown intensively. Confining light in sub-wavelength structures by exciting surface plasmon-polaritons (SPP) modes has various applications in biosensing devices, light harvesting, optical nanoantennas and quantum information processing. SPPs are collective oscillations of electrons and the electromagnetic field that are excited at the interface between a dielectric and a conductor and can propagate along that interface [4]. In plasmonics, noble metals are routinely used as the conducting medium. The main drawback of using noble metals in the applications mentioned above is their large material losses [16].

Graphene constitutes an alternative to using noble metals for plasmonic applications [72–74, 146]. It is a two-dimensional material possessing unique properties [87]. This atomically thick monolayer has superior electronic and mechanical properties originating in part from its charge carriers of zero effective mass that can travel for microns without scattering at room temperatures.

An undoped graphene monolayer (GM) can absorb $\pi\alpha_0 \approx 2.3\%$ of the light incident upon it, at wavelengths in the visible part of the spectrum, where α_0 is the fine structure constant [88]. Patterned GM nanostructures can give rise to 100% absorption at specific wavelengths, which can be tuned through the applied voltage [89, 90].

In this chapter a theoretical investigation of the energy transfer (ET) efficiency between quantum emitters placed in proximity to a conducting monolayer of graphene is presented. The spontaneous emission (SE) rate of a quantum emitter (QE) and the energy transfer (ET)

rate between a donor acceptor, QEs pair, rate, are calculated using the Green's tensor formalism. The SE and ET rates are competitive processes, thus an ET efficiency is introduced, in a similar manner to Chapter 4. This quantity, which is a measure of the contribution of the energy transfer rate to the total decay rate of the donor, will show that one can efficiently transfer energy between QEs separated by distances of the order of hundreds of nanometers, due to the excitation of graphene plasmon (GP) modes on the graphene monolayer (GM).

The ET efficiency can be tuned, through gating of the GM, thus opening opportunities for possible applications, such as switching and sensing devices [79, 153, 154], light harvesting [155], plasmonic rulers [79, 156] and quantum computing [85]. Furthermore it is shown that the ET rate along the GM has two contributions, a Förster contribution, and a GP contribution, both of which can be tuned. Also it is shown that the distance dependence of ET rate between a pair of QEs, placed perpendicular to the GM, is mainly characterized by the penetration depth of the GP mode.

The chapter is structured as follows. Beginning in Sec. 5.2 with a theoretical framework in which we introduce the optical properties of the GM and the GP mode it supports (Sec. 5.2.2), the different coupling regimes of the QE-GM system are investigated, i.e. strong or weak coupling (Sec. 5.2.3). In Sec. 5.3 the results of our calculations are presented for the SE rate (Sec. 5.3.1), the ET function (Sec. 5.3.2) and the ET efficiency (Sec. 5.3.3), for different distance regimes and values of the chemical potential. Finally, in Sec. 5.4 a summary of the results and the conclusions drawn.

5.2 Theoretical Framework

The model system considered in this chapter is presented as a sketch in Fig. 5.1a. An atomically thin monolayer of graphene in the *xy*-plane is considered, suspended in vacuum. Close to this graphene monolayer, there are either a single quantum system, when investigating spontaneous emission, or two quantum emitters, for energy transfer investigations. Firstly, we calculate the Green's tensor, an important quantity for calculating the SE and ET rates, see Sec. 2.3. Next, a conductivity model for describing the optical response of the graphene monolayer and its graphene surface plasmon properties is introduced. Finally, the strong and weak coupling regimes of the QE-GM interaction are investigated .

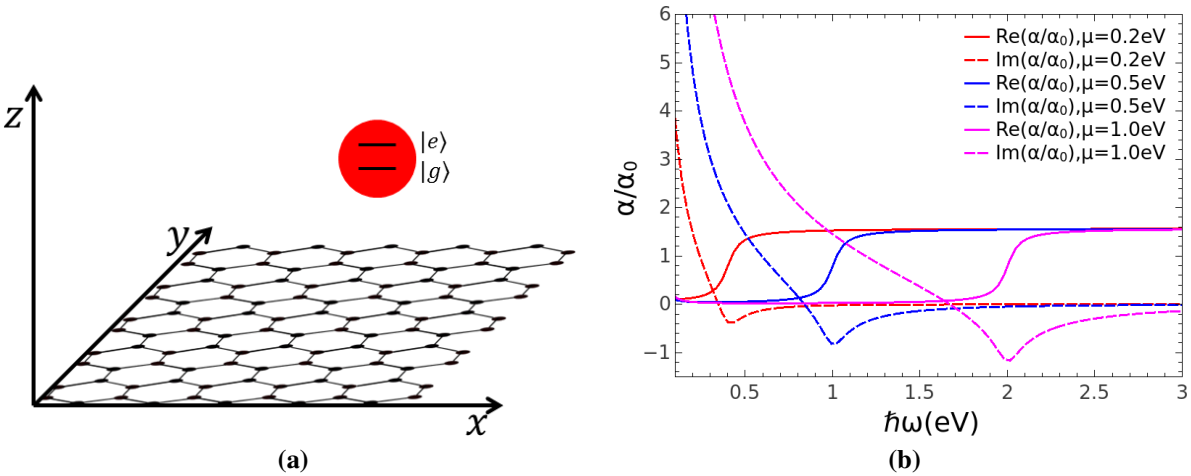

Figure 5.1: *(a) A graphene monolayer in the xy-plane, with the quantum emitter approximated as a two level system. (b) Optical response of the graphene monolayer for different values of the chemical potential, μ.*

5.2.1 Green's tensor for a graphene monolayer

We will consider two planar half-spaces with dielectric permittivities ε_1 and ε_2. The z-direction is perpendicular to the boundary between the two half-spaces. In order to calculate the Green's tensor for this system, we use the method of scattering superposition, see Sec. 3.2. The Green's tensor has the form

$$\mathfrak{G}^{(11)}(\mathbf{r},\mathbf{s},\omega) = \mathfrak{G}_h^{(11)}(\mathbf{r},\mathbf{s},\omega) + \mathfrak{G}_s^{(11)}(\mathbf{r},\mathbf{s},\omega), \tag{5.1}$$

$$\mathfrak{G}^{(21)}(\mathbf{r},\mathbf{s},\omega) = \mathfrak{G}_s^{(21)}(\mathbf{r},\mathbf{s},\omega), \tag{5.2}$$

where the first of the two labels in the superscript $(i1)$ denotes the field point, while the second denotes the source point. The subscript s denotes the scattering term, always present, while the homogeneous term $\mathfrak{G}_h^{(11)}(\mathbf{r},\mathbf{s},\omega)$ contributes only when the source and field points are in the same medium.

The scattering terms have the following expression

$$\mathfrak{G}_s^{(11)}(\mathbf{r},\mathbf{s},\omega) = \frac{i}{8\pi^2}\sum_K \int \mathrm{d}^2k_s \frac{1}{k_{z1}k_s^2} R_K^{+11-}\mathbf{K}(k_s,k_{z1},\mathbf{r})\otimes\mathbf{K}^*(k_s,-k_{z1},\mathbf{s}) \tag{5.3}$$

$$\mathfrak{G}_s^{(21)}(\mathbf{r},\mathbf{s},\omega) = \frac{i}{8\pi^2}\sum_K \int \mathrm{d}^2k_s \frac{1}{k_{z1}k_s^2} R_K^{-11-}\mathbf{K}(k_s,-k_{z2},\mathbf{r})\otimes\mathbf{K}^*(k_s,-k_{z1},\mathbf{s}) \tag{5.4}$$

where $k_s = \sqrt{k_i^2 - k_{zi}^2}$ is the in-plane propagation constant, k_{zi} is the perpendicular propagation constant in medium i, and $k_i = \frac{\omega}{c}\sqrt{\varepsilon_i}$ is the wavenumber in medium i $(i = 1,2)$. The above

expressions involve a summation over **K** which represents **M** and **N**, or the transverse electric (TE) and transverse magnetic (TM) modes.

We impose the following continuity conditions at the boundary between the two half spaces, $z = 0$,

$$\hat{z} \times \left[\mathfrak{G}^{(11)}(\mathbf{r}, \mathbf{s}, \omega) - \mathfrak{G}^{(21)}(\mathbf{r}, \mathbf{s}, \omega) \right]_{z=0} = 0, \tag{5.5}$$

$$\hat{z} \times \left[\nabla \times \mathfrak{G}^{(11)}(\mathbf{r}, \mathbf{s}, \omega) - \nabla \times \mathfrak{G}^{(21)}(\mathbf{r}, \mathbf{s}, \omega) \right]_{z=0} = -i \frac{4\pi}{c} k_0 \sigma \hat{z} \times \hat{z} \times \mathfrak{G}^{(21)}(\mathbf{r}, \mathbf{s}, \omega), \tag{5.6}$$

where σ is the surface conductivity of the GM.

Using Eqs. (5.3)-(5.4) in (5.5)-(5.6) we obtain the generalized Fresnel coefficients, which have the form [84, 115],

$$R_M^{11} = \frac{k_{z1} - k_{z2} - 2\alpha k_0}{k_{z1} + k_{z2} + 2\alpha k_0}, \quad R_N^{11} = \frac{k_2^2 k_{z1} - k_1^2 k_{z2} + 2\alpha k_0 k_{z1} k_{z2}}{k_2^2 k_{z1} + k_1^2 k_{z2} + 2\alpha k_0 k_{z1} k_{z2}} \tag{5.7}$$

$$R_M^{21} = \frac{2k_{z1}}{k_{z1} + k_{z2} + 2\alpha k_0}, \quad R_N^{21} = \frac{2k_1 k_2 k_{z1}}{k_2^2 k_{z1} + k_1^2 k_{z2} + 2\alpha k_0 k_{z1} k_{z2}}, \tag{5.8}$$

where $\alpha = 2\pi\sigma/c$. In this chapter we focus in the case of a free standing graphene monolayer, thus $\varepsilon_1 = \varepsilon_2 = 1$.

5.2.2 Graphene conductivity and graphene plasmon properties

The graphene in-plane conductivity, σ, is calculated using the random phase approximation (RPA) [131, 132, 157]. This quantity is mainly controlled by electron-hole pair excitation that can be divided into intraband and interband excitations. It can be written as

$$\sigma = \sigma_{\text{intra}} + \sigma_{\text{inter}}, \tag{5.9}$$

where the intraband and interband contributions are,

$$\sigma_{\text{intra}} = \frac{2ie^2 t}{\hbar\pi(\Omega + i\gamma)} \ln\left[2\cosh\left(\frac{1}{2t} \right) \right], \tag{5.10}$$

$$\sigma_{\text{inter}} = \frac{e^2}{4\hbar} \left[\frac{1}{2} + \frac{1}{\pi} \arctan\left(\frac{\Omega - 2}{2t} \right) - \frac{i}{2\pi} \ln \frac{(\Omega + 2)^2}{(\Omega - 2)^2 + (2t)^2} \right]. \tag{5.11}$$

In the above the dimensionless parameters $\Omega = \hbar\omega/\mu$, $\gamma = E_S/\mu$ and $t = k_B T/\mu$ are introduced. Here, μ is the chemical potential, T is the temperature, and E_S is the scattering energy. This scattering energy is related to the relaxation time τ through $\tau = \hbar/E_S$. In Fig. (5.1b) the

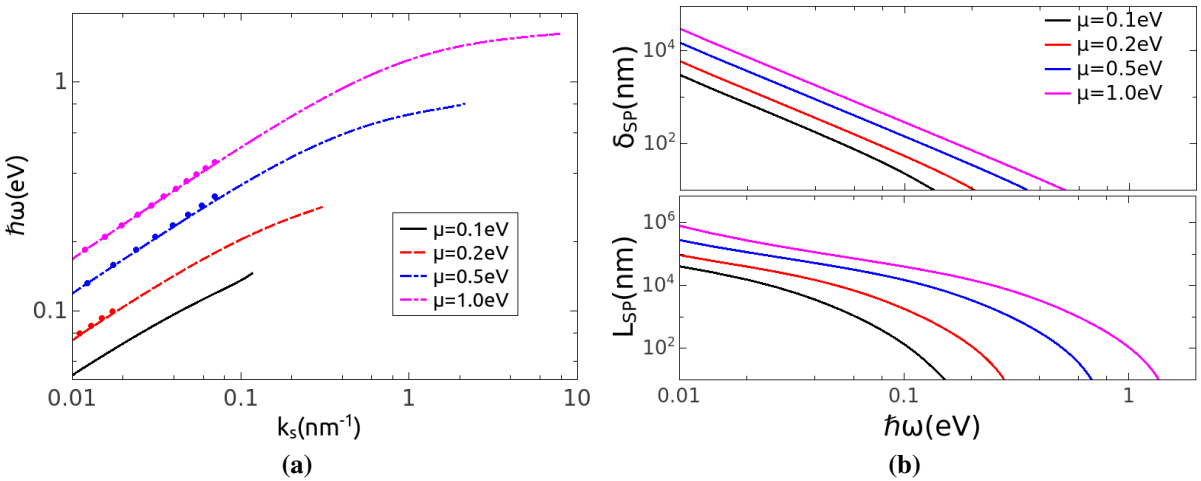

Figure 5.2: *(a) Surface plasmon dispersion relation in doped graphene, $\omega(k_s)$, for different values of the chemical potential μ; the dots show the quadratic approximation of the dispersion relation. (b) (Up) Penetration depth, δ_{SP}, and propagation length, L_{SP}, of the GP mode for different values of the chemical potential, μ.*

expression $\alpha = 2\pi\sigma/c$ is plotted in units of the fine structure constant, α_0, for different values of the chemical potential, μ. The σ_{intra} term describes a Drude model response for intraband processes corrected with a term γ, accounting for impurities, which compromise the electron's mobility. Throughout this chapter a temperature $T = 300\,\text{K}$ and a value of the relaxation time of $\tau = 1\,\text{ps}$ are considered [158, 159]. Fig. 5.2a shows the dispersion relation, $\omega(k_s)$ where k_s is the in-plane wavevector, for different values of the chemical potential, μ. Due to the fact that retardation effects dominate for wavevectors $k_s > k_F$ and for energies $\hbar\omega > 2\mu$, the GP dispersion curves in Fig. 5.2a terminate at these values, where k_F is the Fermi wavevector, $k_F = E_F/\hbar c$. When the chemical potential, μ, has the value $\mu = 0$, the GM absorbance has the value $\pi\alpha_0 \approx 2.3\%$, where α_0 is the fine structure constant. This is the asymptotic value of the doped GM for energies $\hbar\omega > 2\mu$. Considering that the GM is surrounded by air, $\varepsilon_1 = \varepsilon_2 = 1$ (free standing GM), the GP dispersion relation can be obtained from:

$$\frac{1}{\sqrt{k_0^2 - k_{SP}^2}} = -\frac{2\pi\sigma}{\omega}, \tag{5.12}$$

where k_{SP} is the GP wavevector [81]. Because $k_{SP} \gg k_0$, the dispersion relation above can be simplified, using only the σ_{intra} contribution, to obtain

$$k_{SP} = \frac{\hbar^2}{4e^2\mu k_B T \ln\left[2\cosh\left(\frac{\mu}{k_B T}\right)\right]}\omega\left(\omega + \frac{i}{\tau}\right), \tag{5.13}$$

which has as its main feature the quadratic dependence of the GP wavevector on the frequency, when the intraband contributions dominate [132]. This approximate quadratic dependence is shown as dots in Fig. 5.2a. Another feature of the GP dispersion relation on graphene is the fact that the GP resonance frequency is blue-shifted as the chemical potential increases.

Fig. 5.2b shows the penetration depth, $\delta_{\rm SP} = 1/{\rm Im}(k_z^{\rm SP})$, and the propagation length , $L_{\rm SP} = 1/{\rm Im}(k_{\rm s})$, of the surface plasmon along the graphene as a function of energy, for different values of the chemical potential, μ. It is evident from the plot that, depending on the value of the chemical potential, μ, the penetration and propagation lengths can reach values as large as tens of microns at low frequencies. As the energy is increased, however, the lengths decrease rapidly, because the GP then has sufficient energy to generate electron-hole pairs and the dispersion relation is dominated by the interband contributions [72].

5.2.3 Rabi splitting - strong coupling regime

The quantum emitters considered in this thesis have well defined transitions between their electronic levels. In Sec. 2.3.1 it is shown that the spontaneous emission rate is altered by its environment. When the interaction between the emitter and its environment does not alter the emission frequency, but only its spontaneous emission, then the combined system QE+environment operates under the weak coupling regime. The strong coupling regime, on the other hand is accessed when the energy levels, of the quantum emitter, are altered by the modes provided by their the local environment. As environment in this chapter the gated graphene monolayer is considered and the mode provided is the graphene SP mode.

In order to ascertain whether the weak or the strong coupling (SC) regime applies for particular sets of parameters, a model consisting of a single QE interacting with the GP mode of the GM is considered. To describe this system, a Jaynes-Cummings Hamiltonian is used [160], that has the form:

$$H = \frac{\hbar\omega}{2}\sigma_z + \hbar\omega_{\rm SP}\hat{a}^\dagger\hat{a} + \hbar g(\hat{a}\sigma_+ + \hat{a}^\dagger\sigma_-), \tag{5.14}$$

where $\omega_{\rm SP}$ is the GP frequency, $\hat{a}^\dagger$ and $\hat{a}$ are the creation and annihilation operators of the plasmon mode, ω is the transition frequency of the QE between its ground and excited state, σ_+ and σ_- are the raising and lowering operators of the QE, and g is the coupling constant between the QE and the GP mode of the GM. The coupling constant g is given by [161]

$$\begin{aligned} |g(\omega)|^2 =& \frac{1}{\hbar\pi\varepsilon_0}\frac{\omega^2}{c^2}\hat{\mathbf{d}}^T {\rm Im}\mathfrak{G}_{\rm SP}(\omega, \mathbf{r}_{\rm QE}, \mathbf{r}_{\rm QE})\hat{\mathbf{d}} \\ =& \gamma_0\frac{3c}{\omega}\hat{\mathbf{d}}^T {\rm Im}\mathfrak{G}_{\rm SP}(\omega, \mathbf{r}_{\rm QE}, \mathbf{r}_{\rm QE})\hat{\mathbf{d}}, \end{aligned} \tag{5.15}$$

where $\mathfrak{G}_{\mathrm{SP}}(\omega, \mathbf{r}_{\mathrm{QE}}, \mathbf{r}_{\mathrm{QE}})$ is the GP part of the Green's tensor, derived in Sec. 5.2.1, Eq. (5.3), γ_0 is the Einstein A-coefficient, $\gamma_0 = \omega^3 d^2/(3\pi\hbar\varepsilon_0 c^3)$ and $\mathbf{d}$ is the transition dipole moment of the QE positioned at $\mathbf{r}_{\mathrm{QE}} = (0,0,z)$. In this section, we consider $\gamma_0 = 5\times10^{-8}\,\mathrm{fs}^{-1}$. Since the focus is in the coupling between the GP mode and the QE the GP contribution to Eq. (5.3) is calculated, by extracting the pole contribution and it is obtained as

$$\mathfrak{G}^{(11)\mathrm{SP}}_{\mathrm{S},zz}(z,\omega) = -\frac{1}{4}\frac{\left(1-1/\alpha^2\right)}{\alpha k_0}\mathrm{e}^{-2iz/\alpha}, \tag{5.16}$$

where $\alpha = 2\pi\sigma/c$.

The Hamiltonian from Eq. (5.14) couples the states $|e\rangle\otimes|0\rangle$ and $|g\rangle\otimes|1\rangle$ to the dressed states $|1\rangle$ and $|2\rangle$ with energies,

$$E_{1,2} = \frac{\hbar\omega_{\mathrm{SP}}}{2} \mp \frac{\hbar}{2}\sqrt{\delta^2+4g^2}, \tag{5.17}$$

where $\delta = \omega_{\mathrm{SP}} - \omega$, is the detuning between the GP mode resonant frequency and the transition frequency of the QE. The energy states are separated by $\Omega = \sqrt{\delta^2+4g^2}$, which gives the value of the Rabi splitting. As an example, if the QE is positioned at $z = 10\,\mathrm{nm}$ above a GM with a chemical potential equal to the transition energy of the QE, $\mu = \hbar\omega = 0.5\,\mathrm{eV}$, the Rabi splitting, at $\delta = 0$, has a value $2g(\omega) = 0.12\,\mathrm{eV}$.

In order to further investigate the weak and strong coupling regimes, the dependence of the coupling constant, g, on the various parameters involved, namely the value of the chemical potential, μ, the emission frequency of the QE, ω, and the distance of the QE to the GM, z, is analyzed. Considering $\omega = \omega_{\mathrm{SP}}$, i.e. zero detuning, the criterion for having strong coupling is whether or not the absorption spectrum of the system exhibits two peaks of different frequencies [161, 162]. This condition is fulfilled if

$$|g| > \frac{1}{4}\left|\gamma_{\mathrm{LSW}} - \kappa\right|, \tag{5.18}$$

where γ_{LSW} represents the *lossy surface waves* (LSW) contribution, which are non-propagating evanescent modes relaxing through Ohmic losses, and κ is the width of the $|g(\omega)|^2$ spectrum.

In Fig. 5.3a a contour plot of the quantity $\mathfrak{D} = 4|g|/|\gamma_{LSW} - \kappa|$ is presented, as a function of the chemical potential, μ, and the emission energy, $\hbar\omega$, for a fixed position of the QE, $z = 10\,\mathrm{nm}$. Although from condition (5.18) when $\mathfrak{D} < 1$ the weak coupling regime is exhibited, this condition might not be sufficient under some experimental conditions [160], and thus we consider the more stringent inequality $\mathfrak{D} \lesssim 0.5$ as giving the weak coupling condition. As is evident from Fig. 5.3a, for chemical potential values $\mu < 0.3\,\mathrm{eV}$, there exists a frequency

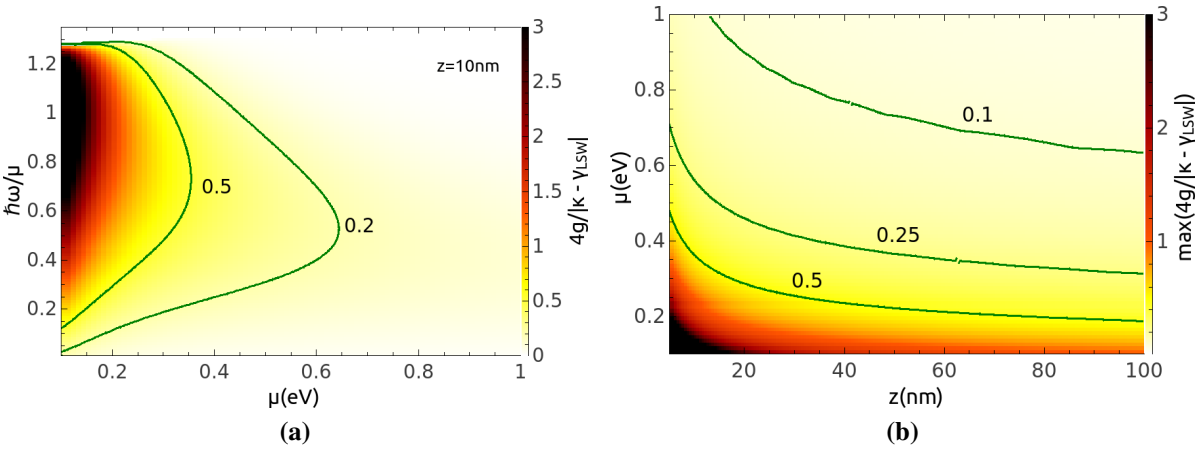

Figure 5.3: *Contour plots of the quantity* $\mathfrak{D} = 4|g|/|\gamma_{LSW} - \kappa|$ *as a function of (a) chemical potential,* μ*, and emission energy,* $\hbar\omega$*, for fixed QE position* $z = 10\,nm$*, (b) chemical potential,* μ*, and QE position, z; each point reflects the maximum value of* $\mathfrak{D}(\omega)$*.*

region where we have $\mathfrak{D} \geq 0.5$ and the weak coupling that will be used to calculate the SE and ET rates would no longer be valid. This region where the strong coupling dominates corresponds to THz frequencies, a range outside the scope of this investigation. For chemical potential values $\mu > 0.6\,eV$, on the other hand, the quantity $\mathfrak{D}$ has values below 0.2 well within the weak-coupling regime.

Figure 5.3b examines the maximum value of $\mathfrak{D}$ for different values of the chemical potential, μ, and at different positions of the QE above the GM. For each point, the maximum value of $\mathfrak{D}$ is calculated as a function of the emission energy of the QE, $\hbar\omega$. This represents, therefore, the worst-case scenario for weak coupling, since at all other frequencies, $\mathfrak{D}$ will be smaller than the values depicted in Fig. 5.3b. It can be seen that the strong coupling regime is only accessed for values $\mu < 0.4\,eV$ at certain frequencies. Throughout the rest of the chapter we only consider frequency ranges which remain outside the SC regime for all values of μ and g explored.

5.3 Results and Discussion

5.3.1 Spontaneous emission rate

As is discussed in Sec. 2.3.1, the decay rate, γ, is proportional to the strength of the coupling between the transition dipole matrix element and the electromagnetic modes acting on it. The

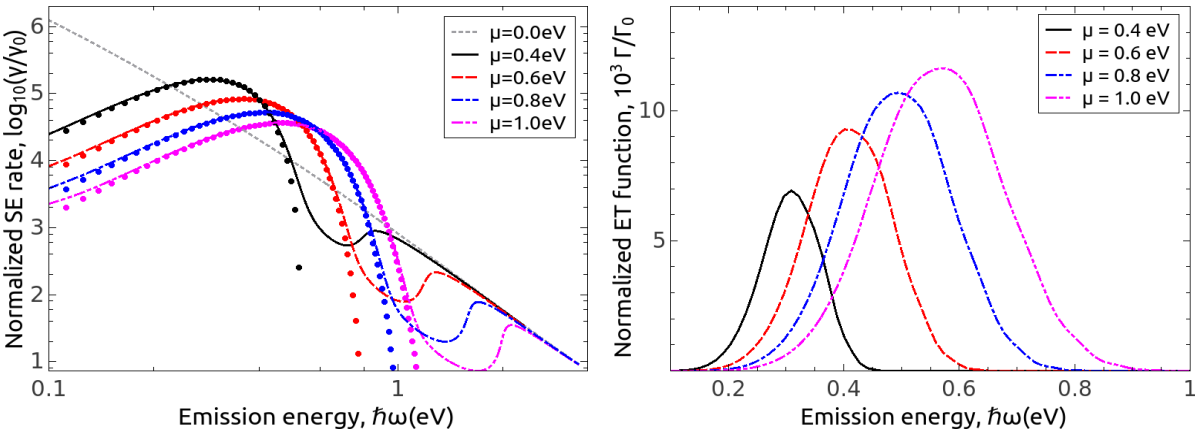

Figure 5.4: *(a) SE rate of a QE, positioned at* $\mathbf{r} = (0,0,10\,nm)$*, as a function of its emission frequency for different values of the chemical potential,* μ*. (b) Normalized ET function,* $\tilde{\Gamma}(\mathbf{r}_A, \mathbf{r}_D, \omega)$*, between a donor and acceptor QE as a function of frequency, for fixed donor and acceptor positions,* $\mathbf{r}_D = (0,0,10\,nm)$ *and* $\mathbf{r}_A = (100\,nm, 0, 10\,nm)$ *respectively, and different values of the chemical potential,* μ*.*

normalized SE is given by Eq. (2.28), for completeness the expression is given again [59],

$$\tilde{\gamma} = \frac{\gamma}{\gamma_0} = n_i + \frac{6\pi c}{\omega} \mathrm{Im}\left[\mathbf{n}_{\mathrm{QE}} \cdot \mathfrak{G}_{\mathrm{s}}(\mathbf{r}, \mathbf{r}, \omega) \cdot \mathbf{n}_{\mathrm{QE}}\right], \tag{5.19}$$

where γ_0 is Einstein's A-coefficient, $\mathbf{n}_{\mathrm{QE}}$ is a unit vector along the direction of the transition dipole moment of the emitter, and $\mathfrak{G}(\mathbf{r}, \mathbf{r}, \omega)$ is given by (5.3).

In Fig. 5.4a the normalized SE rate, $\tilde{\gamma}$, of a QE is plotted for a fixed position, $\mathbf{r} = (0,0,10\,\mathrm{nm})$ above the GM, as a function of the QE's emission energy, $\hbar\omega$, for different values of the chemical potential, μ. In general the SE rate has a peak at an energy below μ. As the energy is further increased, the SE rate drops dramatically before finally recovering to a value independent of μ, typically occurring when the energy is above 2μ. As the value of μ is increased the GP peak blue-shifts, broadens, and has a lower value. The general drop in the SE rate is most visible starting with values of the chemical potential of $\mu > 0.4\,\mathrm{eV}$, and it occurs between the energies $\hbar\omega = \mu$ and $\hbar\omega = 2\mu$. This drop is due to interband transitions when the QE relaxes through lossy channels. At emission energies $\hbar\omega > 2\mu$ the emission is determined by interband contributions and GP excitations become unimportant, as the dispersion relations in Fig. 5.2a show. At these energies the SE rate follows the same behavior as for the case of undoped graphene, $\mu = 0$ eV, also shown in Fig. 5.4a. Moreover, it can be seen that the main contribution to the peak in the normalized SE rate, $\tilde{\gamma}$, comes from the GP contribution, which is denoted by the circular symbols in Fig. 5.4a. The maximum value of $\mathfrak{D}$ is 0.41 at $\mu = 0.4\,\mathrm{eV}$, thus placing us within the weak coupling regime.

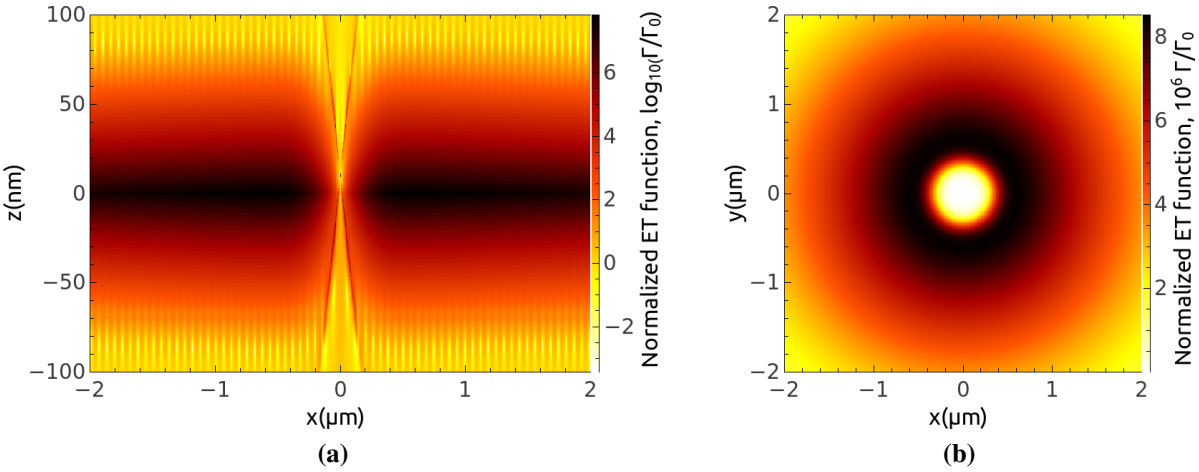

Figure 5.5: *Contour plots of the normalized ET function, in the (a) xz-plane and (b) xy-plane when $z = 10\,nm$, for a donor positioned at $\mathbf{r}_D = (0,0,10\,nm)$ above a GM. The dielectric permitivitty of the surrounding media is $\varepsilon_1 = \varepsilon_2 = 1$. The chemical potential of the graphene monolayer is $\mu = 1.0\,eV$. The emission frequency of the donor is $\omega = 0.8\,fs^{-1}$ ($\lambda = 2.3\,\mu m$). Both donor and accceptor have their transition dipole moments oriented along the z-axis.*

5.3.2 Energy transfer function

In this section the influence of the GM on the energy transfer process between a pair of QEs, a donor and an acceptor, is investigated. The normalized energy transfer function is investigated, which has been introduced in Sec. 2.3.2 and is given by Eq. (2.35).

Figure 5.4b shows the normalized energy transfer function, $\tilde{\Gamma}$, as a function of frequency for different values of the chemical potential, μ, and when both the donor and acceptor transition dipole moments are oriented perpendicular to the GM, i.e. *zz*-orientation. The donor and acceptor positions are fixed at $\mathbf{r}_\mathrm{D} = (0,0,10\,\mathrm{nm})$ and $\mathbf{r}_\mathrm{A} = (100\,\mathrm{nm},0,10\,\mathrm{nm})$, respectively. As for the case of the SE rate in 5.4a, the normalized ET function, $\tilde{\Gamma}$, is enhanced close to the GP frequency and in general for frequencies $\hbar\omega < \mu$, where the intraband transitions dominate. For frequencies $\hbar\omega > \mu$ the energy transfer rate decreases due to the losses generated by the interband contributions.

Figure 5.5 presents contour plots of the normalized ET function, $\tilde{\Gamma}$, as a function of the position of the acceptor in (a) the *xz*-plane and (b) the *xy*-plane 10 nm above the GM, when the donor position is fixed at $\mathbf{r}_\mathrm{D} = (0,0,10\,\mathrm{nm})$, the transition energy is $\hbar\omega = 0.52\,\mathrm{eV}$ ($\lambda = 2.3\,\mu\mathrm{m}$) and the chemical potential is $\mu = 1.0\,\mathrm{eV}$. In Fig. 5.5a the normalized ET function has large values when the acceptor is close to the GM and decreases as the acceptor distance is increased. This behavior is due to the fact that the field is highly confined in the z-direction at the surface of the GM, with a penetration depth of $\delta_\mathrm{SP} = 10\,\mathrm{nm}$, or $\delta_\mathrm{SP}/\lambda = 4\cdot 10^{-3}$. The

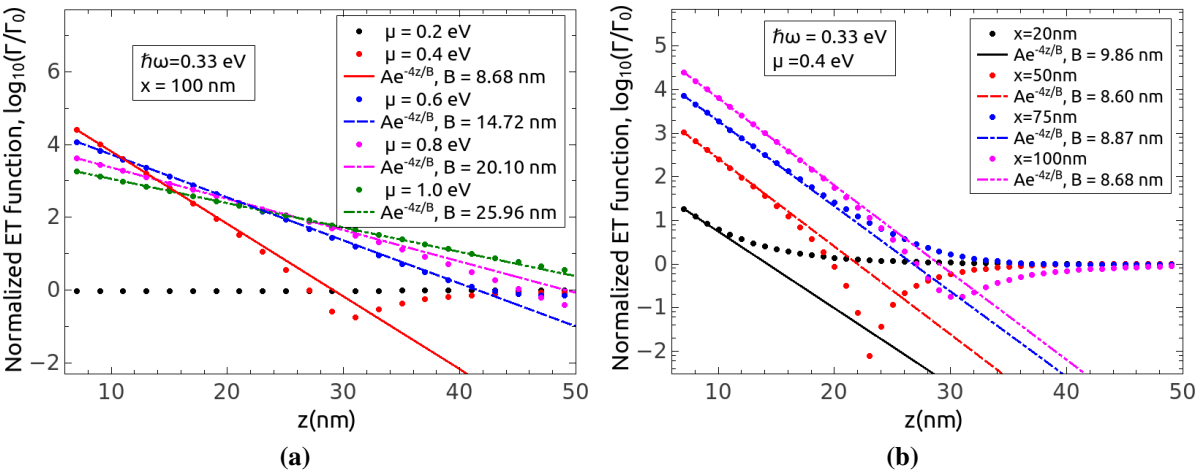

Figure 5.6: *Normalized ET function, $\tilde{\Gamma}(\mathbf{r},\mathbf{s},\omega)$, as a function of the donor and acceptor distance to the graphene monolayer, for a fixed transition energy, $\hbar\omega = 0.33\,eV$. (a) For various values of the chemical potential, μ, when the donor position is $\mathbf{r}_D = (0,0,z)$ and the acceptor position is $\mathbf{r}_A = (100\,nm,0,z)$; (b) For various in-plane distances, x, when the donor position is $\mathbf{r}_D = (0,0,z)$ and the acceptor position is $\mathbf{r}_A = (x,0,z)$, for a fixed value of the chemical potential, $\mu = 0.4\,eV$. The symbols represent the full simulation data, while the lines are fits with the exponential function in the legend. Both donor and acceptor have their transition dipole moments oriented along the z-axis.*

fringes visible in Fig. 5.5a are due to the constructive and destructive interference between the direct and scattering terms in the Green's tensor, see Eq. (5.1). This effect is more profound due to the dipole moment orientations of the QEs, along the z-axis. Fig. 5.5b shows that the normalized ET function has cylindrical symmetry in the xy-plane, due to the orientation of both donor and acceptor transition dipole moments along the z-axis. Furthermore, the normalized ET function has a peak value at a distance of about 400 nm, which is the propagation length of the GP mode for the particular set of parameters used in this calculation.

In Fig. 5.6a the z-dependence of the normalized ET function, $\tilde{\Gamma}$, is presented for a donor located at $\mathbf{r}_\mathrm{D} = (0,0,z)$ and an acceptor at $\mathbf{r}_\mathrm{A} = (100\,\mathrm{nm},0,z)$, for various values of the chemical potential, and a fixed transition energy, $\hbar\omega = 0.33\,\mathrm{eV}$. As has already been pointed out, for different values of the chemical potential, μ, the position of the maximum in the normalized ET function blueshifts as the value of the chemical potential is increased, cf. Fig. 5.4b. Thus, for the smallest value of the chemical potential, $\mu = 0.2\,\mathrm{eV}$, the enhancement of the ET function is negligible to non-existent. As the value of the chemical potential is increased, the ET function has values a few orders of magnitude larger than in free-space when the donor-acceptor pair is close to the GM. As the donor-acceptor pair is moved further from the GM – increasing z – the ET function drops off exponentially, as the figure shows. The continuous lines in Fig. 5.6a represent fits of the calculated ET function (represented by symbols) with

Table 5.1: *Graphene plasmon penetration depths.*

$\hbar\omega$ (eV)	μ (eV)	δ_{SP} (nm)	B_{SE} (nm)	B_{ET} (nm)
0.33	0.4	8.2	8.50	8.68
0.33	0.6	14.06	14.38	14.72
0.33	0.8	19.48	20.04	20.10
0.33	1.0	24.76	25.47	25.96

the exponential function $Ae^{-4z/B}$. The factor 4 in this expression has two sources: (i) the z distance of both donor and acceptor to the GM is varied and (ii) the ET function depends on the square of the field, see Eq. 2.35; each of these gives a doubling of the exponent, for a total of $2 \times 2 = 4$. Furthermore, because the donor-acceptor separation is kept constant at $x = 100\,\text{nm}$, the free-space ET function is also constant and, hence, does not influence the exponential behavior. Table 5.1 shows the values of the parameter B_{ET} extracted from the fit, together with the analogous parameter B_{SE} extracted from fitting the SE dependence (the numerical factor in the exponent is 2 in this case, rather than 4, due to the fact that the SE rate depends linearly on the electric field; data not shown) and the penetration depth of the GP in the air above the graphene, calculated as $\delta_{SP} = 1/\text{Im}\left(k_z^{SP}\right)$. As this table shows, the values of the parameters B_{SE} and B_{ET} match closely with the calculated penetration depths of the GPs. This suggests that the main channel for enhancing the ET function between the QEs is the GP resonance. As the separation between the two QEs becomes smaller and smaller, this relaxation channel becomes less and less important and the direct interaction dominates at distances below $x = 20\,\text{nm}$, as panel 5.6b shows. In this panel the influence of the in-plane distance between the donor and acceptor is investigated, for a fixed value of the chemical potential, $\mu = 0.4\,\text{eV}$ and fixed transition energy, $\hbar\omega = 0.33\,\text{eV}$. The calculated ET function data (symbols) are fitted with the expression $Ae^{-4z/B}$. As one can see, above $x = 50\,\text{nm}$ the B_{ET} parameter extracted is very close to the penetration depth of the GP, δ_{SP}. When the donor and acceptor in-plane distance is smaller than $x = 50\,\text{nm}$, the influence of the GP mode on the ET function is less profound, and, as the donor-acceptor pair is moved away from the GM, it recovers its free-space interaction at shorter distances. This is due to the fact that the influence of the homogeneous part of the Green's tensor dominates over the scattered part, see Eq. 5.1; this effect will be further discussed in Sec. 5.3.3. In this section the quantity $\mathfrak{D}$ has the largest value of 0.48 for $\mu = 0.4\,\text{eV}$, $\hbar\omega = 0.33\,\text{eV}$ at a donor-GM distance of 8 nm, ensuring that the system is in the weak coupling regime.

5.3.3 Energy transfer efficiency

In Sec. 5.1 and 5.2 the SE and ET rates have been investigated, respectively, which will now be used to study the energy transfer efficiency. Now, using a similar approach to the one developed when the dielectric coated cylinder geometry was discussed in Sec. 4.3.3, when the donor dipole is excited it has two ways of relaxing to the ground state: it can either transfer its excitation energy to the acceptor dipole with an ET rate k_{ET}, or it can relax with decay rate k_{SE}, where it is assumed that there is no intrinsic non-radiative decay, i.e. the intrinsic quantum yield of the donor is $Y_0 = 1$. The decay rate k_{SE} takes account of photon emission into the far-field, coupling to GP modes and losses in the GM. The SE and ET processes are, therefore, in competition with each other and an energy transfer efficiency is introduced to describe this competition.

The energy transfer efficiency η is given by Eq. 2.37. This quantity gives the relative contribution of the energy transfer process to the total decay rate of the donor. If the ET efficiency, η, has a value $\eta > 50\%$, then the decay of the excited state of the donor occurs mainly by energy transfer to the acceptor, rather than relaxation into photon or GP modes.

Considering a donor-acceptor pair, the donor emission and acceptor absorption spectra are both given by a Gaussian distribution, Eq. (6.54), and have the form:

$$A_{\mathrm{q}}\, \mathrm{e}^{-(\lambda-\lambda_{\mathrm{q}})^2/\Delta\lambda_{\mathrm{q}}^2}, \tag{5.20}$$

where $\mathrm{q} = D$ represents the donor and $\mathrm{q} = A$ represents the acceptor. The properties of the spectra describing the donor emission and acceptor absorption cross section are identical with the ones used in Sec. 4.3.3. The only difference is that the donor emission peak and acceptor absorption maximum coincide at $\lambda_{\mathrm{D}} = \lambda_{\mathrm{A}} = 2\ \mu$m. There are a variety of emitters at this wavelength, such as quantum dots and synthesized molecules [163, 164].

The Förster radius, R_0, is defined as the donor-acceptor separation at which the energy transfer efficiency, η, is 50%. The Förster radius can be calculated from the spectral overlap and has a value of 19 nm in free-space. R_0 is calculated from the spectral overlap of the normalized donor emission, f_{D}, and acceptor absorption, σ_{A}, spectra using Eq. (2.40).

In Fig. 5.7 contour plots of the ET efficiency are presented for the donor-acceptor pair, with spectral properties described above; the donor and acceptor positions are fixed at $\mathbf{r}_{\mathrm{D}} = (0, 0, 10\,\mathrm{nm})$, and $\mathbf{r}_{\mathrm{A}} = (x, 0, z)$, respectively. Two values of the chemical potential are considered $\mu = 1.0$ eV, Fig. (5.7a), and $\mu = 0.6$ eV, Fig. (5.7b). When $\mu = 1.0\,$eV the emission and absorption spectrum overlap strongly with the ET function. For this case the ET efficiency, η, has values above 70% even for separations along the GM as large as 100 nm, and the 50%

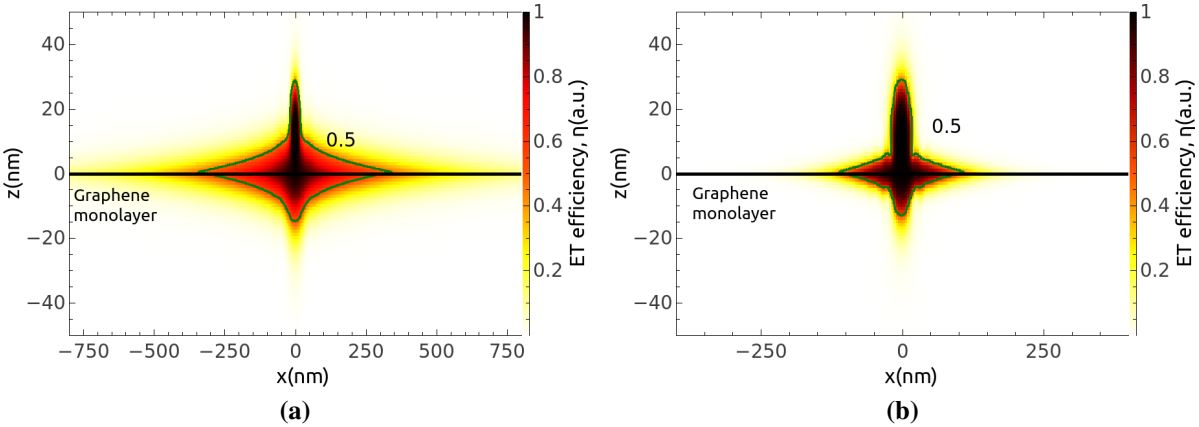

Figure 5.7: *Contour plot of the ET efficiency, η, between a pair of QEs, as a function of acceptor position for a fixed position of the donor at $\mathbf{r}_D = (0,0,10\,nm)$ and different values of the chemical potential, (a) $\mu = 1\,eV$ and (b) $\mu = 0.6\,eV$. The green line gives the $\eta = 50\%$ values.*

efficiency distance is around 300 nm. This value is very large compared to the free-space Förster radius of $R_0 = 19$ nm. When the value of the chemical potential is $\mu = 0.6$ eV, the ET efficiency, η, has values above 50 % for separations above 100 nm but now the overlap between the emission and absorption spectra and the ET function is reduced, thus showing a diminished effect. The large confinement of light at the atomically thin GM surface can be used to efficiently transfer energy between a pair of QEs over large separations. Furthermore, this ET efficiency, η, can be controlled through gating of the GM, thus opening striking opportunities for possible applications, such as switching and sensing devices [79, 153, 154], light harvesting [155], plasmonic rulers [79, 156] and quantum computing [85].

The behavior of the ET rate, k_{ET}, is investigated as a function of the in-plane separation between donor and acceptor. Figs. 5.8a and 5.8b show the ET rate, k_{ET}, as a function of the in-plane distance between the donor and acceptor, when their elevation above the GM is (a) $z = 5$ nm and (b) $z = 10$ nm on the same side of the GM. For both panels, the near field is fitted with a Förster-type model, $(R_0/x)^n$, where R_0 is the Förster radius. At small separations the fit yields the values $n = 6$ and the Förster radius is modified from the free-space value, $R_0 = 19$ nm. The fact that at small separations, $x < 10$ nm, for $z_{\mathrm{D}} = z_{\mathrm{A}} = 5$ nm and $x < 20$ nm, for $z_{\mathrm{D}} = z_{\mathrm{A}} = 10$ nm, the ET rate, k_{ET}, follows an $n = 6$ dependence shows that the homogeneous part of the Green's tensor dominates, see Eq. (5.1), modified by the donor-acceptor interaction with the GM. Thus, there is an enhancement of the Förster radius, which depends on the donor-acceptor distances from the GM and the value of the chemical potential, μ. In Fig. 5.8a the Förster radius has values of $R_0 = 123$ nm for chemical potential values $\mu = 0.8$ eV and $\mu = 1.0$ eV. As the chemical potential value drops, the Förster radius

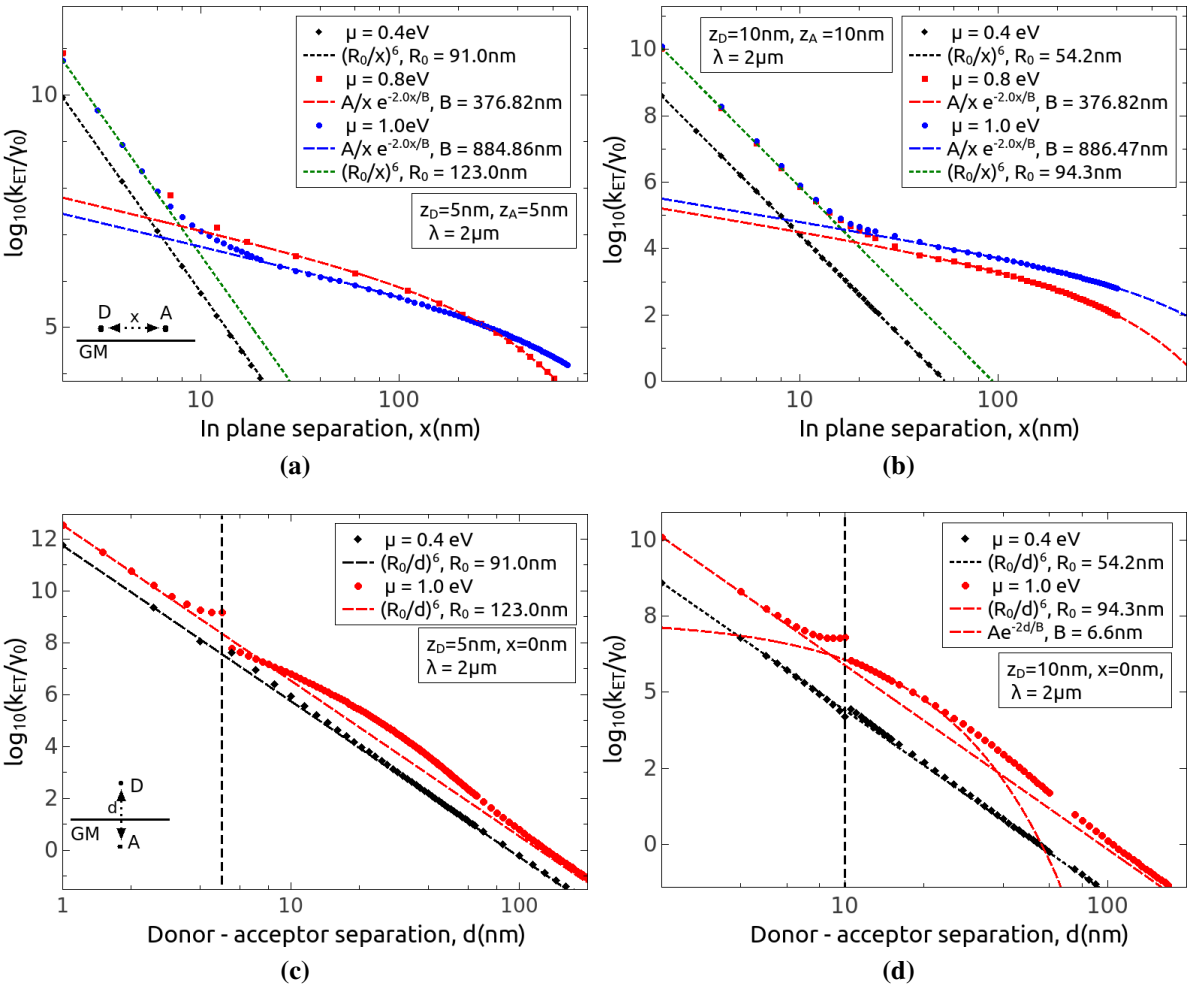

Figure 5.8: *(a-b) ET rate, k_{ET}, as a function of the donor-acceptor in-plane separation, x, for fixed donor positions, (a) $\mathbf{r}_D = (0,0,5\,nm)$ and (b) $\mathbf{r}_D = (0,0,10\,nm)$ respectively, and variable acceptor position, $\mathbf{r}_A = (x,0,5\,nm)$ and $\mathbf{r}_A = (x,0,10\,nm)$ respectively, for different values of the chemical potential, μ. (c-d) ET rate, k_{ET}, as a function of the donor-acceptor separation, d, for fixed donor positions, (c) $\mathbf{r}_D = (0,0,5\,nm)$ and (d) $\mathbf{r}_D = (0,0,10\,nm)$ respectively, and variable acceptor position $\mathbf{r}_A = (0,0,z_A)$, with $d = z_D - z_A$ and for different values of the chemical potential, μ.*

Table 5.2: *Graphene plasmon propagation length.*

z (nm)	μ (eV)	L_{SP} (nm)	B (nm)
5	0.8	379.23	376.82
5	1.0	890.31	884.86
10	0.8	379.23	376.99
10	1.0	890.31	886.47

decreases to $R_0 = 91\,\text{nm}$ for $\mu = 0.4\,\text{eV}$, a value that is smaller than the one for the case of an undoped graphene layer, $R_0 \approx 100\,\text{nm}$, due to interband transitions, see Fig. 5.4a. The effect of tuning the Förster radius through the chemical potential is evident. In Fig. 5.8b the values of the Förster radius are smaller for the different values of the chemical potential, μ, due to the fact the QEs-GM distance is increased. When $\mu = 1.0\,\text{eV}$ the largest value of the Förster radius is exhibited, $R_0 = 94.3\,\text{nm}$, due to the choice of the donor and acceptor. For the off-resonance case, $\mu = 0.4\,\text{eV}$, the Förster radius is $R_0 = 54\,\text{nm}$, once again smaller than the case of undoped graphene, $R_0 = 70\,\text{nm}$.

At larger donor-acceptor separations, the following expression is used to fit the calculated ET rate

$$f(x) = \frac{A}{x}\exp\left(-\frac{2x}{B}\right), \tag{5.21}$$

which represents the dependence of the GP field intensity on the in-plane distance x (the factor 2 in the exponential results from the square of the Green's tensor, as does the x in the denominator – the GP field has a factor of $1/\sqrt{x}$). The fitting parameter B is tabulated in Table 5.2, together with the corresponding propagation length of the GP along the interface of the GM, L_{SP}. As is clear, the correspondence between these parameters is very good indeed, confirming that, away from the near-field, the interaction between donor and acceptor occurs primarily through the GP excited by the donor at the surface of the GM. As the distance between the QEs and the GM is increased, the Förster regime dominates further away from the near-field, as can be seen from the fact that the intersection between the two fitting curves moves to larger distances. This is due to the small value of the penetration depth of the GP, $\delta_{SP} = 6.6\,\text{nm}$ at $\mu = 1.0\,\text{eV}$.

Figs. 5.8c and 5.8d consider the ET rate, k_{ET}, as a function of the donor-acceptor separation, for the case when the donor position is kept fixed at (5.8c) $z_D = 5\,\text{nm}$ and (5.8d) $z_D = 10\,\text{nm}$ above the GM, and the separation between the donor-acceptor, $d = z_D - z_A$ is varied, for $\mu = 1.0\,\text{eV}$ and $\mu = 0.4\,\text{eV}$. At small separations the Förster model is used for fitting, presented earlier. To fit the behavior of the ET rate, k_{ET}, below the GM the expression $f(z) = Ae^{-2z/\Delta}$ is chosen, where the parameter Δ will be connected with the penetration depth of the GP,

δ_{SP}. In both figures, the GM position is denoted by the dashed vertical line. In Fig. 5.8c, for which the donor position is very close to the GM ($z_D = 5\,\text{nm}$), the behavior of the ET rate immediately below the GM is not trivial and comes from various contributions, such as direct interaction and GP-coupling. On the other hand, in panel 5.8d, for which $z_D = 10\,\text{nm}$, we can use the fitting function $f(z_A)$, and find for Δ the value $\Delta = \delta_{SP} = 6.6\,\text{nm}$, showing that the main contribution to the ET rate comes from the GP on the GM. For the $\mu = 0.4\,\text{eV}$ case the ET rate, k_{ET}, is almost uninfluenced by the presence of the GM. The quantity $\mathfrak{D}$ has a maximum value of 0.2 for the donor-GM distance of 5 nm and $\mu = 1.0\,\text{eV}$.

5.4 Summary and Conclusions

In this chapter the behavior of quantum systems placed near a free-standing graphene monolayer has been investigated. The graphene monolayer can support graphene surface plasmon modes, tightly confined to the surface and having large propagation distances along the graphene monolayer.

The conditions of strong and weak coupling, between a quantum system and the surface plasmon mode supported by the graphene monolayer, have been investigated. For reasonably large values of the chemical potential $\mu > 0.4\,\text{eV}$ and any transition energies of the QE not in the THz regime, the weak coupling conditions are fulfilled. Quantities such as spontaneous emission and energy transfer functions are calculated. It is found that both of these quantities are enhanced, compared to their free space values, due to efficient coupling to the graphene plasmon modes.

Due to the competition of the donor-acceptor energy transfer process with other donor decay processes, an energy transfer efficiency, η, is defined and the influence of the graphene plasmons on this quantity is investigated. It is shown that the energy transfer efficiency, η, can reach values above 50% for distances up to 300 nm along the graphene monolayer. This process can be controlled by tuning the value of the chemical potential, e.g. through gating.

Finally, the ET rate, k_{ET}, is investigated varying the donor-acceptor in-plane separation and distance from the GM, for various values of the chemical potential, μ. The ET rate, when the in-plane distance between the donor and acceptor is varied, has two major contributions: the Förster-type mechanism which dominates at small separations, while the GP contribution is found to dominate at large distances. The Förster-type ET rate follows an x^{-6} dependence, with an increased Förster radius value, due to the presence of the GM. The Förster radius value is increased from a value of $R_0 = 91\,\text{nm}$ when $\mu = 0.4\,\text{eV}$ to $R_0 = 123\,\text{nm}$ when $z_D = z_A = 5\,\text{nm}$ and $\mu = 1.0\,\text{eV}$. At larger distances, the main contribution comes from the GP propagation; the

transition from the Förster to the GP-propagation mechanism depends on the distance of the donor-acceptor pair from the GM, and it occurs at donor-acceptor separations ranging from a few nm to tens of nm. When the z-distance between donor-acceptor is varied, for $x = 0$, the behavior is somewhat more complicated, but the GP penetration depth still dictates the interaction length. As the chemical potential, μ, decreases the ET rate approaches the value for the case of undoped graphene.

An application for sensing using the main benefit provided by the graphene monolayer, its tunability, can be envisioned. Drop casting a layer of different species of quantum emitters, thus different spectral properties, on top of a conducting monolayer they will operate as donors. Bringing the full structure in proximity to an other set of different species of acceptors quantum emitters will then resulting in an interaction between donor and acceptor quantum emitters. Tuning the chemical potential of the graphene monolayer the interaction between them can be switched -on and -off. Thus indirectly determine the spectral properties of the acceptors and the distance between donors and acceptors.

In this chapter a gated graphene monolayer is used to facilitate long range, tunable, interaction between a pair of quantum emitters using the propagating SP mode provided. Confining the light in an infinitely thin two-dimensional material, graphene, the interaction between quantum emitters is increased to unreachable distances compared with the case where bulk nanostructures used. Confining the light in all three dimensions can further enhance the SE rate as is discussed in Sec. 1.1. In the next chapter the SP modes provided by a graphene nanodisk are used to enhance the interaction distance, perpendicularly to the disk, between quantum emitters.

Chapter 6

Tunable and long range energy transfer efficiency through a graphene nanodisk

6.1 Introduction

In the previous chapters, the interaction between quantum emitters in the presence of extended conducting, metallic and graphene nanostructures was considered. Moving from the infinite planar metallic layer geometries, Chapter 3, to the dielectric coated metallic cylinder geometry, Chapter 4, one observes an enhancement of the interaction between a pair of quantum emitters in their presence. It is well known that decreasing the dimensionality of the nanostructures, their interactions with quantum emitters are increased, see Sec. 1.1 and the discussion there. Furthermore, in Chapter 5 the interaction between quantum emitters can be significantly increased and tuned by a gated graphene monolayer. In this chapter the interaction between quantum emitters in the presence of a gated graphene nanodisk is considered. A graphene nanodisk confines the light in all three dimensions and its surface plasmon resonances are localized.

Graphene nanodisk structures have been investigated in depth over the last few years. Here is repeated, for completeness, the discussion developed in Sec. 1.1. Electrically gated patterned graphene nanostructures [19, 116], nanodisks and nanorings, interact strongly with the incoming light and the confinement parameter is large compared with the radius of these nanostructures, $\lambda^3/R^3 \gg 1$. A patterned array of graphene nanodisks has been predicted to provide 100% absorption [89]. Similar predictions have been made concerning a photonic crystal consisting of nanoholes patterned in a graphene substrate in the near infrared optical regime [117]. Furthermore, a graphene sheet decorated with small metallic nanoparticles, with zero chemical potential, can support strong absorption [118]. These interactions have been

predicted to be blue-shifted when considering more layers of graphene nanodisks instead of a single nanodisk [119,120]. Edge states and an applied magnetic potential can further influence the response of these nanostructures [114,121]. Further quantum effects have been considered in the regime where non-linear effects emerge in the coupled quantum emitter-graphene nanodisk system [122, 123].

In this chapter the SE of a single quantum emitter and the ET function between a pair of quantum emitters are investigated in the presence of a graphene nanodisk. An electrostatic method developed in Ref. [165], and used recently in Ref. [86], and expanded here, is used to calculate an electrostatic approximation of the Green's tensor. This approximation works well for the near field distances used in our calculations, provided that the graphene nanodisk radius is large enough such that quantum effects are unimportant [112], but small compared with the emission wavelength of the QEs. Using this semianalytical method the dependence of the SE and ET rates and the ET efficiency on the separations between the quantum emitters and the graphene nanodisk is studied, which is of significant importance when considering experiments such as in Refs. [79, 80] where the graphene layer doping and distance dependence are considered for quantum emitters at telecommunication wavelengths. The interaction length between a pair of quantum emitters in the presence of a graphene nanodisk is enhanced up to one order of magnitude compared to the free space value, and a comparison with an infinite graphene monolayer is also provided. Furthermore, the electrostatic nature of the interaction suggests that the main influence comes from the geometrical characteristics of the graphene nanodisk. The formalism developed in this chapter is quite general and can be applied to any two dimensional material provided its conductivity is known and the electrostatic regime applies.

6.2 Theoretical Introduction

In this section are introduced the basic quantities used throughout this chapter to investigate the system sketched in Fig. 6.1. The conductivity of the graphene nanodisk is described by the model introduced in Sec. 5.2.1. In Sec. 6.2.1 the Poisson equation is solved by using an expansion to a known set of functions. In Sec. 6.2.2 the electrostatic Green's tensor is constructed with the aid of which the SE emission of a quantum emitter and the energy transfer between a pair of quantum emitters in the presence of a graphene nanodisk are calculated.

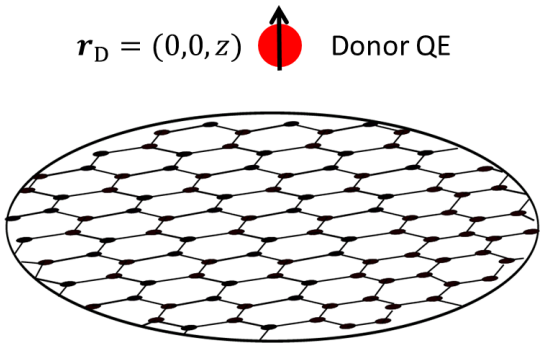

Figure 6.1: *Schematic of the geometry under consideration, a QE in the presence of a graphene nanodisk of radius R.*

6.2.1 Eigenvalues and eigenfunctions

The electrostatic potential, $\phi(\mathbf{r})$, in the case of a graphene nanodisk is given by the Poisson equation,

$$\nabla^2\phi(\mathbf{r}) = -\frac{1}{\varepsilon_0\varepsilon(\mathbf{r})}\rho(\mathbf{r}), \tag{6.1}$$

where the charge density of the graphene nanodisk is given by $\rho(\mathbf{r}) = \delta(z)\rho_{\shortparallel}(r,\theta)\Theta(R-r)$, which vanishes for $r > R$, the background dielectric permittivity is given by $\varepsilon(\mathbf{r}) = \varepsilon_+\theta(z) + \varepsilon_-\theta(-z)$, with $\varepsilon_+ = \varepsilon_- = 1$. Taking advantage of the azimuthal symmetry of the problem under consideration we write the electrostatic field in the form $\phi(\mathbf{r}) = \phi_{\shortparallel}(r)\phi_z(z)\exp(il\theta)$, with the condition $\phi_z(0) = 1$. Similarly, the charge density has the form $\rho_{\shortparallel}(\mathbf{r}_{\shortparallel}) = \rho_{\shortparallel}(r)\exp(il\theta)$. We start by considering only modes with angular dependence, $l \neq 0$. Applying a Hankel transform on Eq. (6.1) for the lth order, when $z \neq 0$, the electrostatic potential has the form:

$$\phi(\mathbf{r}) = \int_0^\infty p\phi(p,z)J_l(pr)e^{il\theta}dp. \tag{6.2}$$

Substituting (6.2) into Eq. (6.1), the following differential equation is obtained:

$$\left(\frac{d^2}{dz^2} - p^2\right)\phi(p,z) = 0. \tag{6.3}$$

A general solution of this equation reads $\phi(p,z) = A_\pm\exp(\mp pz)$. Applying the relevant boundary conditions, that the potential ϕ is continuous and its normal derivative has a discontinuity of the form

$$\varepsilon_+\frac{\partial\phi(p,z)}{\partial z}\bigg|_{z=0^+} - \varepsilon_-\frac{\partial\phi(p,z)}{\partial z}\bigg|_{z=0^-} = \rho_{\shortparallel}(p), \tag{6.4}$$

the coefficients are found to have the form $A_{\pm} = \frac{1}{2\varepsilon_{\pm}}\rho_{||}(p)\frac{1}{p}$. The total field is given by the inverse Hankel transform of $\phi(p,z)$, which, when used in Eq. (6.2) yields,

$$\phi_{||}(\tilde{r}) = \frac{R}{2\varepsilon_0}\int_0^1 d\tilde{r}' K_l(\tilde{r},\tilde{r}')\rho_{||}(\tilde{r}')\tilde{r}', \tag{6.5}$$

where $\tilde{r} = r/R$ and $K_l(\tilde{r},\tilde{r}') = 1/R\int_0^{\infty} dp J_l(p\tilde{r})J_l(p\tilde{r}')$. From now on for simplicity the change of variable $\tilde{r} \to r$ is understood, unless otherwise specified.

By using Ohm's law, $\mathbf{J} = \sigma(\omega)\mathbf{E}$, and the continuity equation, $i\omega\rho(r) = \nabla\cdot\mathbf{J}$, one finds the expression

$$\phi(r) = \frac{i\omega}{\sigma(\omega)}\int_0^1 dr' G_l(r,r')\rho(r')r', \tag{6.6}$$

where

$$\left(\frac{1}{r}\frac{\partial}{\partial r}r\frac{\partial}{\partial r} - \frac{l^2}{r^2}\right)G_l(r,r') = -\frac{\delta(r-r')}{r}, \tag{6.7}$$

subject to the boundary conditions that $G_l(0,r')$ is bounded and $\partial_r G(r,r')|_{r=1^-} = 0$. The solution of Eq. (6.7) is

$$G_l(r,r') = \frac{1}{2l}\left((rr')^l + \left(\frac{r_<}{r_>}\right)^l\right), \tag{6.8}$$

where $r_> = \max(r,r')$ and $r_< = \min(r,r')$, for $l \neq 0$.

Using Eq. (6.5) and (6.6) and including the external potential $\phi^{ext}(r,r')$, we obtain the expression

$$\Omega^2(\omega)\int_0^1 dr' K_l(r,r')\rho_{||}(r')r' - \omega^2\int_0^1 dr' G_l(r,r')\rho(r')r' = -\phi^{ext}(r,r'), \tag{6.9}$$

where $\Omega^2(\omega) = -i\omega\sigma(\omega)/2\varepsilon_0 R$. To solve Eq. (6.9) the charge density is expanded by using the Jacobi polynomials

$$\rho_{||}(r) = r^l\sum_{j=0}^{\infty} c_j P_j^{(l,0)}(1-2r^2). \tag{6.10}$$

In order to calculate the integrals in Eq. (6.9) and replace the integral equation with matrix equations, the orthogonality condition of the Jacobi polynomials is used

$$\int_0^1 dr P_i^{(l,0)}(1-2r^2)P_j^{(l,0)}(1-2r^2)r^{2l+1} = \frac{\delta_{ij}}{2(l+2j+1)}, \tag{6.11}$$

as well as the integral identities

$$\int_0^\infty dr\, r^{l+1} J_l(pr) P_j^{(l,0)}(1-2r^2) = \frac{1}{p} J_{l+2j+1}(p) \tag{6.12}$$

and

$$\int_0^\infty p^{-2} J_{l+2i+1}(p) J_{l+2j+1}(p) dp = \frac{(-1)^{i-j+1}}{\pi[4(i-j)^2-1](l+i+j+1/2)(l+i+j+3/2)}. \tag{6.13}$$

Then, a system of matrix equation is obtained

$$(-\omega \mathbf{G} + \Omega(\omega)\mathbf{K})\mathbf{c} = \frac{i\omega\sigma(\omega)}{R^2}\mathbf{D}\mathbf{d}, \tag{6.14}$$

where the potential created by an external source is expanded as

$$\phi^{ext}(\mathbf{r}, \mathbf{r}') = r^l \sum_{j=0}^{\infty} d_j P_j^{(l,0)}(1-2r^2). \tag{6.15}$$

When one neglects the external potential $\phi^{ext}(r, r')$, one is left with an eigenvalue problem

$$\mathbf{K}\mathbf{c}_n = \zeta_n \mathbf{G}\mathbf{c}_n \tag{6.16}$$

where ζ_n are geometric modes that are once and for all calculated for the specific geometry and are independent of the disk radius R, l is the angular eigenmode and n is the radial eigenmode. Then the resonance frequencies are found from the relation $\zeta_n = \Omega^2(\omega_n)/\omega_n^2$, see Eq. (6.38). The matrices **D**, **G** and **K** have the form

$$D_{ij}^l = \frac{\delta_{ij}}{2(l+2j+1)}, \tag{6.17}$$

$$G_{ij}^l = \frac{\delta_{j0}\delta_{i0}}{8l(l+1)^2} + \frac{\delta_{ij}}{4(l+2j)(l+2j+1)(l+2j+2)} + \frac{\delta_{i+1,j}}{8(l+2j+1)(l+2j+2)(l+2j+3)} + \\ + \frac{\delta_{i,j+1}}{8(l+2j+1)(l+2j+2)(l+2j+3)}, \tag{6.18}$$

$$K_{ij}^l = \frac{(-1)^{i-j+1}}{\pi[4(i-j)-1](l+i+j+1/2)(l+i+j+3/2)}. \tag{6.19}$$

The above expressions are valid for $l \neq 0$. When these angular modes are considered there is no net induced charge density. The situation for the breathing mode, $l = 0$, is different, as we

need to modify the boundary conditions at $\tilde{r} = 1$.

Eq. (6.8) is no longer valid for $l = 0$ and the boundary condition is modified to read as $\partial_r G(r,r')|_{r=1^-} = 1$, in which case the Green's function has the form

$$G(r,r') = -\ln(r_>), \tag{6.20}$$

where $x_> = \max(r,r')$. For $l = 0$ the expansion of the charge density, ρ_{II}, is still valid and the Jacobi polynomials become the Legendre polynomials. Following similar considerations we find that the matrix equation Eq. (6.14) is still valid. Also the matrices (6.17)-(6.19) are correct except for the fact that $i, j = 1,2,3\ldots$. More details can be found in ref. [165].

The induced electrostatic potential in the presence of an external source is written as

$$\phi^{\text{ind}}(\mathbf{r},\mathbf{r}') = \frac{R}{2\varepsilon_0}\sum_{l,n}^{\infty} c_n^l(\mathbf{r}',\omega)\cos(l\theta)\int_0^{\infty} p^{-1}e^{-|z|/Rp}J_l(pr)J_{l+2n+1}(p)dp, \tag{6.21}$$

where for $l = 0$, $n = 1,2,3\ldots$ and for $l > 1$, $n = 0,1,2\ldots$. In Eq. (6.21) $\mathbf{r}$ and $\mathbf{r}'$ are the non-normalized vectors.

6.2.2 Electrostatic Green's tensor

In this section as an external excitation we consider the potential produced by a dipole source in order to investigate the interactions between quantum emitters in the presence of a gated graphene nanodisk.

The potential at $\mathbf{r}$ created by a dipole source positioned at $\mathbf{r}' = (0,0,z')$ and oriented along $\hat{x}$ is given by

$$\phi^{ext}(\mathbf{r},\mathbf{r}') = \frac{p_0}{4\pi\varepsilon_0}\frac{|x-x'|}{((x-x')^2+(y-y')^2+(z-z')^2)^{3/2}} = \frac{p_0}{8\pi\varepsilon_0 R^2}\frac{r(e^{i\theta}+e^{-i\theta})}{(r^2+(z-z')^2)^{3/2}}, \tag{6.22}$$

where p_0 is the dipole moment of the quantum emitter in our case, and the term $1/R^2$ comes from the normalized values we use, $r \to Rr$.

Writing the dipole potential in terms of the Jacobi polynomials, in the xy plane at $z = 0$, as

$$\phi^{ext}(\mathbf{r},\mathbf{r}') = r^l\sum_{j=0}^{\infty} d_j P_j^{(l,0)}(1-2r^2), \tag{6.23}$$

and using Eq. (6.22) and (6.27) , as well as the orthogonality condition Eq. 6.11, the expansion

coefficients are given by

$$d_i^1 = (2i+2)\frac{p_0}{4\pi\varepsilon_0 R^2}\int_0^1 \frac{r^3 P_i^{(1,0)}(1-2r^2)}{(r^2+(z'/R)^2)^{3/2}}dr, \tag{6.24}$$

where only the $l=1$ terms survive from the expansion, due to the dipole orientation of the dipole source along x. The d_i^1 are then the components of the vector $\mathbf{d}$ of Eq. (6.14).

The induced electrostatic Green's tensor is given by the expression

$$\mathfrak{G}^{\text{ind}}(\mathbf{r},\mathbf{r}',\omega) = \varepsilon_0 c^2/(\omega p_0)\nabla\phi^{\text{ind}}(\mathbf{r},\mathbf{r}'), \tag{6.25}$$

using Eq. (6.21) and for the xx transition dipole moments has the form

$$\mathfrak{G}_{xx}^{\text{ind}}(\mathbf{r},\mathbf{r}',\omega) = \frac{c^2}{\omega^2}\sum_k c_k^1(z')\int_0^\infty [J_0(pr)-J_2(pr)]J_{2k+2}(p)e^{-|z|/Rp}dp \tag{6.26}$$

where the expansion coefficient for the case of a dipole oriented along $\hat{x}$ has only the $l=1$ terms and depends on the dipole position through the expansion of the dipole field Eq. (6.24).

When the acceptor QE is also placed in the middle of the graphene nanodisk, $\mathbf{r}=(0,0,z)$, the integral in Eq. (2.26) can be performed analytically, leading to the full result

$$\mathfrak{G}_{xx}^{\text{ind}}(\mathbf{r},\mathbf{r}',\omega) = -\frac{c^2}{2\omega^2}\sum_{k=0}^{\infty} c_k^1(z')\frac{\left[\sqrt{(z/R)^2+1}-z/R\right]^{2k+2}}{\sqrt{(z/R)^2+1}}, \tag{6.27}$$

where we used the identities

$$\frac{\partial}{\partial r}J_1(p\tilde{r}) = \frac{p}{R}\frac{1}{2}[J_0(p\tilde{r})-J_2(p\tilde{r})] \tag{6.28}$$

$$\int_0^\infty e^{-ax}J_n(\beta x)dx = \frac{\beta^{-n}[\sqrt{a^2+\beta^2}-a]^n}{\sqrt{a^2+\beta^2}}. \tag{6.29}$$

Similarly, the electrostatic potential at $\mathbf{r}$ created by a dipole source positioned at $\mathbf{r}'=(0,0,z')$ and oriented along $\hat{z}$ is given by

$$\phi^{ext}(\mathbf{r},\mathbf{r}') = \frac{|z-z'|}{((x)^2+(y)^2+(z-z')^2)^{3/2}} = \frac{1}{R^3}\frac{|z-z'|}{(r^2+(z-z')^2/R^2)^{3/2}}. \tag{6.30}$$

Due to the symmetry only the $l=0$ term in the expansion will survive and, like Eq. (6.24), the

expansion coefficients have the expression

$$d_i^0 = 2(2i+1)\frac{z'}{R^3}\int_0^1 \frac{rP_i^{(0,0)}(1-2r^2)}{(r^2+z'/R^2)^{3/2}}, \tag{6.31}$$

where the d_i^0 are then the components of the vector $\mathbf{d}$ of Eq. (6.14).

The zz component of the electrostatic induced Green's tensor, describing the relevant transition dipole moment, is given by the expression

$$\mathfrak{G}_{zz}^{\mathrm{ind}}(\mathbf{r},\mathbf{r}',\omega) = \frac{\mp c^2}{2\omega^2}\sum_k c_k^0(z')\int_0^\infty J_0(pr)J_{2k+2}(p)e^{-|z|/Rp}dp, \tag{6.32}$$

where the minus (plus) signs holds for $z>0$ ($z<0$). Again, when the acceptor QE is placed at $\mathbf{r}=(0,0,z)$, the integral in Eq. (6.32) can be calculated analytically, yielding

$$\mathfrak{G}_{zz}^{\mathrm{ind}}(\mathbf{r},\mathbf{r}',\omega) = \frac{\mp c^2}{2\omega^2}\sum_{k=1}^{\infty} c_k^0(z')\frac{\left[\sqrt{(z/R)^2+1}-z/R\right]^{2k+1}}{\sqrt{(z/R)^2+1}}. \tag{6.33}$$

The integrals in Eq. (6.24) and (6.31) can be calculated analytically for each order k, and below we provide the expressions for a few values of k,

$$d_{k=0}^{l=1} = \frac{2}{R^3}\frac{(\sqrt{R^2+z^2}-z)^2}{\sqrt{R^2+z^2}}, \tag{6.34}$$

$$d_1^0 = -6\frac{z}{R^3}\left(\frac{R}{z}\frac{\sqrt{R^2+z^2}-z}{\sqrt{R^2+z^2}} - 2\frac{\left(\sqrt{R^2+z^2}-z\right)^2}{R\sqrt{R^2+z^2}}\right), \tag{6.35}$$

$$d_2^0 = -10\frac{z}{R^3}\left(\frac{R}{z}\frac{\sqrt{R^2+z^2}-z}{\sqrt{R^2+z^2}} - 6\frac{\left(\sqrt{R^2+z^2}-z\right)^2}{R\sqrt{R^2+z^2}} + \text{Higher order terms}\right). \tag{6.36}$$

6.3 Results and Discussion

6.3.1 Spontaneous emission rate

The spontaneous decay rate, γ, is proportional to the strength of the transition dipole moments and the electromagnetic field strength acting on it. The normalized spontaneous emis-

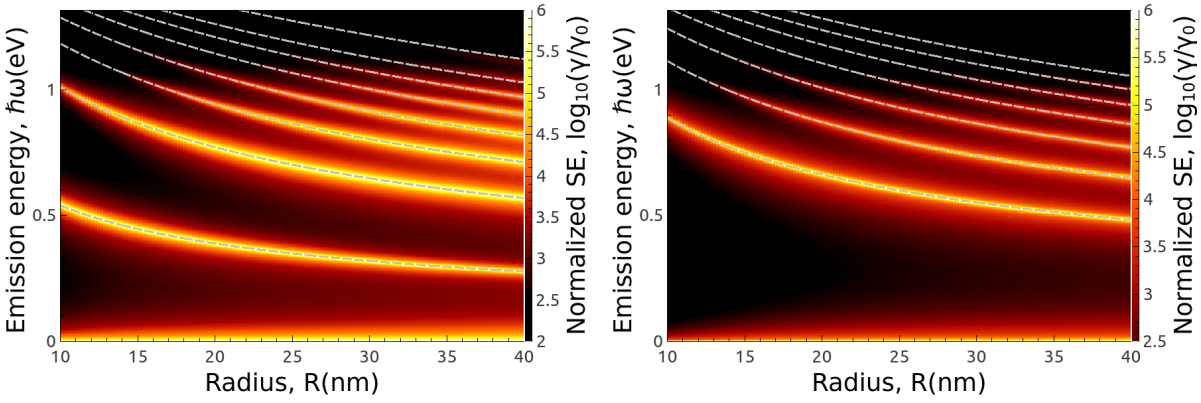

(a) *x-oriented dipole* **(b)** *z-oriented dipole*

Figure 6.2: *Normalized spontaneous emission rate of a quantum emitter placed* 10 *nm above the center of a graphene nanodisk for a fixed value of the chemical potential,* $\mu = 1\,eV$*, as a function of emission frequency and disk radius, R, for (a) x-oriented and (b) z-oriented transition dipole moment of the emitter. The dashed lines represent numerical solutions of Eq. (6.38).*

sion rate was introduced in Sec. 2.3 and has the form

$$\frac{\gamma}{\gamma_0} = 1 + \frac{6\pi c}{\omega}\mathrm{Im}(\mathbf{n}_{\mathrm{QE}} \cdot \mathfrak{G}^{\mathrm{ind}}(\mathbf{r}', \mathbf{r}', \omega) \cdot \mathbf{n}_{\mathrm{QE}}) \tag{6.37}$$

where the free space spontaneous emission is given by $\gamma_0(\omega) = \omega^3 |\mathbf{p}|^2 / 3\pi\varepsilon_0\hbar c^3$ and $\mathbf{n}_{\mathrm{QE}}$ is a unit vector along the direction of the transition dipole moment of the quantum emitter.

In Fig 6.2 a contour plot of the SE rate is presented as a function of the emission frequency of the quantum emitter, ω, and the radius of the graphene nanodisk, R, when the dipole emitter is located at $\mathbf{r}_{\mathrm{D}} = (0, 0, 10\,\mathrm{nm})$ and the value of the chemical potential is fixed at $\mu = 1\,\mathrm{eV}$. In panel 6.2a the dipole is oriented along the x-axis, while in panel 6.2b it is along the z-axis. For both orientations, as the radius of the graphene nanodisk is increased, more resonances are emerging; this is due to the fact that modes with a higher order k can now contribute in Eqs. (6.23) and (6.33). The values of the resonance frequencies are found by setting the external excitation to zero in Eq. (5.21) and then numerically solving the equation

$$\frac{\sigma(\omega_k^l)}{\omega_k^l} = \frac{2i\varepsilon_0 R}{\zeta_k^l}, \tag{6.38}$$

where ζ_k^l are the geometric modes of the particular geometry which can be calculated through Eq. (6.16). Considering only the intraband contribution to the surface conductivity, $\sigma(\omega) = 8i\pi\alpha_0 c k_B T \ln(2\cosh(\mu/2k_BT))/[\pi(\hbar\omega)]$, where α_0 is the fine structure constant, ignoring the relaxation time, τ, and noting that $\mu/k_BT \gg 1$ for the chemical potential values considered in

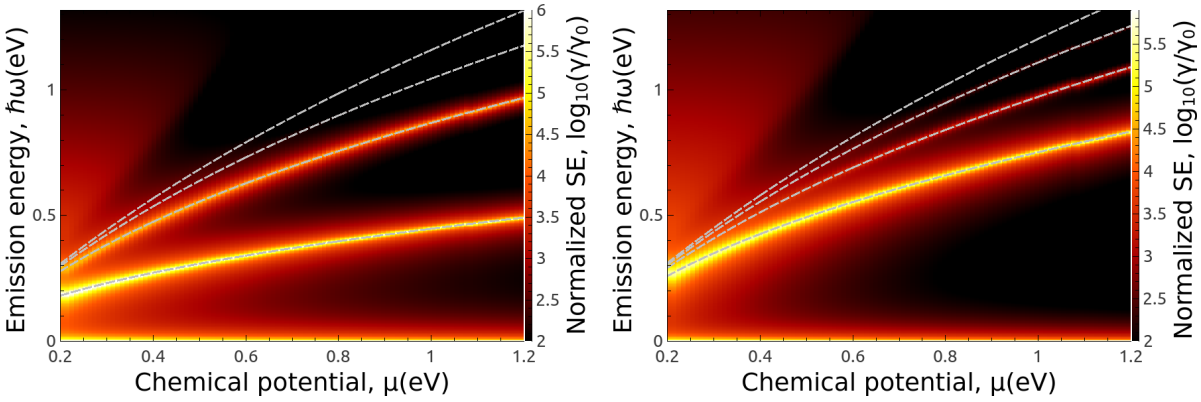

(a) *x-oriented dipole* **(b)** *z-oriented dipole*

Figure 6.3: *Normalized spontaneous emission rate of a quantum emitter placed* 10 *nm above the center of a graphene nanodisk with a fixed radius,* $R = 15\,nm$*, as a function of frequency and the chemical potential,* μ*, for (a) x-oriented and (b) z-oriented transition dipole moment of the quantum emitter. The dashed lines represent numerical solutions of Eq. (6.38).*

this chapter, the following expression is obtained for the resonance frequencies:

$$\omega_k^l = \sqrt{\frac{4\alpha_0 c \zeta_k^l \mu}{\hbar R}}. \tag{6.39}$$

This expression gives the approximate physical connection of the resonance frequencies with the geometric modes, ζ_k^l, the chemical potential, μ, and the graphene nanodisk radius, R. It is observed that for $l = 1$, x oriented dipole, and $l = 0$, z oriented dipole, different sets of resonance frequencies are excited. From Eq. (6.39) it can be easily seen that, as the radius is increased, the resonance frequencies are red-shifted, following a $\sqrt{1/R}$ dependence. The dashed lines in Fig. 6.2 represent precise numerical solutions of Eq. (6.38) and it is clear that the sharp resonance peaks in the SE rate follow the trend described by Eq. 6.39 for the resonance frequencies.

Eq. (6.39) also easily accounts for the behavior of the SE rate as a function of the chemical potential following a $\sqrt{\mu}$ dependence, as seen in Fig. 6.3. Here we present a contour map of the SE rate of a quantum emitter placed at $\mathbf{r}_D = (0, 0, 10\,\text{nm})$, above a graphene nanodisk of radius $R = 15\,\text{nm}$, as a function of the emission frequency of the quantum emitter and the chemical potential of the graphene nanodisk. The emerging resonances are now blueshifted with increasing the value of the chemical potential, μ. Thus, by changing the value of the chemical potential, the graphene nanodisk resonances can be tuned to selectively couple to specific quantum emitters.

As the distance between the quantum emitter and the graphene nanodisk is increased, their

interaction decreases, and at large distances it reverts to its free-space behavior. The orientation of the dipole quantum emitter has a large influence on the distance dependence. The spontaneous emission rate is given by the field induced by the dipole source, which can be found from Eqs. (6.23) and (6.33). From these expressions, the induced field can be written as $\mathfrak{G}^{\text{ind}}(\mathbf{r}',\mathbf{r}',\omega) = \text{Resonance}\times\text{Geometrical dependence}$. The Resonance term is given by $\mathbf{M} = (-\omega\mathbf{G} + \Omega(\omega)\mathbf{K})^{-1}$ which is maximum at the resonance frequencies calculated from Eq. (6.38). The Geometrical term is connected with the expansion coefficients of the dipole source, see Eqs. (6.24) and (6.31).

Considering the distance dependence of the SE rate of a quantum emitter placed at $\mathbf{r}' = (0,0,z')$ and with a transition dipole moment oriented along the x-axis, focusing only on the $k=0$ term, the induced electrostatic Green's tensor then has the form:

$$\mathfrak{G}^{\text{ind}}_{xx,k=0}(\mathbf{r}',\mathbf{r}',\omega) = -\frac{1}{2}c^1_{k=0}\frac{\left[\sqrt{(z'/R)^2+1}-z'/R\right]^2}{\sqrt{(z'/R)^2+1}}, \tag{6.40}$$

with

$$c^1_0 = \frac{i\omega}{R^2}\sigma(\omega)M^1_{i0}D_{00}\frac{1}{R^2}\int_0^1 \frac{x^3}{(x^2+(z'/R)^2)^{3/2}}dx. \tag{6.41}$$

From this, the distance dependence of the Green's tensor becomes:

$$\mathfrak{G}^{\text{ind}}_{xx,k=0}(\mathbf{r}',\mathbf{r}',\omega) = \text{Resonance}\frac{1}{R^9}\frac{\left[\sqrt{(z'^2+R^2}-z'\right]^4}{z'^2+R^2}. \tag{6.42}$$

If the transition dipole of the quantum emitter is along the z-axis, i.e. perpendicular to the graphene nanodisk, the distance dependence of the Green's tensor is somewhat more complicated. Nevertheless, focusing on the $k=2$ term, the induced electrostatic Green's tensor has the form:

$$\mathfrak{G}^{\text{ind}}_{zz,k=2}(\mathbf{r}',\mathbf{r}',\omega) = -c^0_{k=2}\frac{\left[\sqrt{(z'/R)^2+1}-z'/R\right]^5}{\sqrt{(z'/R)^2+1}} \tag{6.43}$$

with

$$c^0_2 = \frac{i\omega}{R^2}\sigma(\omega)M^0_{ij}D_{jj}d^0_2. \tag{6.44}$$

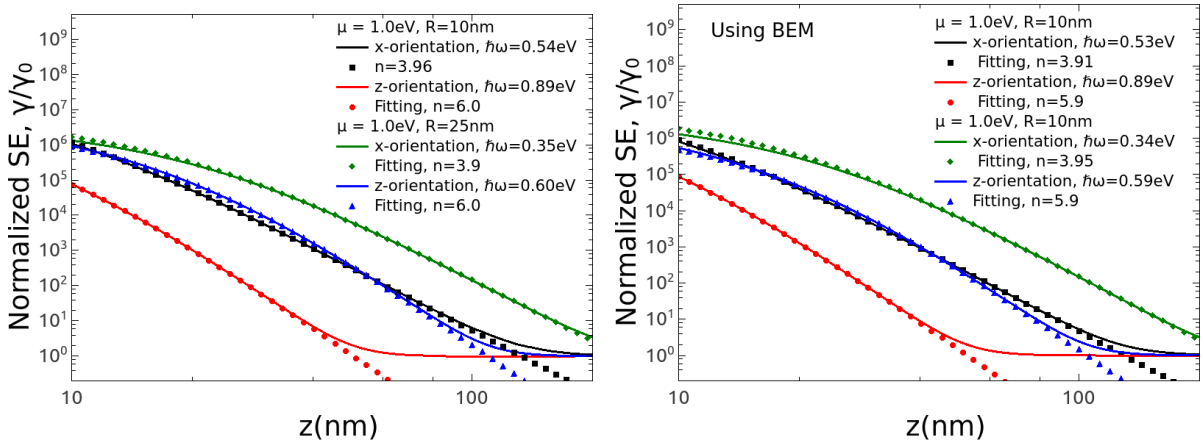

(a) *Electrostatic mode expansion* **(b)** *Boundary element method*

Figure 6.4: *Spontaneous emission of a quantum emitter as a function of its position,* $\mathbf{r}_D = (0,0,z)$*, above the graphene nanodisk, for a chemical potential,* $\mu = 1$ *eV and radii* $R = 10$ *nm and* $R = 25$ *nm. (a) Mode expansion. (b) Boundary element method.*

After some algebraic manipulation the distance dependence is obtained as:

$$\mathfrak{G}^{\text{ind}}_{zz,k=2}(\mathbf{r}',\mathbf{r}',\omega) = \text{Resonance}\frac{1}{R^4}\frac{\left[\sqrt{(z'^2+R^2}-z'\right]^6}{z'^2+R^2}. \tag{6.45}$$

In order to examine these approximate forms of the dependence of the SE rate on the distance away from the graphene nanodisk, in Fig. 6.4 several examples are presented, where the full calculations are fitted using an expression of the form $f(z,R) = A\left(\sqrt{z^2+R^2}-z\right)^n/\left(z^2+R^2\right)$, with A and n being the fitting parameters. The choice of this expression is suggested naturally by Eqs. (6.42) and (6.45). A good agreement of the fitting with the full numerical calculation is found, which shows that the distance dependence follows the analytical expressions introduced earlier. In particular, in Fig. 6.4a it is shown that for the z-oriented dipole and radii $R = 10\,\text{nm}$ and $R = 25\,\text{nm}$, the value of the fitting parameter $n = 6$ coincides precisely with the value given by Eq. (6.45). For the x-orientation it is found that $n = 3.9$ is very close to the analytical value $n = 4$ given by Eq. (6.42). The general behavior is, of course, more complicated than described by Eqs. (6.45) and (6.42), since different orders, k, contribute to each resonance. For the case of a dipole source oriented along the z-axis and for the $k = 2$ order, we can see from Eq. (6.36) that there are different values of n that we can use as a fitting parameter. Nevertheless, the general distance dependence behavior can be explained with the fitting expression.

In order to compare the electrostatic approximation with full numerical results, the bound-

ary element method open source code MNPBEM has been used [166, 167]. In MNPBEM the graphene disk is modeled as a thin layer of thickness $d = 0.5\,\text{nm}$ with a dielectric permittivity described by [168]

$$\varepsilon(\omega) = 1 + \frac{4\pi i\sigma(\omega)}{\omega d}, \tag{6.46}$$

where the surface conductivity is given by Eq. (5.9). Importantly, the full numerical results in Fig. 6.4b give almost the same fitting parameters, A and n.

Thus, it is found that the dependence of the SE rate of a quantum emitter on its distance to a graphene nanodisk is primarily given by the geometrical characteristics of the structure and not by the material characteristics of the graphene nanodisk. For comparison we consider the distance dependence of a quantum emitter above an infinite graphene sheet, this behaves as $\exp(-z/\delta_{\text{SP}})$, where δ_{SP} is the penetration depth of the surface plasmon on an infinite graphene sheet, given by $\delta_{\text{SP}} = \text{Im}\left(1/k_z^{\text{SP}}\right)$ with $k_z^{\text{SP}} = \sqrt{k^2 - k_{\text{SP}}^2}$ [97]. When an infinite graphene sheet is considered with chemical potential $\mu = 1\,\text{eV}$, the penetration depth is $\delta_{\text{SP}} = 24\,\text{nm}$ at $\hbar\omega = 0.35\,\text{eV}$ and $\delta_{\text{SP}} = 7\,\text{nm}$ at $\hbar\omega = 0.6\,\text{eV}$, see Fig. (5.2b). Fig. 6.4a shows, on the other hand, that the QE can interact with the graphene nanodisk at up to 80 nm for the z-orientation and up to 200 nm for the x-orientation, distances considerably larger than the penetration depth.

6.3.2 Energy Transfer Function

In this section we present results regarding the enhancement of the ET function between a pair of quantum emitters placed in proximity to the graphene nanodisk. To do so the full Green's tensor is used, see Sec. (3.1), which has the form

$$\mathfrak{G}(\mathbf{r}_{\text{A}}, \mathbf{r}_{\text{D}}, \omega) = \mathfrak{G}^{\text{ind}}(\mathbf{r}_{\text{A}}, \mathbf{r}_{\text{D}}, \omega) + \mathfrak{G}^{\text{hom}}(\mathbf{r}_{\text{A}}, \mathbf{r}_{\text{D}}, \omega), \tag{6.47}$$

where the induced part of the electrostatic Green's tensor is given by Eq. (6.26) and Eq. (6.32) for the x and z oriented transition dipole moments, respectively, and $\mathfrak{G}^{\text{hom}}(\mathbf{r}, \mathbf{r}', \omega)$ is the electrostatic homogeneous Green's tensor which is given by the expression

$$\mathfrak{G}_{ij}^{\text{hom}}(\mathbf{r}_{\text{A}}, \mathbf{r}_{\text{D}}, \omega) = \frac{c^2}{4\pi\omega^2 R^2}(3\hat{R}_i\hat{R}_j - 1), \tag{6.48}$$

with $\mathbf{R} = \mathbf{r}_{\text{A}} - \mathbf{r}_{\text{D}}$. The ET function is defined as, see (2.34),

$$\Gamma(\mathbf{r}_{\text{A}}, \mathbf{r}_{\text{D}}, \omega) = \frac{2\pi}{\hbar^2}\left(\frac{\omega^2}{c^2\varepsilon_0}\right)^2 \left|\mathbf{p}\cdot\mathfrak{G}(\mathbf{r}_{\text{A}}, \mathbf{r}_{\text{D}}, \omega)\cdot\mathbf{p}'\right|^2, \tag{6.49}$$

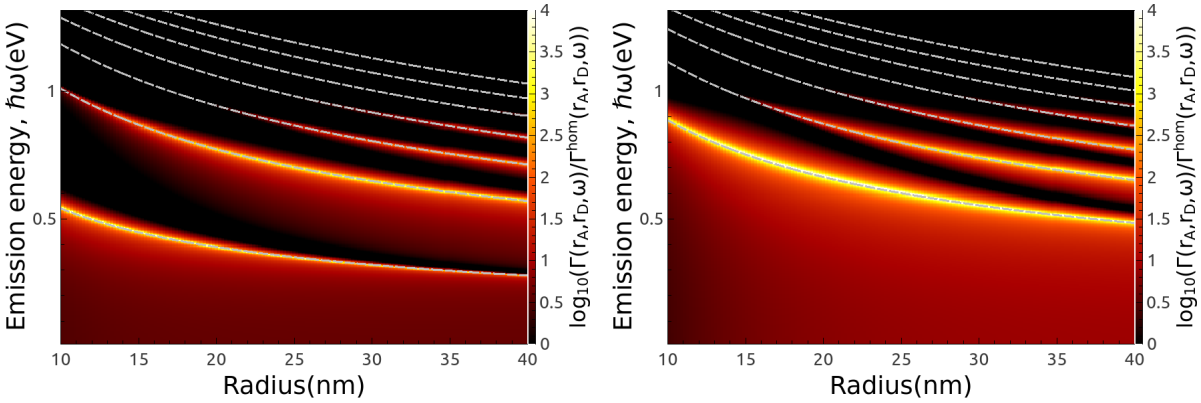

(a) *x-oriented dipole* **(b)** *z-oriented dipole*

Figure 6.5: *Normalized ET function between a pair of quantum emitters, when the donor is positioned at* $\mathbf{r}_D = (0,0,10\,nm)$ *and the acceptor is positioned at* $\mathbf{r}_A = (0,0,-10\,nm)$*, for a fixed value of the chemical potential,* $\mu = 1\,eV$*, as a function of disk radius, R, for two orientations, (a) x-orientation and (b) z-orientation of the transition dipole moments of the donor and acceptor. The dashed lines represent numerical solutions of Eq. (6.38).*

where $\mathbf{p}$ and $\mathbf{p}'$ are the acceptor and donor transition dipole moments, respectively.

Starting by considering the donor placed at $\mathbf{r}_\mathrm{D} = (0,0,10\,\mathrm{nm})$ and the acceptor placed exactly on the opposite side of a graphene nanodisk, $\mathbf{r}_\mathrm{A} = (0,0,-10\,\mathrm{nm})$, the enhancement of the ET function between them is investigated. Firstly, in Fig. 6.5 a contour plot of the logarithm of the normalized ET function, $\tilde{\Gamma}(\mathbf{r}_\mathrm{A},\mathbf{r}_\mathrm{D},\omega) = \Gamma(\mathbf{r}_\mathrm{A},\mathbf{r}_\mathrm{D},\omega)/\Gamma^\mathrm{hom}(\mathbf{r}_\mathrm{A},\mathbf{r}_\mathrm{D},\omega)$ see Eq. (2.35), is presented for a fixed value of the chemical potential, $\mu = 1\,\mathrm{eV}$, as a function of the radius of the graphene disk, R. Secondly, in Fig. 6.6 it is presented the normalized ET function, $\tilde{\Gamma}(\mathbf{r}_\mathrm{A},\mathbf{r}_\mathrm{D},\omega)$, for a fixed radius of the graphene nanodisk, $R = 15\,\mathrm{nm}$, as a function of the chemical potential, μ. Comparing Figs. 6.5 and 6.6 with Figs. 6.2 and 6.3, it is observed that the behavior of the ET function is very similar to the behavior of the SE rate, particularly the locations of the resonances.

In Fig. 6.7a and 6.8a we again consider fixed positions for the donor, $\mathbf{r}_\mathrm{D} = (0,0,10\,\mathrm{nm})$, and acceptor, $\mathbf{r}_\mathrm{A} = (0,0,-10\,\mathrm{nm})$, for a single value of chemical potential, $\mu = 1\,\mathrm{eV}$, for two disk radii, $R = 10$ nm and $R = 30$ nm, respectively. Furthermore, two different dipole orientations, x and z, are considered and are clearly seen the different resonance frequencies for the different orientations. It is also observed that the normalized ET function follows an asymmetric resonance of Fano type, and not a Lorentzian shape, as when considering the normalized SE rate, see Fig. (6.2) and (6.3). Moreover, as expected, for a graphene nanodisk with a larger radius, $R = 30\,\mathrm{nm}$, more resonance frequencies are visible. The dashed lines in Figs. 6.7a and 6.8a represent numerical simulations using MNPBEM and a good agreement is obtained between the two methods. In this regime the electrostatic method is expected to hold,

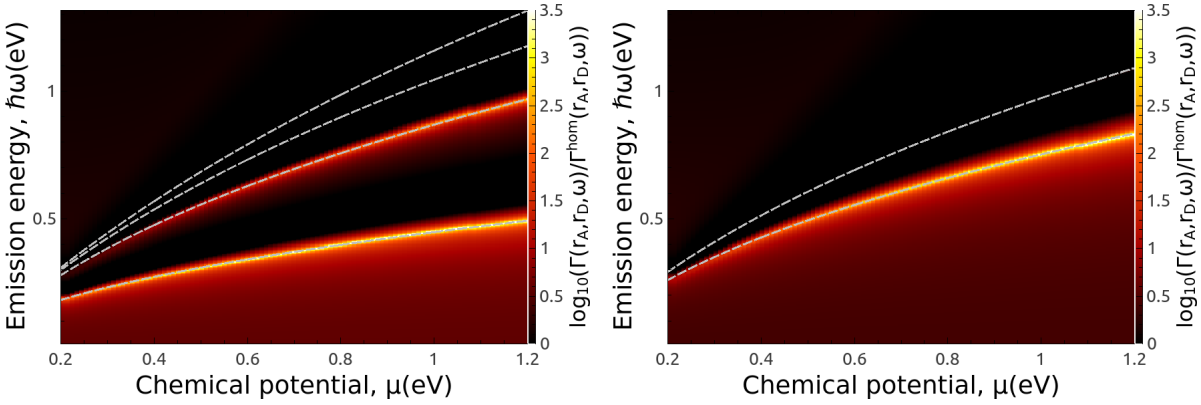

(a) *x-oriented dipole* **(b)** *z-oriented dipole*

Figure 6.6: *Normalized ET function between a pair of quantum emitters, when the donor is positioned at* $\mathbf{r}_D = (0,0,10\,nm)$ *and the acceptor is positioned at* $\mathbf{r}_A = (0,0,-10\,nm)$*, for a fixed radius of the graphene nanodisk,* $R = 15\,nm$*, as a function of the chemical potential,* μ*, for two orientations, (a) x-orientation and (b) z-orientation of the transition dipole moments of the donor and acceptor. The blue lines in each panel represents the resonance frequencies calculated using Eq. (6.39). The dashed lines represent numerical solutions of Eq. (6.38).*

since the donor-acceptor separations are smaller than the emission wavelength of the donor, $|\mathbf{r}-\mathbf{r}'| \ll \lambda$.

Panels (6.7b-6.7d) and (6.8b-6.8e) present contour plots of the normalized ET function when the donor is placed at a fixed position, $\mathbf{r}_\mathrm{D} = (0,0,10\,\mathrm{nm})$, and the acceptor scans the xz-plane, $\mathbf{r}_\mathrm{A} = (x,0,z)$. Panels (6.7b-6.7c) and (6.8b-6.8c) show the x-component of the transition dipole moment of both the donor and acceptor, while panels 6.7d and (6.8d-6.8e) show the z-component. The emission frequencies of the donor have been chosen from the peak values from panels 6.7a and 6.8a, in order to have the largest response of the graphene nanodisks. Details of the relevant parameters are found in the caption and below the individual panels.

Firstly it is observed that when both donor and acceptor transition dipole moments are along the x-axis, the largest ET function enhancement occurs in the region of the circumference; when both donor and acceptor transition dipole moments are along the z-axis, the normalized ET function is reduced. Furthermore, as the emission frequency is increased, higher order resonances are involved and, consequently, the number of lobes increases, a general characteristic of plasmonic finite structures when localized surface plasmons are excited. As the number of lobes is increased the field is more tightly confined to the graphene nanodisk.

Now we consider the ET function, $\Gamma(\mathbf{r}_\mathrm{A},\mathbf{r}_\mathrm{D},\omega) \propto \left|\mathfrak{G}^{\mathrm{ind}}(\mathbf{r}_\mathrm{A},\mathbf{r}_\mathrm{D},\omega)+\mathfrak{G}^{\mathrm{hom}}(\mathbf{r}_\mathrm{A},\mathbf{r}_\mathrm{D},\omega)\right|^2$, where the induced part is given by Eqs. (6.26) and (6.32). The interaction strength between the donor and acceptor is proportional to this quantity. Panels 6.9a and 6.9b present a contour plot of the ET function as a function of frequency and acceptor position for a fixed donor

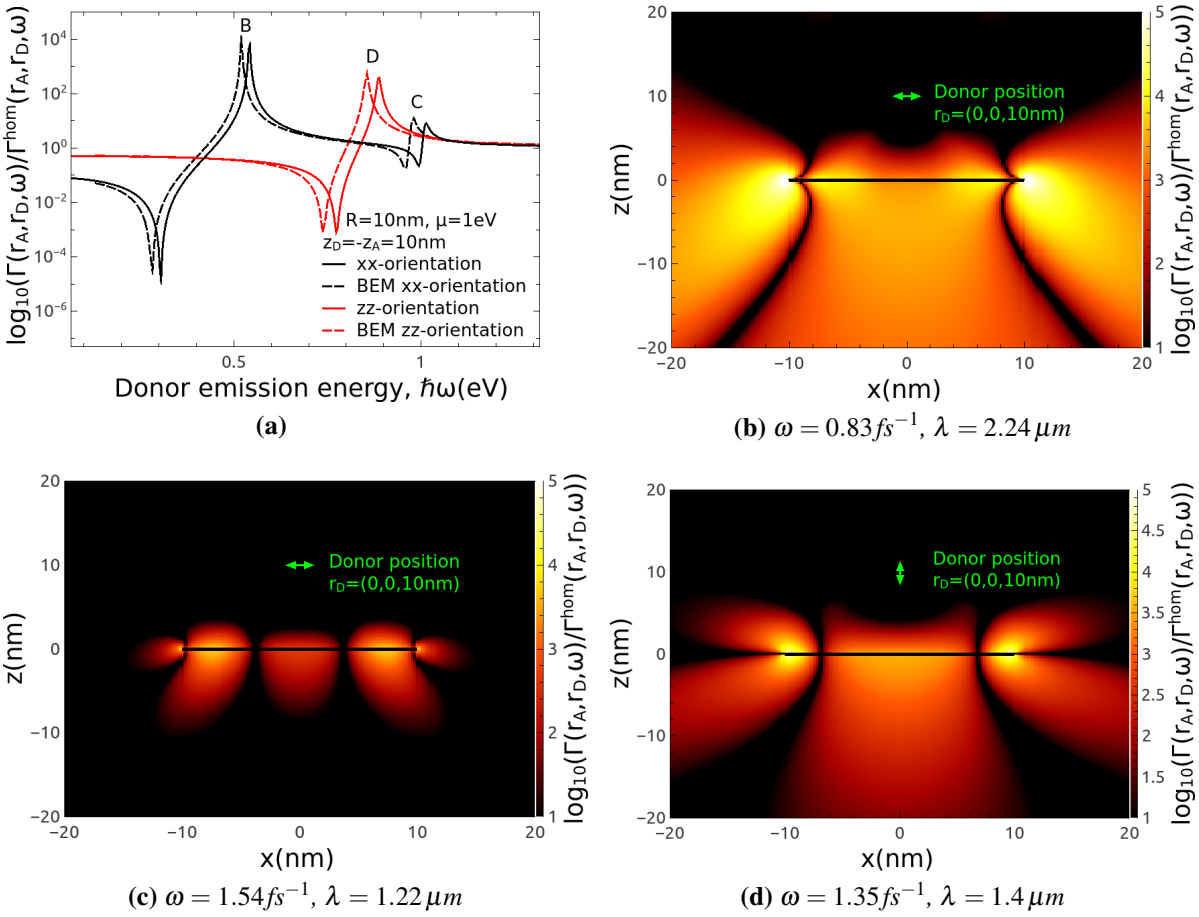

(a)

(b) $\omega = 0.83 fs^{-1}$, $\lambda = 2.24\,\mu m$

(c) $\omega = 1.54 fs^{-1}$, $\lambda = 1.22\,\mu m$

(d) $\omega = 1.35 fs^{-1}$, $\lambda = 1.4\,\mu m$

Figure 6.7: *Normalized ET function between a donor-acceptor pair, when the donor is positioned at* $\mathbf{r}_D = (0,0,10nm)$ *for a fixed radius,* $R = 10nm$*, and a fixed value of the chemical potential,* $\mu = 1eV$*. (a) Acceptor positioned at* $\mathbf{r}_A = (0,0,-10nm)$ *for two orientations, along the x and z-axes. For the peak frequencies labeled B, C and D we present contour plots of the spatial distribution in the xz-plane of the normalized ET function in the (b-d) graphs.*

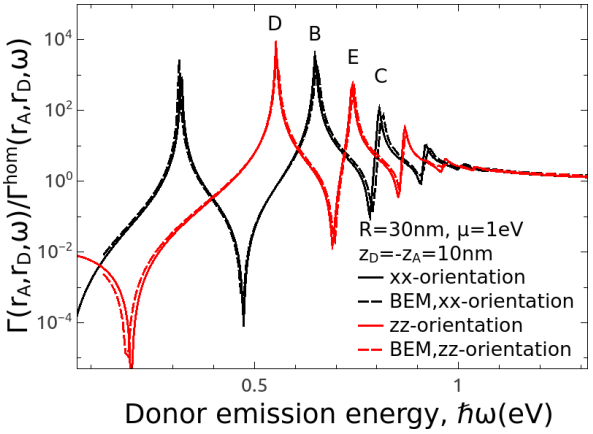

(a)

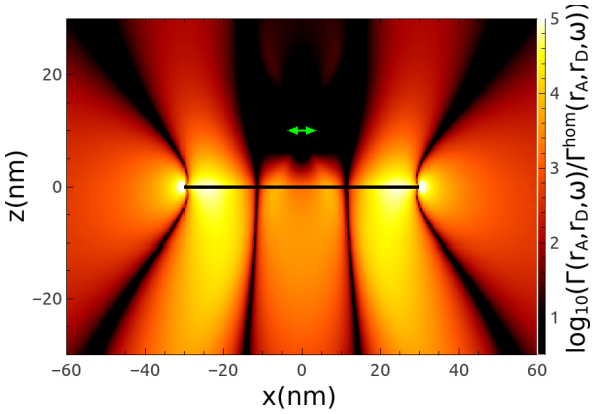

(b) $\omega = 0.98 fs^{-1}$, $\lambda = 1.91\,\mu m$

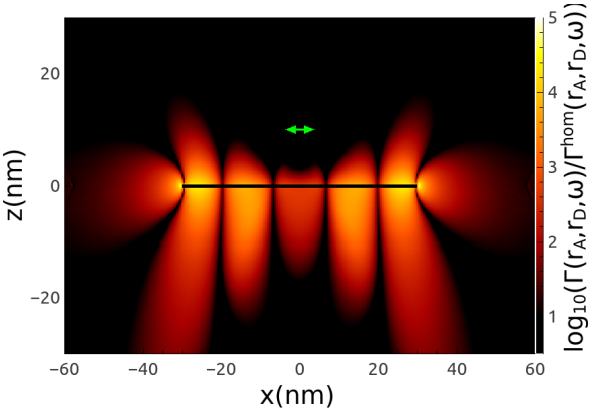

(c) $\omega = 1.22 fs^{-1}$, $\lambda = 1.54\,\mu m$

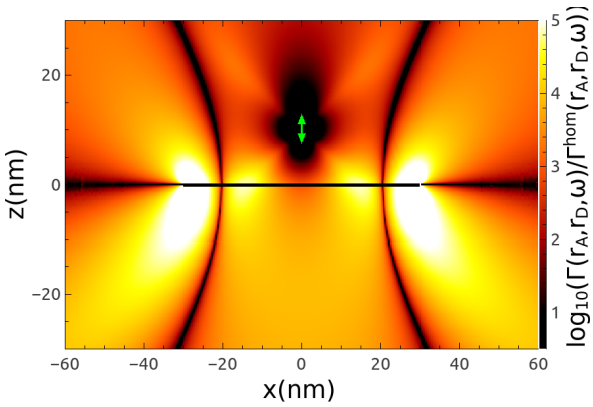

(d) $\omega = 0.83 fs^{-1}$, $\lambda = 2.27\,\mu m$

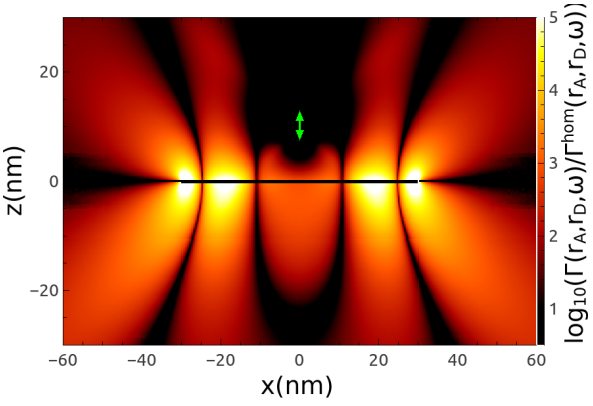

(e) $\omega = 1.12 fs^{-1}$, $\lambda = 1.68\,\mu m$

Figure 6.8: *Normalized ET function between a donor-acceptor pair, when the donor is positioned at* $\mathbf{r}_D = (0,0,10\,nm)$ *for a fixed radius,* $R = 30\,nm$*, and a fixed value of the chemical potential,* $\mu = 1\,eV$*. (a) Acceptor positioned at* $\mathbf{r}_A = (0,0,-10\,nm)$ *for two orientations, along the x and z-axes. For the peak frequencies labeled B-E we present contour plot of the spatial distribution in the xz-plane of the normalized ET function in panels (b-e).*

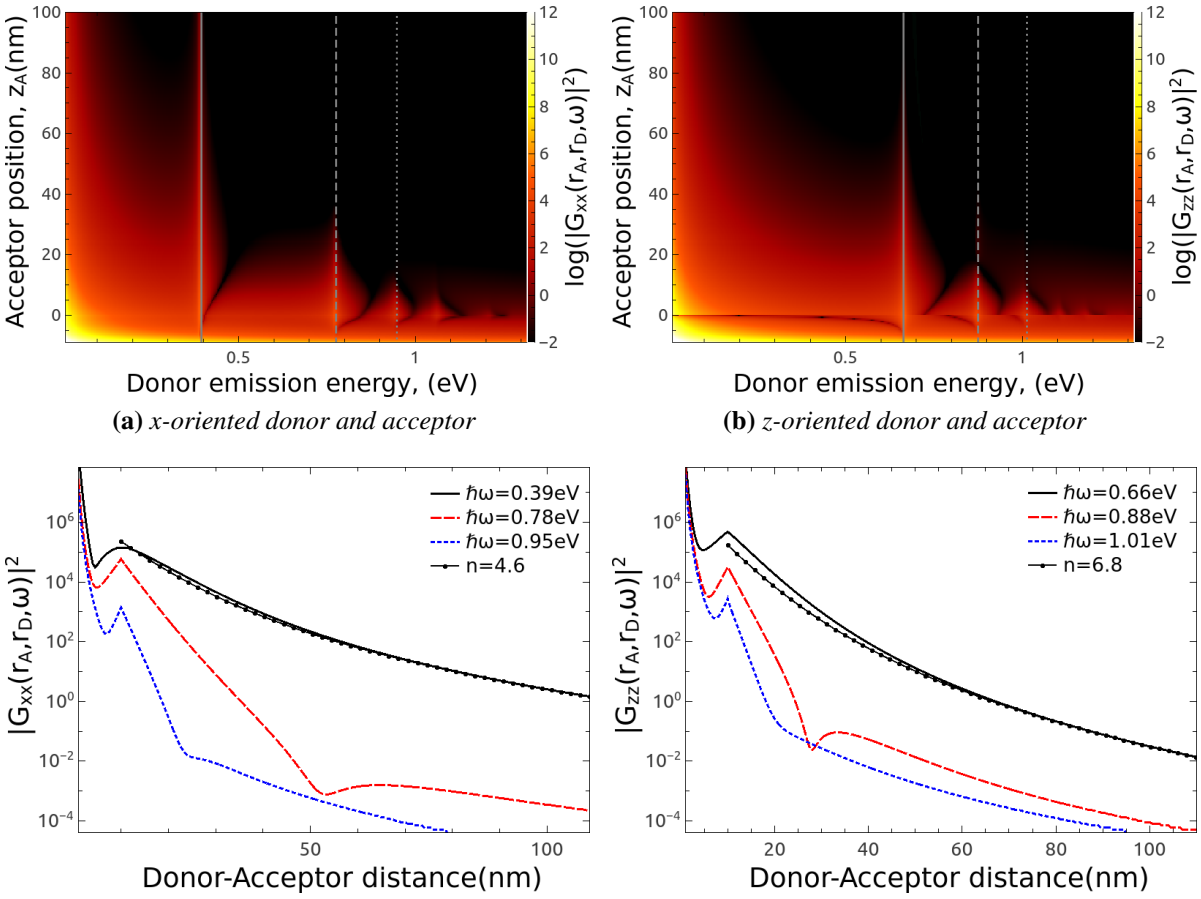

(a) *x-oriented donor and acceptor*

(b) *z-oriented donor and acceptor*

(c) *x-oriented donor and acceptor*

(d) *z-oriented donor and acceptor*

Figure 6.9: *Frequency and acceptor position dependence of the ET function for a donor placed at* $\mathbf{r}_D = (0,0,-10)$ *nm for the case where both donor and acceptor are along the (a) x-axis and (b) z-axis. Donor-acceptor distance dependence of the ET function for frequencies marked by vertical lines in (a) and (b) when both donor and acceptor are along the x-axis, cf. panel (c), and z-axis, cf. panel (d). In all cases the chemical potential is* $\mu = 1$ *eV and the graphene nanodisk radius is* $R = 20$ *nm.*

position, $\mathbf{r}_{\mathrm{D}} = (0,0,-10)$ nm, when the donor and acceptor transition dipole moments are along the x-axis (6.9a) and along the z-axis (6.9b). The acceptor is positioned at $\mathbf{r} = (0,0,z_{\mathrm{A}})$. The chemical potential is $\mu = 1\,\mathrm{eV}$, and the radius is $R = 20\,\mathrm{nm}$. It is observed that for the x-orientation, the normalized ET function has larger values which extend over larger distances compared with the z-orientation. the higher order resonances decay faster than the main resonance, which is the $k = 0$ order for the xx-orientation and the $k = 1$ order for the z-orientation.

The focus now is on the resonance frequencies from panels 6.9a and 6.9b and the dependence of the normalized ET function on the donor-acceptor distance is investigated. The components of the induced Green's tensor are given by Eq. (6.27) and (6.33), where these expressions are separated in resonance and geometrical contributions. The situation is somewhat simplified now, because the donor position is kept fixed. The xx-component of the induced Green's tensor is

$$\mathfrak{G}^{1}_{xx,k}(\mathbf{r},\mathbf{r}') = \text{resonance term} \times \frac{\left[\sqrt{(z/R)^2+1} - z/R\right]^{2k+2}}{\sqrt{(z/R)^2+1}}, \tag{6.50}$$

while the zz-component reads as

$$\mathfrak{G}^{0}_{zz,k}(\mathbf{r},\mathbf{r}') = \text{resonance term} \times \frac{\left[\sqrt{(z/R)^2+1} - z/R\right]^{2k+1}}{\sqrt{(z/R)^2+1}}. \tag{6.51}$$

In panels 6.9c and 6.9d the data obtained from the simulations are fitted with the function

$$f(z) = A(\sqrt{z^2+R^2} - z)^n/(z^2+R^2), \tag{6.52}$$

corresponding to the squares of the expressions in Eqs. (6.50) and (6.51). For the resonances with quantum number $l = 1$ and $k = 0$, the fitting at large donor-acceptor distances gives a value $n = 4.7$, which is close to the value $n = 4$ for $k = 0$ given by Eq. (6.50). The closer the donor is to the graphene nanodisk, however, the worse the fitting with the chosen function is, since this considers that only one resonance contributes to the ET function. In addition, the direct interaction between the donor and acceptor is appreciable when they are close to each other, further leading to a mismatch. For higher order resonances, the behavior becomes more complex, and one can even identify a minimum in the ET function for $k = 1$ at a distance of 50 nm. Similarly, considering the case when both donor and acceptor are along the z-axis, the fitting of the main resonance gives a value of $n = 6.8$, again close to the value $n = 6$ for $k = 1$

given by Eq. (6.51). Furthermore, the minimum in the next higher order resonance occurs even closer to the graphene nanodisk, at a donor-acceptor distance of 25 nm. The appearance of a minimum can be seen in Fig. 6.8e. The ET function falls off more rapidly for the higher frequency resonances, as can be seen in Fig. (6.9c) and (6.9d). This effect is also present in Fig. 6.8e, where the higher frequency of the resonances lead to more lobes in the field distribution, which in turn leads to a tighter confinement of the field at the graphene nanodisk. The distance dependence is further analyzed in the next section.

6.3.3 Energy transfer efficiency

When the donor is excited it generally has two ways of relaxing to the ground state: by transferring its excitation energy to the acceptor with an ET rate k_{ET}, or by relaxing with decay rate k_{SE}. The decay rate k_{SE} takes account of photon emission into the far-field, intrinsic non-radiative recombination paths and coupling to surface plasmon modes. The SE and ET processes are, therefore, in competition with each other and an energy transfer efficiency is introduced to describe this competition. We consider, in what follows, quantum emitters with a quantum yield of one, $Y_0 = 1.0$, which assumes no intrinsic losses such as phonon relaxation, etc.

Using Eqs. (2.29) and (2.34), introduced in Sec. (2.3), for the SE and ET rates of ensembles of emitters and donor-acceptor pairs, an energy transfer efficiency η is defined as [127]

$$\eta = \frac{k_{\mathrm{ET}}}{k_{\mathrm{SE}} + k_{\mathrm{ET}}}. \tag{6.53}$$

This quantity gives the relative contribution of the energy transfer process to the total decay rate of the donor. If the ET efficiency, η, has a value $\eta > 50\%$, then the decay of the excited state of the donor occurs mainly by energy transfer to the acceptor, rather than relaxation into photon or SP modes.

When real quantum emitters are considered, the donor emission spectra, $f_{\mathrm{D}}(\lambda)$, and acceptor absorption spectra, $\sigma_{\mathrm{A}}(\lambda)$, are described by Gaussian distributions and not by the idealized δ-distributions. Note that the properties used to describe the donor and acceptor quantum emitters in this chapter have been introduced earlier, see Sec. (4.3.3). They are restated here for completeness. The donor emission and acceptor absorption spectra are given by

$$A_{\mathrm{q}}\, \mathrm{e}^{-(\lambda-\lambda_{\mathrm{q}})^2/\Delta\lambda_{\mathrm{q}}^2}, \tag{6.54}$$

where $\mathrm{q} = D$ represents the donor and $\mathrm{q} = A$ represents the acceptor, A_{q} is a normalization

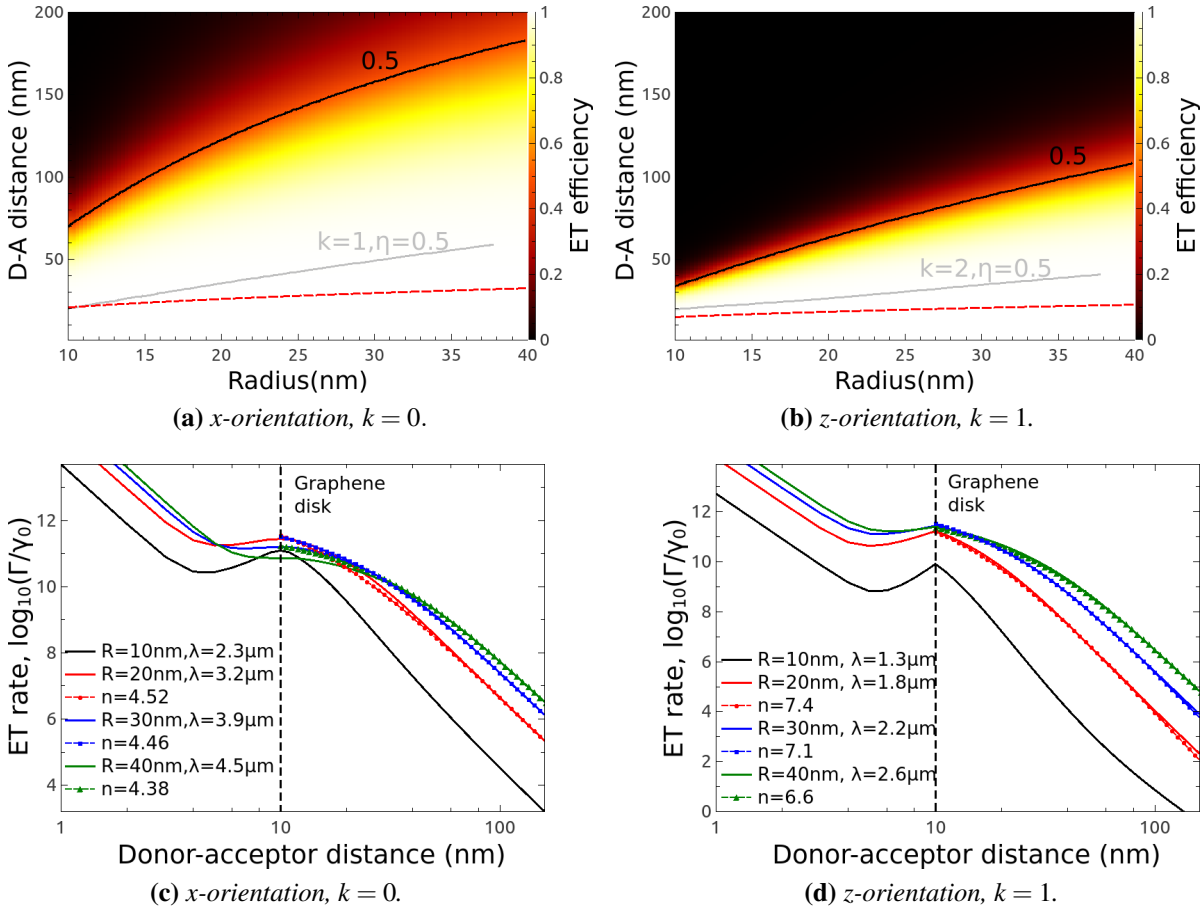

(a) *x-orientation,* $k = 0$.

(b) *z-orientation,* $k = 1$.

(c) *x-orientation,* $k = 0$.

(d) *z-orientation,* $k = 1$.

Figure 6.10: *(a-b) Contour plot of the ET efficiency as a function of graphene nanodisk radius and donor-acceptor distance, for a fixed donor position,* $\mathbf{r}_D = (0,0,10\,nm)$ *and variable acceptor position,* $\mathbf{r}_A = (0,0,z_A)$*, and for different resonances calculated using Eq. (6.38). The solid black line represents the 50% efficiency contour, while the dashed red line represents the same in free-space. The grey line represents the* 50% *efficiency for the* $k = 1$*, panel (a), and* $k = 2$*, panel (b), frequency mode resonances. (c-d) ET rate as a function of donor-acceptor distance for the same fixed position of the donor. The chemical potential is everywhere* $\mu = 1$ *eV.*

constant, λ_q gives the position of the spectral peak and $\Delta\lambda_q$ is related to the full width at half maximum (FWHM) of the spectrum. The normalization constant of the donor emission spectrum is given as $A_D^{-1} = \int_0^\infty d\lambda\, f_D(\lambda)$. The FWHM will be $\Delta\lambda_D = 20$ nm for the donor-acceptor pairs, which corresponds to a typical spectrum of a fluorescent dye, e.g. fluorescein [130]. The constant for the acceptor absorption spectrum is $A_A = 0.021$ nm^2, while the FWHM is $\Delta\lambda_A = 50$ nm. In this section we consider quantum emitters that are on resonance with the graphene nanodisk which means that the position of the spectral peak, λ_q, for the various arrangements, is given by Eq. (6.38), cf. also the dashed lines from Fig. 6.2 and Fig. 6.3.

In Fig. 6.10a and Fig. 6.10b, contour plots of the ET efficiency are presented as a function of the radius of the graphene nanodisk, R, and the donor-acceptor distance, r_{DA}, when the

donor position is kept fixed at $\mathbf{r}_D = (0,0,10\,\text{nm})$ and the position of the acceptor varies. The value of the chemical potential is $\mu = 1\,\text{eV}$. For each panel in the figure, the peak values of the donor emission and acceptor absorption spectra, Eq. (5.20), are taken to be the resonance wavelength, calculated from Eq. (6.38). In Fig. 6.10a, for which the donor and acceptor transition dipole moments are oriented along the x-axis and the resonance wavelength corresponds to $k = 0$, the interaction distance increases with the disk radius. The free-space 50% efficiency contour is given as the dashed red line. It corresponds to the so-called Förster radius. The interaction distance is considerably increased, reaching values well above 100 nm for the larger disk radii considered. In Fig. 6.10b, for which the dipole moment orientation is along the z-axis and the resonance wavelength corresponds to $k = 1$, we observe that the interaction distance is smaller compared with the x-orientation of the transition dipole, while still being larger than the free space value. This is not surprising, since the SE rate and the ET function follow similar trends, and more insight is given by Eqs. (6.24) and (6.31) where the different distance dependences, for the different orientations of the transition dipole moment, are apparent. Furthermore, the next higher order resonances are considered in panels 6.10a and 6.10b where the 50% distance is plotted for $k = 1$ and $k = 2$ resonances, respectively. It is observed that the interaction distance is smaller than for the main resonances. This is a general characteristic for structures supporting localized surface plasmons, such as nanospheres, nanoboxes etc. For these higher order resonances, the interaction distance is also larger than in free-space.

Panels 6.10c and 6.10d show the dependence of the ET rate between a donor-acceptor pair on their separation, for several disk radii from panels 6.10a and 6.10b. The value of the chemical potential is $\mu = 1\,\text{eV}$. For the fitting we use Eq. (6.52), the same expression as for the case of the ET function. For the x-oriented transition dipole moments, the fitting returns $n = 4.4$, for a radius of $R = 40\,\text{nm}$, slightly different from the value $n = 4$ obtained from the induced Green's tensor from Eq. (6.50) for $k = 0$. Interestingly as the radius increases, the fitting value approaches the theoretical value, due to the fact that the contribution from the induced part of the Green's tensor, Eq. (6.47), becomes large. When considering a z-orientation for the transition dipole moments, similar results are obtained, with a fitting parameter $n = 6.6$, for radius of $R = 40\,\text{nm}$, compared with the theoretical value $n = 6$. This discrepancy is attributed to the contribution of higher order modes. The main difference between the behavior of the ET rate for x and z oriented donors and acceptors, is the fact that the absolute values of the ET rate decay faster with distance for the z orientation, explaining the shorter distance over which efficient ET occurs. Furthermore, we want to point out, again, that the distance dependence of the energy transfer for a donor-acceptor pair is fully characterized by the geometrical

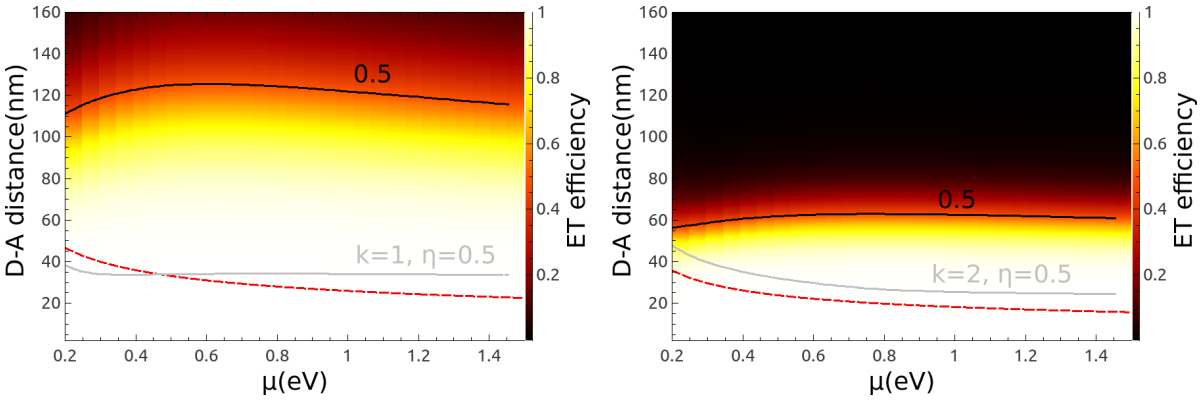

(a) *x-orientation, $k = 0$.* **(b)** *x-orientation, $k = 1$.*

Figure 6.11: *Contour plot of the ET efficiency as a function of the acceptor position, $\mathbf{r}_A = (0,0,z)$, with a fixed position of the donor, $\mathbf{r}_D = (0,0,10nm)$, $d = 10nm - z$. The value of the chemical potential, μ, is varied for fixed value of the radius of the graphene nanodisk, $R = 20nm$, for different resonance frequencies, Eq. (6.38), more details in the inset. The solid black line represents the 50% efficiency contour, while the dashed red line represents the same in free-space. The solid gray line represents the 50% efficiency for the $k = 1$, panel (a), and $k = 2$, panel (b), frequency mode resonances.*

dependence. This is one of the key results of this chapter. This is in contrast with the case considering the interaction of a donor-acceptor pair in the presence of an infinite graphene sheet, for which the perpendicular distance dependence is characterized by the SP penetration depth δ_{SP}, Sec. 6.3.1 [97].

In Fig. 6.11 a contour plot of the ET efficiency is presented as a function of the donor-acceptor distance and chemical potential, for a fixed donor position $\mathbf{r}_{\mathrm{D}} = (0,0,10\,\mathrm{nm})$, and a fixed value of the graphene nanodisk radius, $R = 20\,\mathrm{nm}$. The x and z orientation for the transition dipole moments of the donor-acceptor QEs are considered, Fig. 6.11a and 6.11b respectively. The peak values of the donor emission and acceptor absorption spectra are given by the resonance wavelengths from Eq. (6.38). The ET efficiency is observed to vary slowly with the chemical potential over a broad range of values of the chemical potential. This further supports the argument that the ET efficiency has a strong dependence on the geometrical parameters of the structures and not on the material parameters. The interaction distance is enhanced compared with the free space value for the same set of parameters. In Fig. 6.11a and 6.11b the 50% ET efficiency distance for the $k = 1$ and $k = 2$ resonances is also shown as gray lines, respectively. The ET efficiency for the higher order resonances is not significantly influenced by varying the value of the chemical potential, μ.

6.4 Summary and Conclusions

In this chapter the SE of a single quantum emitter and the ET function have been investigated for a donor-acceptor pair in the presence of a gated graphene nanodisk. While investigating the SE and ET rate sharp resonances are appearing, due to the excitation of localized surface plasmon modes, that can enhance these rates several order of magnitudes compared with their free space values.

Furthermore, due to the competition between the donor SE rate and the ET rate from the donor to the acceptor, an energy transfer efficiency, η, has been introduced. In the case that the donor and acceptor are placed in the middle of the graphene nanodisk, and on opposite sides, the ET efficiency is enhanced compared with its free space value, even for the higher order resonances which are close to the telecommunication wavelengths.

Moreover, the distance dependence of the SE and ET function and the ET rate have been investigated. The distance dependence has a certainly non-trivial behavior which depends on the geometrical characteristics of the disk. The full numerical results describing the interaction distance of a quantum emitter-graphene nanodisk system and of a pair of quantum emitters-graphene nanodisk are fitted with an analytical expression which depends on the geometrical characteristics of the graphene nanodisk, i.e. its radius. In contrast, the perpendicular interaction between a pair of quantum emitters in the presence of an infinite graphene sheet is dictated by the SP penetration depth [97], which is influenced by the value of the chemical potential and the emission energy of the quantum emitters, see Sec. (5.3.3). The interaction distance between a pair of quantum emitters in the presence of a graphene nanodisk is increased, through the interaction with the localized surface plasmon modes of the disc. The interaction distance compared with the free-space is increased by one order of magnitude, for the x-transition dipole orientation of the donor-acceptor quantum emitters for disc radii above 15 nm. Furthermore, when the orientation of the transition dipole moments of the donor-acceptor quantum emitters is along x, the interaction distance is larger compared with z-oriented transition dipole moments.

The knowledge of the distance dependence of the SE rate of a single quantum emitter and of the ET rate between a pair of quantum emitters in the presence of a graphene nanodisk and the tunability of the interaction between them, through the applied voltage, is crucial for a plethora of applications. The gating of an array of graphene nanodisks has been experimentally demonstrated in Ref. [19] and the tunability of the SE rate of the quantum emitters interacting with a gated graphene sheet in Ref. [80]. Thus, the experimental investigation of the interaction of quantum emitters with graphene nanodisks described in this chapter is fea-

sible. Possible applications, such as: tunable plasmonic rulers [78], surface-enhanced Raman scattering [169, 170], quantum information [122], sensing devices [11, 154] and light harvesting [155] could benefit from tuning the interaction distance and efficiency.

Finally, novel two dimensional materials have been considered in recent years due to the high demand for nanostructures with emission in the visible. Materials belonging to the family of diochalgonides [171], like MoS_2, fulfill this requirement and the analysis presented above is general enough to be applied to any two-dimensional material with a known surface conductivity, in the electrostatic limit. Furthermore, this analytical formalism is also valid for metallic plasmonic nanodisks, i.e. Au, Ag or Cu, with small thickness and large radius to thickness ratio [172].

Chapter 7

Conclusions and Outlook

7.1 Conclusions

In this thesis the interaction between quantum emitters in the presence of conducting nanostructures is investigated. In particular, the spontaneous emission rate, of a single quantum emitter, and the energy transfer rate, between a pair of quantum emitters, in the presence of conducting nanostructures have been studied. The influence of the surface plasmon modes provided by the conducting nanostructures has been found to enhance these rates. Furthermore, an energy transfer efficiency has been introduced in order to examine which of these two processes is favored. The interaction distance between a pair of quantum emitters is enhanced when a conducting material is present, compared with its free space values.

In Chapter 3 a single planar interface, between a metal and a dielectric, and a metallic slab, in dielectric host media, have been considered. The spontaneous emission rate of a single quantum emitter is enhanced several order of magnitudes, compared with its free space value, when it is in proximity to the planar nanostructures of thicknesses of tens of nanometers. The distance dependence of the spontaneous emission away from the single interface geometry has been analyzed. Different contributions dominate in different distances. In particular, very close to the interface between metal and dielectric the lossy surface waves dominate, which are connected with Ohmic losses, as the distance is increased above 5 nm the surface plasmon mode dominates and for larger distances the spontaneous emission rate reverts to its free space value. The spectral dependence of the spontaneous emission rate presents large enhancements, compared with the free space values, close to the surface plasmon wavelengths. The surface plasmon dispersion relation has been used to analyze these contributions. The energy transfer, between a pair of quantum emitters, is influenced by the position of the donor. It needs to be close to the metal dielectric interface in order to facilitate high energy transfer. When the

energy transfer is considered for the case of a metallic slab, the donor emission wavelength is crucial for exciting the surface plasmon wavelength. If the emission frequency lies between the two surface plasmon curves of the dispersion relation, for small thicknesses of the metallic slab, the energy transfer rate is suppressed.

The analysis conducted for the interaction between quantum emitters and metallic planar nanostructures provides an introduction for the next chapters. In Chapter 4 the level of complexity is increased, the spontaneous emission and energy transfer rates have been investigated in the presence of a dielectric coated metallic cylinder. Au and Ag cores have been considered. Experimental data have been used for the dielectric permitivitties of the metallic core taken from Ref. [129]. Again the spontaneous emission rate has been enhanced when the emission wavelength of the quantum emitter is close to the surface plasmon wavelength and its position is close to the coated cylinder. Au and Ag have different plasmon resonance wavelengths and different material losses yielding different modification of the spontaneous emission resonances. Also, the energy transfer rate, between a pair of quantum emitters, in the presence of metallic nanostructures is influenced by the surface plasmon modes. The dielectric coating acts as a mediator for the energy transfer process. The existence of hot spots around the circumference of the coated cylinder is also observed, the number of hot spots is connected with the number of the modes excited, which can be found from the dispersion relation.

The energy transfer efficiency, between a pair of quantum emitters in the presence of the dielectric coated metallic cylinder, depends strongly on the overlap integral between the emission spectrum of the donor, the absorption cross section of the acceptor and the spectral dependence of the absolute value of the Green's tensor. Thus, strong overlap of the emission and absorption spectra with the surface plasmon wavelength leads to enhancement of the interaction distance over the free space values. The dielectric coated cylinder acts as a lens when the distance dependence between a pair of quantum emitters across the cylinder is considered. Furthermore, the surface plasmon wavelength can be tuned by changing the value of the dielectric permittivity of the coating and the core material.

The noble metals suffer from high material losses. Graphene, a material that can also support surface plasmon modes, has lower losses. Thus grahene might be a suitable candidate for replacing noble metals. In Chapter 5 the spontaneous emission and energy transfer rates have been considered in the presence of a graphene monolayer. The optical properties of graphene can be tuned via an applied voltage, thus influencing the emission properties of the quantum emitters. The normalized spontaneous emission, of a single quantum emitter, and energy transfer function, between a pair of quantum emitters, are enhanced several orders of magnitude when the emission wavelength matches the plasmon wavelengths, compared with

their free space values. The energy transfer efficiency has values above 50% for distances up to 300 nm, for quantum emitters positioned very close to the graphene monolayer. Moreover, the distance dependence of the energy transfer rate at small donor-acceptor separations is characterized by an R^{-6} dependence. When increasing the separation distance along the graphene monolayer, the propagation length of the graphene surface plasmon mode dominates the energy transfer rate and again enhances the interaction distance over larger distances, compared with their free space value. When the perpendicular distance between the donor and acceptor is varied, the energy transfer rate distance dependence is characterized by the penetration length of graphene plasmon mode.

In Chapters 3,4 and 5 extended conducting nanostructure have been considered. Thus the surface plasmon modes are propagating, tightly confined to the surface of the conductors. In Chapter 6 a gated graphene disk has been considered as the conducting medium, thus confining the light in all three dimensions. The surface plasmon modes are now localized. The normalized spontaneous emission and energy transfer rates have been enhanced compared with their free space values following sharp resonances which they can be tuned by the chemical potential and the nanodisk radius. Different set of resonances are excited when considering different transition dipole moments of the quantum emitters. The distance dependence of the energy transfer efficiency, between a pair of quantum emitters, along the axis perpendicular to the graphene nanodisk, is enhanced compared to free space, once the emission wavelength of the donor matches the resonance wavelength. Considering higher order resonances the interaction distance is smaller but still larger than free space values. The distance dependence of the energy transfer rate, between a pair of quantum emitters, is fully characterized by the geometrical property of the graphene nanostructure, its radius.

The main goal of this thesis was to investigate routes for enhancing the interaction distance between a pair of quantum emitters. The free space interaction is weak. Choosing conducting nanostructures, that support surface plasmon modes, the interaction distance can be enhanced. This statement is the main conclusion of my work. A great deal of work for this thesis it has been devoted to the distance dependence of the spontaneous emission and energy transfer rates due to fact that these quantities can be directly measured and thus exploited from an application point of view. Applications such as a plasmon ruler, sensing devices, light harvesting and quantum computing can potentially benefit from enhanced energy transfer rates, efficiencies and distances. In the next section further ideas are considered for extending the current work.

7.2 Outlook and Future Work

In this section further work on the study of the nanostructures discussed in this thesis will be considered. Starting from the planar structures, Chapter 3, one can further investigate how the emission properties of a periodic array of quantum emitters positioned above a metallic slab compare with a single emitter. For this one can use a Hubbard Hamiltonian to investigate these collective phenomena [173].

For the dielectric coated metallic cylinder, Chapter 4, the energy transfer efficiency has been studied across the axis of the cylinder. Thus, the next direct step would be to investigate the interaction distance between a pair of quantum emitters along the coated cylinder [38, 40]. Also, instead of a metallic core, the case of a metallic coating can be considered. Furthermore, the material of the coating can be replaced with a material supporting surface phonon polaritons and compare it with a graphene nanotube [109] because the resonance wavelengths are for both materials in the infrared. The case where the core medium is a lossy material and the coating is a gain material, or vice versa, can also be considered. In this case due to the breaking of the PT-symmetry the nanostructure will only allow specific orientations for light transmission [174, 175].

A vast family of two dimensional material monolayers are being developed [176–178]. These materials they can be considered as a replacement for the graphene monolayer, Chapter 5. Graphene is a well studied material and its surface conductivity is described by a closed form formula [131]. Moreover, understanding the material properties of the new two-dimensional materials, like MoS2, is challenging [118, 179]. Investigating the interaction distances for these materials using the Green's tensor formalism is also of fundamental importance for possible applications in the future.

Considering the infinitely thin nanodisk geometry, Chapter 6, the next step will be to consider different material replacing the graphene. Using an effective surface conductivity, noble metal materials can be considered as replacements [172]. Then one can use the formalism developed in this thesis to investigate the interaction distance between a pair of quantum emitters.

In this thesis metallic and graphene nanostructures are considered and their interaction with quantum emitters is investigated. Both of these material have a similarity, they are able to confine light to sub-diffraction lengths by supporting surface plasmon modes. A main difference between them is their surface plasmon resonance wavelengths. For the noble metals are in the visible part of the spectrum, while for graphene the resonance frequencies spans from the near to the far infrared part of the spectrum. Thus, graphene is unfavorable for many applications in

the visible part of the spectrum. On the other hand, the material losses for the noble metals are higher than in the case of graphene. Furthermore, graphene's optical response can be tuned via the value of the chemical potential, giving an additional advantage over the noble metals. To date the primary commercial application that has become successful is the surface enhanced Raman scattering (SERS) [169]. Graphene on the other hand has only been exploited as a complementary material, not providing, up to this day, any unique commercial application, in the field of photonics [180]. However with the recent emergence of many new two dimensional materials it might be expected that someones can achieve the desired properies in order for plasmonics to be used for everyday commercial photonics applications [178]. Stronger collaboration is needed between the different branches of science, such as engineering, experimental and theoretical physics and chemistry in order to develop materials with the desirable properties for the future applications.

The field of plasmonics is active and has not yet fully exploited in order to bring to the society its full benefits. There are still a lot to be done, something exciting for all the people working on the field.

Bibliography

[1] R. P. Feynman, Eng. Sci. **23**, 22 (1960).

[2] S. V. Gaponenko, *Introduction to Nanophotonics*, 1st ed. (Cambridge University Press, New York, NY, USA, 2010).

[3] P. Andrew and W. L. Barnes, Science **306**, 1002 (2004).

[4] W. L. Barnes, A. Dereux, and T. W. Ebbesen, Nature **424**, 824 (2003).

[5] A. V. Akimov, A. Mukherjee, C. L. Yu, D. E. Chang, A. S. Zibrov, P. R. Hemmer, H. Park, and M. D. Lukin, Nature **450**, 402 (2007).

[6] J. D. Thompson, T. G. Tiecke, N. P. de Leon, J. Feist, A. V. Akimov, M. Gullans, A. S. Zibrov, V. Vuletić, and M. D. Lukin, Science **340**, 1202 (2013).

[7] M. S. Tame, K. R. McEnery, S. K. Özdemir, J. Lee, S. A. Maier, and M. S. Kim, Nat. Phys. **9**, 329 (2013).

[8] S. A. Maier and H. A. Atwater, J. Appl. Phys. **98**, 011101 (2005).

[9] W. L. Barnes, J. Opt. A **8**, S87 (2006).

[10] B. M. Reinhard, M. Siu, H. Agarwal, A. P. Alivisatos, and J. Liphardt, Nano Lett. **5**, 2246 (2005).

[11] J. N. Anker, W. P. Hall, O. Lyandres, N. C. Shah, J. Zhao, and R. P. Van Duyne, Nat. Mater. **7**, 442 (2008).

[12] A. G. Brolo, Nat. Photon. **6**, 709 (2012).

[13] J. R. Cole and N. J. Halas, Appl. Phys. Lett. **89**, 153120 (2006).

[14] L. Novotny and N. Van Hulst, Nat. Photon. **5**, 83 (2011).

[15] M. L. Juan, M. Righini, and R. Quidant, Nat. Photon. **5**, 349 (2011).

[16] J. Dionne, L. Sweatlock, H. Atwater, and A. Polman, Phys. Rev. B **72**, 075405 (2005).

[17] A. V. Zayats, I. I. Smolyaninov, and A. A. Maradudin, Phys. Rep. **408**, 131 (2005).

[18] L. Higgins, V. Karanikolas, C. Marocico, A. Bell, T. C. Sadler, P. Parbrook, and A. Bradley, Opt. Express **23**, 1377 (2015).

[19] Z. Fang, S. Thongrattanasiri, A. Schlather, Z. Liu, L. Ma, Y. Wang, P. M. Ajayan, P. Nordlander, N. J. Halas, and F. J. García de Abajo, ACS Nano **7**, 2388 (2013).

[20] E. Purcell, Phys. Rev. **69**, 681 (1946).

[21] H. Morawitz, Phys. Rev. **187**, 1792 (1969).

[22] M. R. Philpott, J. Chem. Phys. **62**, 1812 (1975).

[23] J. Wylie and J. Sipe, Phys. Rev. A **30**, 1185 (1984).

[24] R. M. Amos and W. L. Barnes, Phys. Rev. B **55**, 7249 (1997).

[25] R. Matloob, Phys. Rev. A **62**, 1 (2000).

[26] D. Alves, C. Farina, and A. Tort, Phys. Rev. A **61**, 1 (2000).

[27] I. Larkin, M. Stockman, M. Achermann, and V. Klimov, Phys. Rev. B **69**, 2 (2004).

[28] C. Marocico and J. Knoester, Phys. Rev. A **84**, 1 (2011).

[29] L. Novotny and C. Hafner, Phys. Rev. E **50**, 4094 (1994).

[30] W. Zakowicz and M. Janowicz, Phys. Rev. A **62**, 013820 (2000).

[31] V. V. Klimov and M. Ducloy, Phys. Rev. A **62**, 043818 (2000).

[32] U. Schröter and A. Dereux, Phys. Rev. B **64**, 125420 (2001).

[33] V. V. Klimov and M. Ducloy, Phys. Rev. A **69**, 013812 (2004).

[34] P. K. Rekdal, S. Scheel, P. L. Knight, and E. A. Hinds, Phys. Rev. A **70**, 013811 (2004).

[35] D. Fussell, R. McPhedran, and C. Martijn de Sterke, Phys. Rev. A **71**, 013815 (2005).

[36] P. L. Hernández-Martínez and A. O. Govorov, Phys. Rev. B **78**, 1 (2008).

[37] C. Marocico and J. Knoester, Phys. Rev. A **79**, 053816 (2009).

[38] D. Dzsotjan, A. S. Sørensen, and M. Fleischhauer, Phys. Rev. B **82**, 075427 (2010).

[39] V. Bordo, J. Opt. Soc. Am. B **29**, 1799 (2012).

[40] J. Barthes, A. Bouhelier, A. Dereux, and G. C. D. Francs, Sci. Rep. **3**, 2734 (2013).

[41] H. Chew, Phys. Rev. A **38**, 3410 (1988).

[42] H. T. Dung, L. Knöll, and D.-G. Welsch, Phys. Rev. A **62**, 053804 (2000).

[43] R. Carminati, J.-J. Greffet, C. Henkel, and J. Vigoureux, Opt. Commun. **261**, 368 (2006).

[44] P. Anger, P. Bharadwaj, and L. Novotny, Phys. Rev. Lett. **96**, 113002 (2006).

[45] H. Mertens, A. Koenderink, and A. Polman, Phys. Rev. B **76**, 115123 (2007).

[46] R. S. Swathi and K. L. Sebastian, J. Chem. Phys. **126**, (2007).

[47] V. Klimov, M. Ducloy, and V. Letokhov, Eur. Phys. J. D **20**, 133 (2002).

[48] A. Trügler and U. Hohenester, Phys. Rev. B **77**, 115403 (2008).

[49] V. Klimov, M. Ducloy, and V. Letokhov, Chem. Phys. Lett. **358**, 192 (2002).

[50] D. E. Chang, A. S. Sorensen, P. R. Hemmer, and M. D. Lukin, Phys. Rev. Lett. **97**, 053002 (2006).

[51] D. Chang, A. Sorensen, P. Hemmer, and M. Lukin, Phys. Rev. B **76**, 035420 (2007).

[52] T. Förster, Annalen der Physik **437**, 55 (1948).

[53] D. L. Dexter, J. Chem. Phys. **21**, 836 (1953).

[54] D. L. Andrews and G. Juzeliunas, J. Chem. Phys. **96**, 6606 (1992).

[55] G. J. Daniels, R. D. Jenkins, D. S. Bradshaw, and D. L. Andrews, J. Chem. Phys. **119**, 2264 (2003).

[56] T. Kobayashi, Q. Zheng, and T. Sekiguchi, Phys. Lett. A **199**, 21 (1995).

[57] T. Kobayashi, Q. Zheng, and T. Sekiguchi, Phys. Rev. A **52**, 2835 (1995).

[58] M. Cho and R. J. Silbey, Chem. Phys. Lett. **2614**, (1995).

[59] H. T. Dung, L. Knöll, and D.-G. Welsch, Phys. Rev. A **65**, 043813 (2002).

[60] G. Colas des Francs, C. Girard, and O. J. F. Martin, Phys. Rev. A **67**, 053805 (2003).

[61] V. Karanikolas, C. A. Marocico, and A. L. Bradley, Phys. Rev. A **89**, 063817 (2014).

[62] J. I. Gersten and A. Nitzan, Chem. Phys. Lett. **104**, 31 (1984).

[63] S. D. Druger, S. Arnold, and L. M. Folan, J. Chem. Phys. **87**, 2649 (1987).

[64] P. T. Leung and K. Young, J. Chem. Phys. **89**, 2894 (1988).

[65] V. V. Klimov and V. S. Letokhov, Phys. Rev. A **58**, 3235 (1998).

[66] A. O. Govorov, J. Lee, and N. A. Kotov, Phys. Rev. B **76**, 1 (2007).

[67] M. Minkov and V. Savona, Phys. Rev. B **88**, 081303 (2013).

[68] M. Minkov and V. Savona, Phys. Rev. B **87**, 125306 (2013).

[69] D. Martín-Cano, A. González-Tudela, L. Martín-Moreno, F. J. García-Vidal, C. Tejedor, and E. Moreno, Phys. Rev. B **84**, 235306 (2011).

[70] W. Barnes, J. Light. Technol. **17**, 2170 (1999).

[71] S. Maier, *Plasmonics: Fundamentals and Applications* (Springer, New York, NY, USA, 2007).

[72] F. J. García de Abajo, ACS Photon. **1**, 135 (2014).

[73] A. N. Grigorenko, M. Polini, and K. S. Novoselov, Nat. Photon. **6**, 749 (2012).

[74] P. Alonso-González, A. Y. Nikitin, F. Golmar, A. Centeno, A. Pesquera, S. Vélez, J. Chen, G. Navickaite, F. Koppens, A. Zurutuza, F. Casanova, L. E. Hueso, and R. Hillenbrand, Science **344**, 1369 (2014).

[75] T. Low and P. Avouris, ACS Nano **8**, 1086 (2014).

[76] F. Bonaccorso, Z. Sun, T. Hasan, and A. C. Ferrari, Nat. Photon. **4**, 611 (2010).

[77] G. Konstantatos, M. Badioli, L. Gaudreau, J. Osmond, M. Bernechea, F. P. Garcia de Arquer, F. Gatti, and F. H. L. Koppens, Nat. Nanotechnol. **7**, 363 (2012).

[78] L. Gaudreau, K. J. Tielrooij, G. E. D. K. Prawiroatmodjo, J. Osmond, F. J. G. de Abajo, and F. H. L. Koppens, Nano Lett. **13**, 2030 (2013).

[79] G. Mazzamuto, A. Tabani, S. Pazzagli, S. Rizvi, A. Reserbat-Plantey, K. Schädler, G. Navickaite, L. Gaudreau, F. S. Cataliotti, F. Koppens, and C. Toninelli, New J. Phys. **16**, 113007 (2014).

[80] K. J. Tielrooij, L. Orona, A. Ferrier, M. Badioli, G. Navickaite, S. Coop, S. Nanot, B. Kalinic, T. Cesca, L. Gaudreau, Q. Ma, A. Centeno, A. Pesquera, A. Zurutuza, H. de Riedmatten, P. Goldner, F. J. García de Abajo, P. Jarillo-Herrero, and F. H. L. Koppens, Nat. Phys. **11**, 281 (2015).

[81] F. H. L. Koppens, D. E. Chang, and F. J. García de Abajo, Nano Lett. **11**, 3370 (2011).

[82] Y. V. Bludov, A. Ferreira, N. M. R. Peres, and M. I. Vasilevskiy, Int. J. Mod. Phys. B **27**, 1341001 (2013).

[83] F. J. García de Abajo, ACS Nano **7**, 11409 (2013).

[84] G. W. Hanson, J. Appl. Phys. **103**, 064302 (2008).

[85] M. J. Gullans and J. M. Taylor, arXiv:1407.7035 (2014).

[86] T. Christensen, W. Wang, A.-P. Jauho, M. Wubs, and N. A. Mortensen, Phys. Rev. B **90**, 241414 (2014).

[87] A. H. Castro Neto, N. M. R. Peres, K. S. Novoselov, and A. K. Geim, Rev. Mod. Phys. **81**, 109 (2009).

[88] R. R. Nair, P. Blake, A. N. Grigorenko, K. S. Novoselov, T. J. Booth, T. Stauber, N. M. R. Peres, and A. K. Geim, Science **320**, 1308 (2008).

[89] S. Thongrattanasiri, F. H. L. Koppens, and F. J. García de Abajo, Phys. Rev. Lett. **108**, 047401 (2012).

[90] A. Y. Nikitin, F. Guinea, F. J. Garcia-Vidal, and L. Martin-Moreno, Phys. Rev. B **85**, 081405 (2012).

[91] K. W. K. Shung, Phys. Rev. B **34**, 979 (1986).

[92] R. S. Swathi and K. L. Sebastian, J. Chem. Phys. **130**, 086101 (2009).

[93] A. Y. Nikitin, F. Guinea, F. J. Garcia-Vidal, and L. Martin-Moreno, Phys. Rev. B **84**, 195446 (2011).

[94] K. A. Velizhanin and A. Efimov, Phys. Rev. B **84**, 085401 (2011).

[95] S.-A. Biehs and G. S. Agarwal, Appl. Phys. Lett. **103**, 243112 (2013).

[96] E. Forati, G. W. Hanson, and S. Hughes, Phys. Rev. B **90**, 085414 (2014).

[97] V. D. Karanikolas, C. A. Marocico, and A. L. Bradley, Phys. Rev. B **91**, 125422 (2015).

[98] A. Y. Nikitin, F. Guinea, F. J. García-Vidal, and L. Martín-Moreno, Phys. Rev. B **84**, 161407 (2011).

[99] P. A. Huidobro, A. Y. Nikitin, C. González-Ballestero, L. Martín-Moreno, and F. J. García-Vidal, Phys. Rev. B **85**, 155438 (2012).

[100] S. Thongrattanasiri, I. Silveiro, and F. J. García de Abajo, Appl. Phys. Lett. **100**, 201105 (2012).

[101] E. Forati and G. W. Hanson, Appl. Phys. Lett. **103**, 133104 (2013).

[102] J. H. Strait, P. Nene, W.-M. Chan, C. Manolatou, S. Tiwari, F. Rana, J. W. Kevek, and P. L. McEuen, Phys. Rev. B **87**, 241410 (2013).

[103] P. Nene, J. H. Strait, W.-M. Chan, C. Manolatou, S. Tiwari, P. L. McEuen, and F. Rana, Appl. Phys. Lett. **105**, 143108 (2014).

[104] K. A. Velizhanin, Phys. Rev. B **91**, 125429 (2015).

[105] I. Torre, A. Tomadin, R. Krahne, V. Pellegrini, and M. Polini, Phys. Rev. B **91**, 081402 (2015).

[106] I. V. Bondarev and B. Vlahovic, Phys. Rev. B **75**, 033402 (2007).

[107] R. S. Swathi and K. L. Sebastian, J. Chem. Phys. **132**, 104502 (2010).

[108] A. M. Nemilentsau, G. Y. Slepyan, S. A. Maksimenko, A. Lakhtakia, and S. V. Rotkin, Phys. Rev. B **82**, 235411 (2010).

[109] L. Martin-Moreno, F. J. G. de Abajo, and F. J. Garcia-Vidal, Phys. Rev. Lett. **115**, 173601 (2015).

[110] I. Silveiro, A. Manjavacas, S. Thongrattanasiri, and F. J. García de Abajo, New J. Phys. **15**, 033042 (2013).

[111] I. Silveiro and F. Javier García de Abajo, Appl. Phys. Lett. **104**, 131103 (2014).

[112] S. Thongrattanasiri, A. Manjavacas, and F. J. García de Abajo, ACS Nano **6**, 1766 (2012).

[113] I. Soto Lamata, P. Alonso-González, R. Hillenbrand, and A. Y. Nikitin, ACS Photon. **2**, 280 (2015).

[114] W. Wang, S. P. Apell, and J. M. Kinaret, Phys. Rev. B **86**, 125450 (2012).

[115] A. Y. Nikitin, F. J. Garcia-Vidal, and L. Martin-Moreno, IEEE J. Select. Topics Quantum Electron. **19**, 4600611 (2013).

[116] N. Papasimakis, S. Thongrattanasiri, N. I. Zheludev, and F. García de Abajo, Light: Sci. & Appl. **2**, e78 (2013).

[117] J. R. Piper and S. Fan, ACS Photon. **1**, 347 (2014).

[118] T. Stauber, G. Gómez-Santos, and F. J. G. de Abajo, Phys. Rev. Lett. **112**, 077401 (2014).

[119] F. Ramirez, B. Liu, and S. Shen, J. Quant. Spectrosc. Radiat. Transfer **158**, 27 (2015).

[120] A. Kumar, K. H. Fung, M. T. Homer Reid, and N. X. Fang, Opt. express **22**, 6400 (2014).

[121] W. Wang, P. Apell, and J. Kinaret, Phys. Rev. B **84**, 085423 (2011).

[122] A. Manjavacas, P. Nordlander, and F. J. García de Abajo, ACS Nano **6**, 1724 (2012).

[123] J. D. Cox, M. R. Singh, G. Gumbs, M. A. Anton, and F. Carreno, Phys. Rev. B **86**, 125452 (2012).

[124] D. Martin-Cano, L. Martin-Moreno, F. J. Garcia-Vidal, and E. Moreno, Nano Lett. **10**, 3129 (2010).

[125] K. A. Velizhanin and T. V. Shahbazyan, Physical Review B **86**, 245432 (2012).

[126] H. T. Dung, L. Knöll, and D.-G. Welsch, Phys. Rev. A **57**, 3931 (1998).

[127] X. Zhang, C. A. Marocico, M. Lunz, V. A. Gerard, Y. K. Gun'ko, V. Lesnyak, N. Gaponik, A. S. Susha, A. L. Rogach, and A. L. Bradley, ACS Nano **8**, 1273 (2014).

[128] F. J. García de Abajo, Rev. Mod. Phys. **82**, 209 (2010).

[129] P. B. Johnson and R. W. Christy, Phys. Rev. B **6**, 4370 (1972).

[130] L. Novotny and B. Hecht, *Principles of nano-optics*, 2nd ed. (Cambridge University Press, Cambridge, UK, 2012).

[131] B. Wunsch, T. Stauber, F. Sols, and F. Guinea, New J. Phys. **8**, 318 (2006).

[132] M. Jablan, H. Buljan, and M. Soljačić, Phys. Rev. B **80**, 245435 (2009).

[133] E. Kretschmann and H. Raether, Z. Naturforsch. A **23**, 2135 (1968).

[134] A. Otto, Naturforsch. Phys. **216**, 398 (1968).

[135] S. Scheel and S. Buhmann, Acta Phys. Slov. **58**, 675 (2008).

[136] J. D. Jackson, *Classical Electrodynamics* (Wiley, New York, NY, USA, 1998).

[137] D. P. Craig and T. Thirunamachandran, *Molecular Quantum Electrodynamics: An Introduction to Radiation Molecule Interactions* (Academic Press, New York, NY, USA, 1998).

[138] G. Baffou, R. Quidant, and C. Girard, Phys. Rev. B **82**, 165424 (2010).

[139] G. Baffou, R. Quidant, and F. J. Garcia de Abajo, ACS Nano **4**, 709 (2010).

[140] X. Zhang, C. A. Marocico, M. Lunz, V. A. Gerard, Y. K. Gun'ko, V. Lesnyak, N. Gaponik, A. S. Susha, A. L. Rogach, and A. L. Bradley, ACS Nano **6**, 9283 (2012).

[141] W. C. Chew, *Waves and Fields in Inhomogeneous Media* (IEEE Press, New York, NY, USA, 1995).

[142] C. T. Tai, *Dyadic Green Functions in Electromagnetic Theory* (IEEE Press, New York, NY, USA, 1994).

[143] G. Ford and W. Weber, Phys. Rep. **113**, 195 (1984).

[144] E. N. Economou, Phys. Rev. **182**, 539 (1969).

[145] J. E. Sipe, J. Opt. Soc. Am. B **4**, 481 (1987).

[146] M. Law, L. E. Greene, J. C. Johnson, R. Saykally, and P. Yang, Nat. Mat. **4**, 455 (2005).

[147] O. L. Muskens, J. G. Rivas, R. E. Algra, E. P. A. M. Bakkers, and A. Lagendijk, Nano Lett. **8**, 2638 (2008).

[148] C. B. Winkelmann, I. Ionica, X. Chevalier, G. Royal, C. Bucher, and V. Bouchiat, Nano Lett. **7**, 1454 (2007).

[149] B. Zhang, H. Wang, L. Lu, K. Ai, G. Zhang, and X. Cheng, Adv. Funct. Mater. **18**, 2348 (2008).

[150] F. De Angelis, M. Malerba, M. Patrini, E. Miele, G. Das, A. Toma, R. P. Zaccaria, and E. Di Fabrizio, Nano Lett. **13**, 3553 (2013).

[151] Y. Estrin, D. H. Rich, A. V. Kretinin, and H. Shtrikman, Nano Lett. **13**, 1602 (2013).

[152] L.-W. Li, M.-S. Leong, T.-S. Yeo, and P.-S. Kooi, J. Electromagnet. Wave **14**, 961 (2000).

[153] F. Schwierz, Nat. Nanotechnol. **5**, 487 (2010).

[154] Q. He, S. Wu, Z. Yin, and H. Zhang, Chem. Sci. **3**, 1764 (2012).

[155] C.-C. Lin, D.-Y. Wang, K.-H. Tu, Y.-T. Jiang, M.-H. Hsieh, C.-C. Chen, and C.-W. Chen, Appl. Phys. Lett. **98**, 263509 (2011).

[156] Y. Wang, Z. Li, J. Wang, J. Li, and Y. Lin, Trends Biotechnol. **29**, 205 (2011).

[157] L. A. Falkovsky, J. Phys.: Conf. Ser. **129**, 012004 (2008).

[158] K. S. Novoselov, Science **306**, 666 (2004).

[159] K. S. Novoselov, A. K. Geim, S. V. Morozov, D. Jiang, M. I. Katsnelson, I. V. Grigorieva, S. V. Dubonos, and A. A. Firsov, Nature **438**, 197 (2005).

[160] P. Törmä and W. L. Barnes, Rep. Progr. Phys. **78**, 013901 (2015).

[161] T. Hümmer, F. García-Vidal, L. Martín-Moreno, and D. Zueco, Phys. Rev. B **87**, 115419 (2013).

[162] L. Andreani, G. Panzarini, and J.-M. Gérard, Phys. Rev. B **60**, 13276 (1999).

[163] J. M. Pietryga, R. D. Schaller, D. Werder, M. H. Stewart, V. I. Klimov, and J. A. Hollingsworth, J. Am. Chem. Soc. **126**, 11752 (2004).

[164] J. A. Treadway, G. F. Strouse, R. R. Ruminski, and T. J. Meyer, Inor. Chem. **40**, 4508 (2001).

[165] A. L. Fetter, Phys. Rev. B **33**, 5221 (1986).

[166] F. J. García de Abajo and A. Howie, Phys. Rev. B **65**, 115418 (2002).

[167] U. Hohenester and A. Trügler, Comput. Phys. Commun. **183**, 370 (2012).

[168] A. Vakil and N. Engheta, Science **332**, 1291 (2011).

[169] K. Kneipp, Y. Wang, H. Kneipp, L. T. Perelman, I. Itzkan, R. R. Dasari, and M. S. Feld, Phys. Rev. Lett. **78**, 1667 (1997).

[170] A. Marini, I. Silveiro, and F. J. García de Abajo, ACS Photon. **2**, 876 (2015).

[171] M. M. Ugeda, A. J. Bradley, S.-F. Shi, F. H. da Jornada, Y. Zhang, D. Y. Qiu, W. Ruan, S.-K. Mo, Z. Hussain, Z.-X. Shen, F. Wang, S. G. Louie, and M. F. Crommie, Nat. Mat. **13**, 1091 (2014).

[172] F. J. García de Abajo and A. Manjavacas, Faraday Discuss. **178**, 87 (2015).

[173] A. González-Tudela, C.-L. Hung, D. E. Chang, J. I. Cirac, and H. J. Kimble, Nat. Photon. **9**, 320 (2015).

[174] H. Alaeian and J. A. Dionne, Phys. Rev. B **91**, 245108 (2015).

[175] F. Abbasi, A. R. Davoyan, and N. Engheta, New J. Phys. **17**, 063014 (2015).

[176] J. N. Coleman, M. Lotya, A. O'Neill, S. D. Bergin, P. J. King, U. Khan, K. Young, A. Gaucher, S. De, R. J. Smith, I. V. Shvets, S. K. Arora, G. Stanton, H.-Y. Kim, K. Lee, G. T. Kim, G. S. Duesberg, T. Hallam, J. J. Boland, J. J. Wang, J. F. Donegan, J. C. Grunlan, G. Moriarty, A. Shmeliov, R. J. Nicholls, J. M. Perkins, E. M. Grieveson, K. Theuwissen, D. W. McComb, P. D. Nellist, and V. Nicolosi, Science **331**, 568 (2011).

[177] L. Britnell, R. M. Ribeiro, A. Eckmann, R. Jalil, B. D. Belle, A. Mishchenko, Y.-J. Kim, R. V. Gorbachev, T. Georgiou, S. V. Morozov, A. N. Grigorenko, A. K. Geim, C. Casiraghi, A. H. C. Neto, and K. S. Novoselov, Science **340**, 1311 (2013).

[178] F. Xia, H. Wang, D. Xiao, M. Dubey, and A. Ramasubramaniam, Nat. Photon. **8**, 899 (2014).

[179] A. Scholz, T. Stauber, and J. Schliemann, Phys. Rev. B **88**, 035135 (2013).

[180] K. Kim, J.-Y. Choi, T. Kim, S.-H. Cho, and H.-J. Chung, Nature **479**, 338 (2011).